



# **Measuring the Muon Neutrino Magnetic Moment in the NOvA Near Detector**

Róbert Králik

*Supervisor:* Dr. Lily Asquith

*A thesis submitted in fulfilment of the requirements for the degree of  
Doctor of Philosophy to the*

School of Mathematical and Physical Sciences  
University of Sussex

In Brighton, United Kingdom

April 3, 2024

I hereby declare that I carried out this thesis independently, and only with the cited sources, literature and other professional sources.

I also declare that this thesis has not been and will not be, submitted in whole or in part to another University for the award of any other degree.

*Brighton, United Kingdom,*  
*April 3, 2024*

---

Róbert Králik

# Acknowledgements

School of Mathematical and Physical Sciences, University of Sussex

DOCTORAL THESIS

---

Measuring the Muon Neutrino Magnetic Moment in the NOvA Near  
Detector

---

by Róbert Králik

**ABSTRACT**

Measuring an enhanced neutrino magnetic moment would be a clear indication of physics beyond the Standard Model (BSM), shedding light on the correct BSM theory or the potential Majorana nature of neutrinos. It would manifest in the NOvA near detector as an excess of neutrino-on-electron elastic scattering interactions at low electron recoil energies. Leveraging an intense and highly pure muon neutrino beam, along with the finely segmented liquid scintillator detector technology specifically designed for electromagnetic shower separation, enables NOvA to achieve a potentially world-leading sensitivity in probing the effective muon neutrino magnetic moment. Despite facing statistical limitations stemming from the low cross section of the signal process, systematic uncertainties have a significant impact on this result. To address these challenges, the NOvA Test Beam experiment focuses on mitigating some of the largest systematic uncertainties within NOvA by investigating particle interactions and energy deposition in a small-scale replica NOvA detector. This thesis describes the calibration of the NOvA Test Beam detector, which is a crucial step in analysing the Test Beam data before they can be utilised to reduce NOvA systematic uncertainties.

Keywords: neutrino NOvA electromagnetic testbeam calibration

# Contents

<b>Acknowledgements</b>	<b>ii</b>
<b>List of Figures</b>	<b>vi</b>
<b>List of Tables</b>	<b>x</b>
<b>1 The NOvA experiment</b>	<b>1</b>
1.1 The Neutrino Beam . . . . .	1
1.2 The NOvA Detectors . . . . .	4
1.3 Readout and Data Acquisition . . . . .	6
1.4 Simulation . . . . .	8
1.5 Data Processing and Event Reconstruction . . . . .	11
1.6 Detector Calibration . . . . .	14
1.6.1 Scale . . . . .	17
1.6.2 Threshold and Shielding Correction . . . . .	18
1.6.3 Relative Calibration . . . . .	18
1.6.4 Absolute Calibration . . . . .	20
1.7 Energy Estimation . . . . .	21
1.8 Systematic Uncertainties at NOvA . . . . .	22
<b>2 NOvA Test Beam Detector Calibration</b>	<b>24</b>
2.1 The NOvA Test Beam Experiment . . . . .	25
2.2 Data-based Simulation of Cosmic Muons . . . . .	30
2.2.1 Reconstruction and Selection of Cosmic Data Events . . . . .	31
2.2.2 Energy Correction, Charge Assignment and Smearing . . . . .	36
2.2.3 Validation . . . . .	41
2.3 NOvA Test Beam Detector Calibration . . . . .	44
2.3.1 Fibre Brightness . . . . .	47
2.3.2 Threshold and Shielding Corrections . . . . .	48
2.3.3 Simulation . . . . .	48
2.3.4 Period 2 Data . . . . .	53

2.3.5	Period 3 Data . . . . .	60
2.3.6	Period 4 Data . . . . .	68
2.3.7	Absolute Calibration Results . . . . .	73
2.3.8	Results . . . . .	74
2.3.9	Validation . . . . .	75
2.4	Conclusion . . . . .	76
<b>Acronyms</b>		<b>94</b>
<b>Bibliography</b>		<b>97</b>

# List of Figures

1.1	The schematic of the NuMI beam facility . . . . .	2
1.2	NuMI neutrino beam components in the NOvA near detector . . . . .	3
1.3	The NOvA off-axis beam concept . . . . .	3
1.4	NOvA detectors . . . . .	4
1.5	NOvA Avalanche Photo Diodes . . . . .	6
1.6	NOvA Front End Board . . . . .	7
1.7	NOvA reconstruction of a single electron . . . . .	12
1.8	NOvA detectors event topologies . . . . .	14
1.9	Tricell condition for calibration hits in NOvA . . . . .	16
1.10	Fibre Brightness bins for the NOvA calibration . . . . .	17
1.11	Example attenuation fit for NOvA Relative calibration . . . . .	19
1.12	Example LOWESS correction for NOvA Relative calibration . . . . .	20
1.13	Example distributions for the NOvA absolute calibration . . . . .	21
2.1	Comparison of Test Beam detector to the Near and Far Detectors . .	26
2.2	Scintillator oils used in the Test Beam detector . . . . .	28
2.3	Removing Test Beam beam spill . . . . .	32
2.4	Track start and $\text{Cos}_Z$ cut for data-based simulation selection . . . .	33
2.5	Tracking algorithms for the data-based simulation selection . . . .	35
2.6	Tracking algorithms $\text{Cos}_Z$ distributions for the data-based simulation selection . . . . .	36
2.7	Event selection for the data-based simulation . . . . .	38
2.8	Energy correction for through-going muons for the data-based simulation . . . . .	39
2.9	Data-Simulation comparison of angular distributions . . . . .	42
2.10	Data-Simulation comparison of angular and track length distributions	43
2.11	Data-Simulation comparison of track start distributions . . . . .	44
2.12	Data-Simulation comparison of track start distribution . . . . .	45
2.13	Comparison of simulation to a circular re-simulation validation sample	46

2.14 Example of failed attenuation fits used for the Test Beam fibre brightness file . . . . .	47
2.15 Examples of threshold and shielding corrections for the Test Beam detector . . . . .	49
2.16 Plane-Cell distribution of hits for the simulation sample . . . . .	50
2.17 Uncorrected energy response along the position within a cell for simulation . . . . .	50
2.18 Uncorrected average energy response along cells for simulation. . . . .	51
2.19 Uncorrected average energy response along planes for simulation. . . . .	52
2.20 Map of fitted response at cell centre for simulation . . . . .	52
2.21 Example attenuation fits for simulation . . . . .	53
2.22 Plane-Cell distribution of hits for the period 2 data sample . . . . .	54
2.23 Uncorrected energy response along the position within a cell for period 2 data . . . . .	55
2.24 Uncorrected energy response along cells for epochs in period 2 data. . . . .	55
2.25 Uncorrected average energy response along planes for epochs in period 2 data. . . . .	56
2.26 Map of fitted response at cell centre for period 2 data . . . . .	56
2.27 Attenuation fits for standard cells in period 2 data . . . . .	57
2.28 Attenuation fits for underfilled cells in period 2 data . . . . .	57
2.29 Attenuation fits for underfilled cells in plane 1 in period 2 data . . . . .	58
2.30 Attenuation fits for cells in planes 55 and 57 in period 2 data . . . . .	58
2.31 Attenuation fits for cells with swapped cables in period 2 data . . . . .	59
2.32 Attenuation fits for cells with large fluctuations in period 2 data . . . . .	59
2.33 Plane-Cell distribution of hits for the period 3 data sample . . . . .	61
2.34 Uncorrected average energy response along the position within a cell for epochs in period 3 data. . . . .	61
2.35 Uncorrected average energy response along cells for epochs in period 3 data. . . . .	62
2.36 Uncorrected average energy response along planes for epochs in period 3 data. . . . .	62
2.37 Map of fitted response at cell centre for epochs 3a, 3b and 3c data . . . . .	63

2.38	Attenuation fits for re-filled cells in period 3 data . . . . .	64
2.39	Attenuation fits for cells with faulty readout in period 3 data . . . . .	65
2.40	Attenuation fits for cells with large fluctuations in period 3 data . . . . .	65
2.41	Map of fitted response at cell centre for epochs 3d and 3e data . . . . .	66
2.42	Attenuation fits for dead channels cells in period 3 data . . . . .	66
2.43	Attenuation fits for cells with mixed scintillators in period 3 data . . . . .	67
2.44	Corrected map of fitted response at cell centre for epochs 3d and 3e data . . . . .	67
2.45	Attenuation fits for cells with large fluctuations in period 3 data . . . . .	68
2.46	Plane-Cell distribution of hits for the period 4 data sample . . . . .	69
2.47	Uncorrected average energy response along the position within a cell (w) for epochs in period 4 data. . . . .	70
2.48	Uncorrected average energy response along cells for epochs in period 4 data. . . . .	70
2.49	Uncorrected average energy response along planes for epochs in pe- riod 4 data. . . . .	70
2.50	Map of fitted response at cell centre for period 4 data . . . . .	71
2.51	Attenuation fits for cells with in period 4 data . . . . .	71
2.52	Corrected map of fitted response at cell centre for period 4 data . . . . .	72
2.53	Example distributions of reconstructed (left) and true (right) energy response of stopping muons 1-2 m from the end of their tracks. The mean of the reconstructed (true) response is the reconstructed (true) MEU unit. . . . .	73
2.54	Distributions of stopping muons within a 1-2 m track window from the end of their tracks across the position within a cell. . . . .	77
2.55	Distributions of stopping muons within a 1-2 m track window from the end of their tracks across the position within a cell. . . . .	78
2.56	Distributions of stopping muons within a 1-2 m track window from the end of their tracks across the cells of the detector. . . . .	79
2.57	Distributions of stopping muons within a 1-2 m track window from the end of their tracks across the cells of the detector. . . . .	80
2.58	Distributions of stopping muons within a 1-2 m track window from the end of their tracks across the planes of the detector. . . . .	81

2.59 Distributions of stopping muons within a 1-2 m track window from the end of their tracks across the planes of the detector. . . . .	82
2.60 Distributions of stopping muons within a 1-2 m track window from the end of their tracks across the cosine of the track angle from the X (horizontal) axis. . . . .	83
2.61 Distributions of stopping muons within a 1-2 m track window from the end of their tracks across the cosine of the track angle from the X (horizontal) axis. . . . .	84
2.62 Distributions of stopping muons within a 1-2 m track window from the end of their tracks across the cosine of the track angle from the Y (vertical) axis. . . . .	85
2.63 Distributions of stopping muons within a 1-2 m track window from the end of their tracks across the cosine of the track angle from the Y (vertical) axis. . . . .	86
2.64 Distributions of stopping muons within a 1-2 m track window from the end of their tracks across the cosine of the track angle from the Z (beam) axis. . . . .	87
2.65 Distributions of stopping muons within a 1-2 m track window from the end of their tracks across the cosine of the track angle from the Z (beam) axis. . . . .	88
2.66 Distributions of stopping muons within a 1-2 m track window from the end of their tracks across the event UNIX time. . . . .	89
2.67 Distributions of stopping muons within a 1-2 m track window from the end of their tracks across the event UNIX time. . . . .	90
2.68 Distributions of stopping muons within a 1-2 m track window from the end of their tracks. . . . .	91
2.69 Distributions of stopping muons within a 1-2 m track window from the end of their tracks. . . . .	92

# List of Tables

1.1	Models and tunes used in the NOvA simulation of neutrino interactions.	10
2.1	Test Beam detector data taking periods. . . . .	25
2.2	Overview of the event selection for the data-based simulation . . . .	37
2.3	Description of Test Beam period 3 epochs . . . . .	60
2.4	Table of the absolute calibration results. MEU <sub>Reco</sub> values (top table) are in units of PECorr/cm and MEU <sub>True</sub> values (bottom table) are in units of MeV/cm . . . . .	73

# CHAPTER 1

## The NOvA experiment

tion experiment based at the Fermi National Accelerator Laboratory (FERMILAB) [2]. NOvA receives an off-axis  $\nu_\mu$  and  $\bar{\nu}_\mu$  beam from FERMILAB’s Neutrinos from the Main Injector (NuMI) neutrino source, described in Sec. 1.1, and measures  $\nu_e/\bar{\nu}_e$  appearance and  $\nu_\mu/\bar{\nu}_\mu$  disappearance between its two highly active and finely segmented detectors, described in Sec. 1.4 [3].

The capability to measure both  $\nu_e$  and  $\bar{\nu}_e$  appearance, coupled with a significant matter effect induced by the long baseline, allows NOvA to address some of the most important questions in neutrino physics to date, such as the neutrino mass ordering, the octant of  $\theta_{23}$ , and the possible Charge conjugation - Parity (CP) violation in the neutrino sector [3–7]. NOvA data also enables measurements of the values of  $\theta_{13}$ ,  $\theta_{23}$  and  $|\Delta m_{atm}^2|$  [3], measurements of neutrino differential cross sections in the near detector [8–11], constraints on the possible sterile neutrino models [12, 13], monitoring for supernova neutrino activity [14, 15], searches for magnetic monopoles [16], and constraints on the neutrino electromagnetic properties (this thesis). Using two functionally identical detectors mitigates the systematic uncertainties of neutrino oscillation measurements, described in Sec. 1.8.

NOvA started taking data in February 2014 and is expected to run through 2026 [17]. *TO DO: Add DUNE into this and find the LOI reference*

### 1.1 The Neutrino Beam

The neutrino beam for NOvA comes from the FERMILAB-based NuMI neutrino source [18]. The schematic description of NuMI is shown in Fig. 1.1, starting on the left hand side with 120 GeV protons from the Main Injector (MI), part of the FERMILAB accelerator complex. The proton beam is divided into 10  $\mu$ s long pulses, with  $\sim 5 \times 10^{13}$  Protons On Target (POT) per spill every  $\sim 1.3$  s long cycle time, resulting in

a proton beam power of  $\sim 800$  kW, with upgrades currently underway to surpass 1 MW [19].

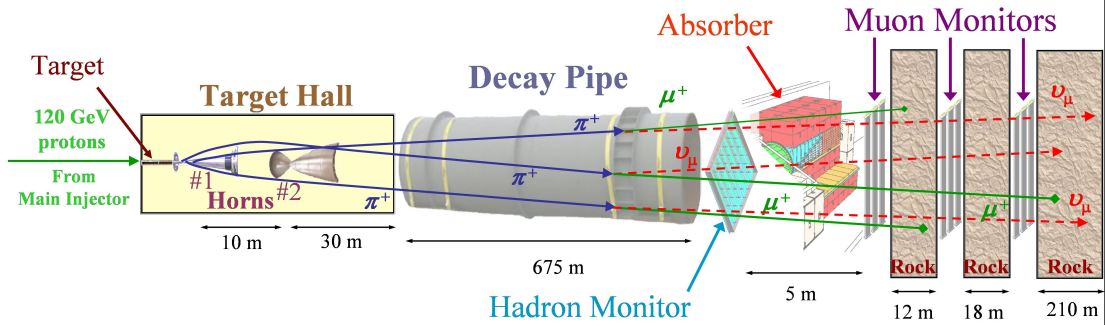


Figure 1.1: The NuMI neutrino beam starts on the left hand side with protons from the MI impinged on a graphite target producing mainly pions and kaons. These are then focused and charge-selected by two focusing horns, after which they decay inside the decay pipe into a high-purity  $\nu_\mu$ , or  $\bar{\nu}_\mu$  beam. The residual hadrons are stopped and monitored in the hadron absorber and the remaining muons are recorded with muon monitors and absorbed inside the rock. Figure from [18].

The proton beam passes through a collimating baffle before hitting a  $\sim 1.2$  m-long (equal to about two interaction lengths) graphite target [20], producing hadrons, predominantly pions and kaons [18]. These are then focused and selected by two parabolic magnetic "horns". The focused hadrons pass through a 675 m-long decay pipe filled with helium to create a low density environment for hadrons to propagate and decay in flight into either neutrinos or antineutrinos. High energy hadrons that do not decay in the decay pipe are absorbed within a massive aluminium, steel, and concrete hadron absorber and monitored with a hadron monitor. The leftover muons are ranged out in dolomite rock after the absorber and monitored using three muon monitors. The hadron and all the muon monitors are ionization chambers, used to monitor the quality, location and relative intensity of the beam.

Using a positive current inside the horns focuses positively charged particles, which then decay into neutrinos, and removes negatively charged particles. Reversing the horn current focuses negatively charged particles, which decay into antineutrinos, and defocuses positively charged particles. The neutrino mode is therefore called Forward Horn Current (FHC) and the antineutrino mode is called Reverse Horn Current (RHC). The composition of the neutrino beam for both these modes at the NOvA Near Detector (ND), shown as a rate of Charged current (CC) events, is presented in Fig. 1.2, displaying the very high purity  $\nu_\mu$  component in the FHC beam,

and the high purity  $\bar{\nu}_\mu$  component in the **RHC** mode [18].

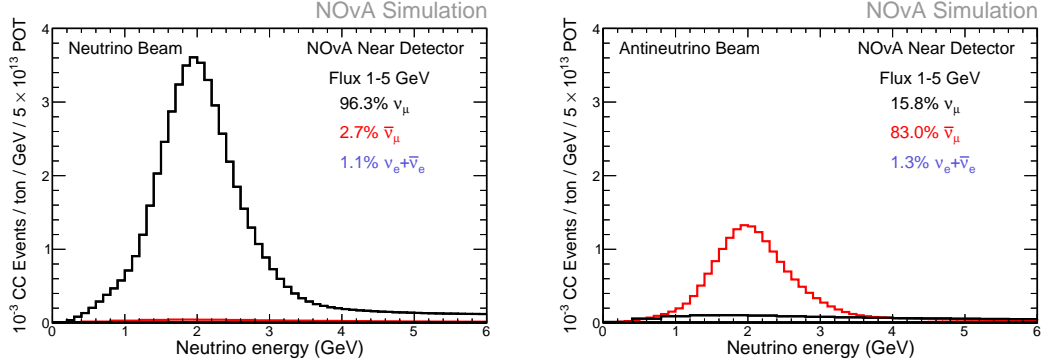


Figure 1.2: The **CC** event rates for different neutrino flavours, as measured at the **NOvA ND** in the **FHC** regime shown on the left, or the **RHC** regime on the right. The contribution of neutrino flavours to the event rates is also displayed, showing the high purity of the neutrino beam for **NOvA**. Figure from internal **NOvA** repository.

The resulting neutrino beam energy distribution is peaked at  $\sim 7$  GeV with a wide energy band. However, thanks to the kinematics of the dominant pion decay, by placing **NOvA** detector 14.6 mrad ( $\approx 0.8^\circ$ ) off the main **NuMI** beam axis, we achieve a narrow band neutrino flux peaked at 1.8 GeV [7, 21], as can be seen in Fig. 1.3. Using an off-axis neutrino flux increases the neutrino beam around 2 GeV about 5-fold compared to the on-axis flux and narrow-band peak enhances background rejection for the  $\nu_e$  appearance analysis [21].

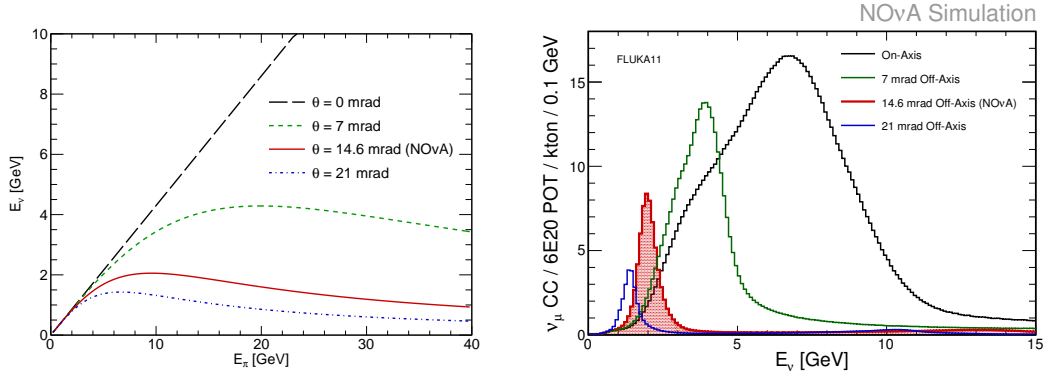


Figure 1.3: (Left) Dependence of the neutrino energy on the parent pion's energy and (right) neutrino energy distribution for an on-axis beam and three different off-axis beam designs. The case for **NOvA** is shown here in red and results in a narrow neutrino energy distribution around 2 GeV, with limited dependence on the parent pion's energy. Figure from [21]

## 1.2 The NOvA Detectors

The two main NOvA detectors are the ND, located in FERMILAB  $\sim 1$  km from the NuMI target and  $\sim 100$  m under ground, and the Far Detector (FD), located  $\sim 810$  km from FERMILAB at Ash River in north Minnesota, partially underground with a rock overburden [21]. NOvA also operated a detector prototype called Near Detector on the Surface (NDOS) used for early research and development of detector components and analysis [4]. Additionally, NOvA operated a Test Beam (TB) detector, described in detail in Sec. ???. The scale of ND and FD is shown in Fig. 1.4.

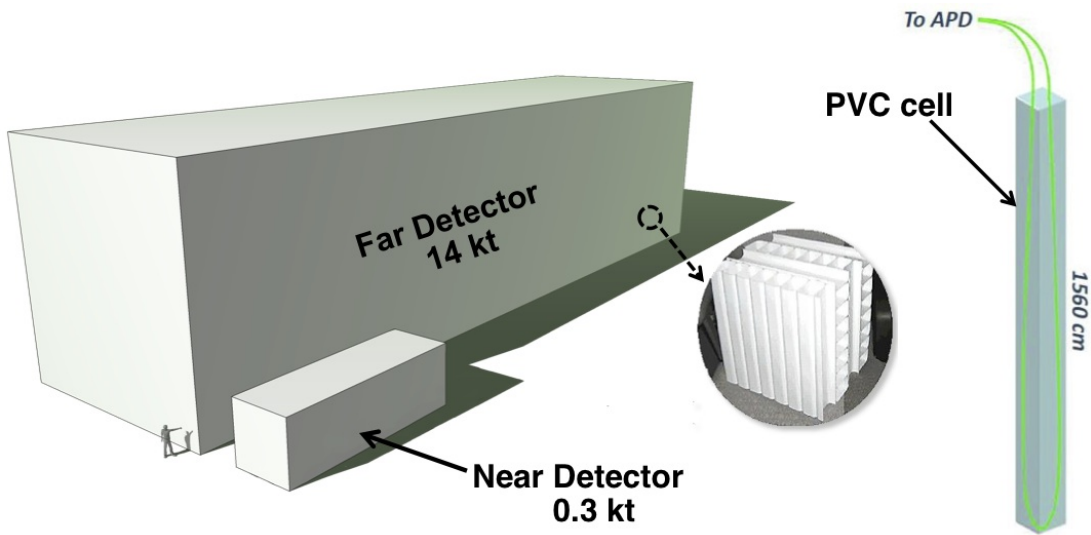


Figure 1.4: Schematic description of scale and composition of the NOvA detectors. The inset shows a photo of the orthogonal planes made out of PVC cells. An example of a FD cell containing liquid scintillator and a looped WLS fibre attached to an APD is shown on the right [22].

All NOvA detectors are highly segmented, highly active, functionally identical tracking calorimeters made up of Polyvinyl chloride (PVC) cells filled with liquid scintillator. Each cell is a long rectangular cuboid with depth of 5.9 cm and width of 3.8 cm (with some variations), with cell length extending to the full width/height of each detector, which is  $\sim 4.1$  m for the ND and  $\sim 15.6$  m for the FD [21]. An example of a FD cell is shown on the right of Fig. 1.4.

Cells are connected side-by-side into a 16 cell-wide extrusions with 3.3 mm-wide walls between cells and 4.9 mm-wide walls on the outsides of the extrusions. The first and last cell of each extrusion are  $\sim 3$  mm narrower than the rest of the cells. Two extrusions are connected side-by-side to form a 32 cell-wide module, with each module

having a separate readout (see Sec. 1.3). In the **FD**, 12 modules are connected side-by-side to form one plane of the detector. In the **ND** only 3 modules make up a plane. Planes are positioned one after another, alternating between vertical and horizontal orientation, and grouped into diblocks, each containing 64 planes. The **FD** contains 14 diblocks, totalling 896 planes, whereas the **ND** contains 3 diblocks totalling 192 planes. However, the **ND** also consists of a Muon Catcher region, positioned right after the active region, consisting of 22 planes of the normal **NOvA** detector design, 2 modules high and 3 modules wide, sandwiched with 10 steel plates to help range out muons mainly from the  $\nu_\mu$  charged current interactions [4, 21].

**TO DO:** *Describe the coordinate system in NOvA*

Each cell is filled with a liquid scintillator consisting of mineral oil with 4.1% pseudocumene as the scintillant [23]. Each cell contains a single wavelength shifting fibre with double the length of the cell, looping at one end and connecting to the readout at the other. As light travels through the fibre, it is attenuated by about a fraction of ten for the **FD** cells **TO DO:** *Figure out what is the correct statement here.* The **PVC** walls of the detector cells are loaded with highly reflective titanium dioxide, with light typically bouncing off the **PVC** walls about 8 times before being captured by the fibre [21].

The final dimensions of the **FD** are  $15.6\text{ m} \times 15.6\text{ m} \times 60\text{ m}$  with a total mass of 14 kT and for the **ND** the dimensions are  $3.8\text{ m} \times 3.8\text{ m} \times 12.8\text{ m}$  with a mass of about 0.3 kT [17]. The active volume, consisting only of the liquid scintillator without the **PVC** structure, makes up about 70% of the total detector volume [21].

The **NOvA** detectors are specifically designed for electromagnetic shower identification, with a radiation length of 38 cm, which amounts to  $\sim 7$  planes for particles travelling perpendicular to the detector planes [4]. This is particularly useful to distinguish electrons and  $\pi^0$ s.

**TO DO:** *Talk here or in the next section about minimum electron energy to be recorded by NOvA detector and electronics. Maybe in all sections including reconstruction to tie them together*

### 1.3 Readout and Data Acquisition

The signal from the Wavelength Shifting (WLS) fibres is read out by an Avalanche Photodiode (APD), converting the scintillation light into electrical signal, with a high quantum efficiency of  $\sim 85\%$  and a gain of 100 [21]. An example APD is shown in Fig. 1.5. Both ends of each fibre are connected to one of the 32 pixels on the APD, with each APD reading out signal from one module. To maximise the signal to noise ratio, the APDs are cooled to  $-15^\circ\text{C}$  by a thermoelectric cooler, with heat carried away by a water cooling system.

The combination of the APD quantum efficiency and the light yield, determined by the PVC reflectivity and the scintillator's and WLS fibre's response, result in a signal requirement of at least 20 photoelectrons in response to minimum ionizing radiation at the far end of the FD cell.

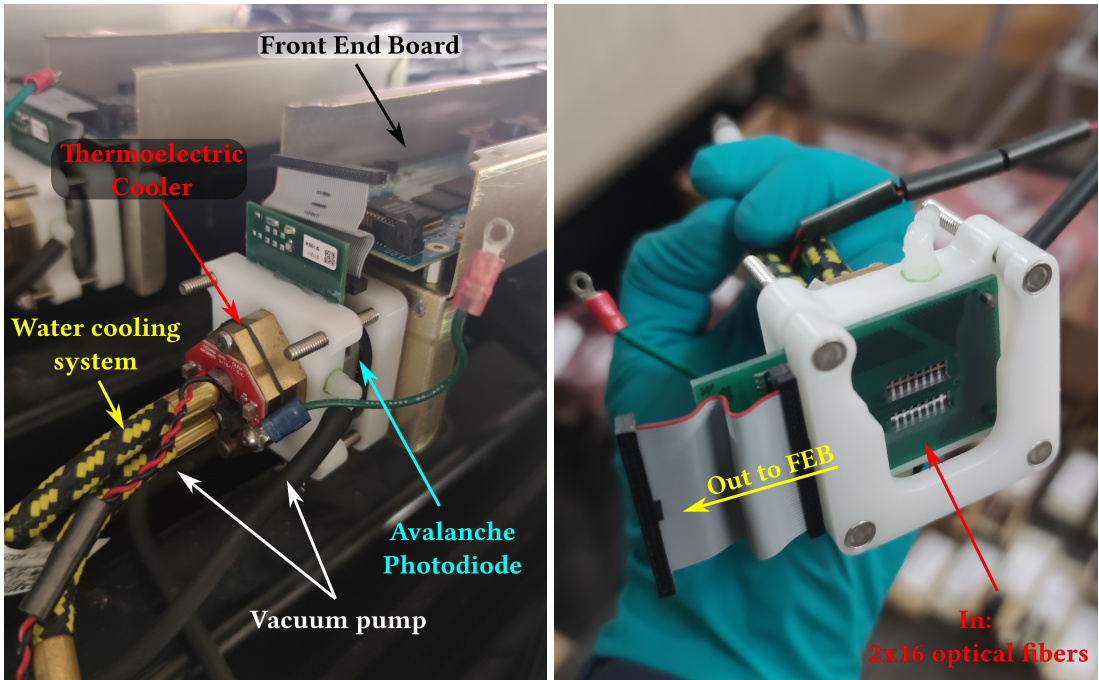


Figure 1.5: The modules with APDs for NOvA mounted on top of the detector on the left picture, and shown from the bottom on the right. The individual components of the module are described. The left picture shows a disconnected ribbon cable and ground cable, which are normally connected to the front end board.

Each APD is connected to a single Front End Board (FEB), shown in Fig. 1.6. The FEB amplifies and integrates the APD signal, determines its amplitude and arrival time, before passing it to the Data Acquisition (DAQ) system. On the FEB the APD signal is first passed to a custom NOvA Application-Specific Integrated Circuit (ASIC),

which is design to maximize the detector sensitivity to small signals. **ASICs** amplify, shape and combine the signal, before sending it to an Analog-to-Digital Converter (ADC). The combined noise from the **APD** and the amplifier is equivalent to about 4 Photo Electron (PE)s, which, compared to an average photoelectron yield from the far end of the **FD** cell of 30, results in a good signal and noise separation [21]. The digitized data from an **ADC** is sent to a Field Programmable Gate Array (FPGA), which extracts the time and amplitude of the **ADC** signals, while subtracting noise based on a settable threshold. The **FPGAs** employ multiple correlated sampling methods to reduce noise and improve time resolution of the signal [24].

**TO DO:** *Find out what is the pedestal/threshold that's being subtracted*

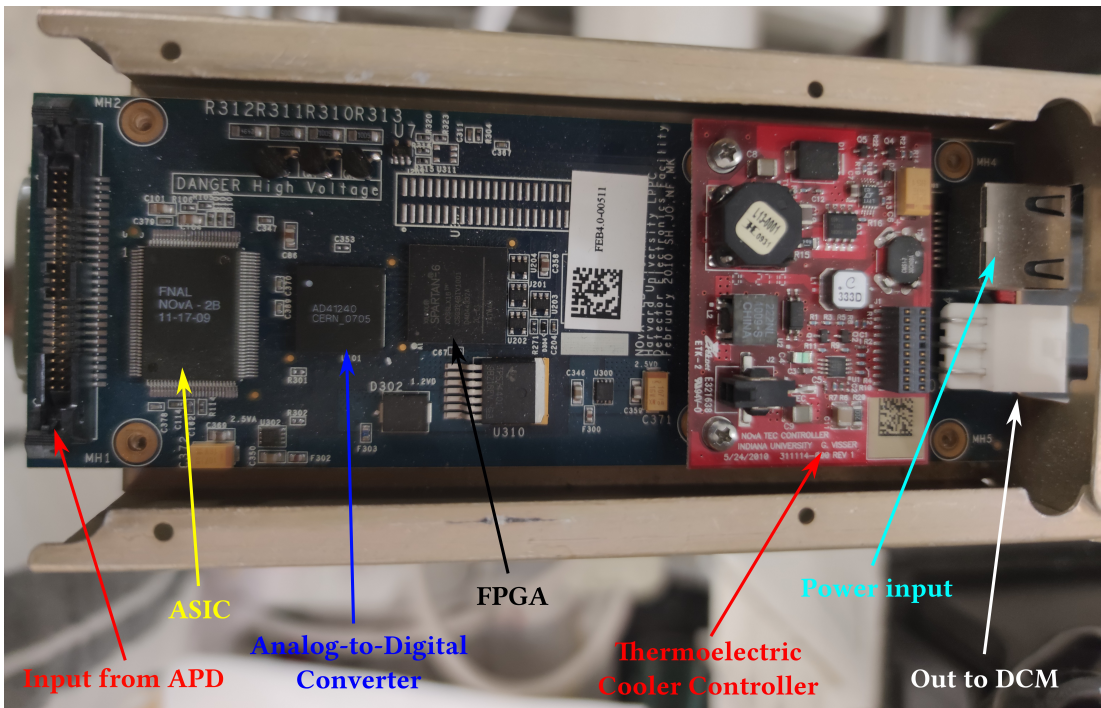


Figure 1.6: An example of a **NOvA FEB** with individual components labelled.

All of the **NOvA** front end electronics (**APDs** and **FEBs**) are operated in a continuous readout mode, without requiring any external triggers [21]. Due to higher detector activity during beam spills, the **ND FEBs** work at a higher frequency of 8 MHz, whereas the **FD FEBs** suffice with 2 MHz sampling frequency [24].

Data from up to 64 **FEBs** are concentrated in a Data Concentration Module (DCM), which concatenates and packages the data into 5 ms time slices, before sending it to the buffer nodes. **DCMs** are also connected to the timing system and pass a single unified timing measurement to the **FEBs** to maintain synchronization across the de-

tector [24].

The buffer nodes cache the data for at least 20 seconds while receiving information from the trigger system. Each trigger uses a time window based either on the time of the **NuMI** beam spill, on a periodic interval for readout of cosmic events for detector calibration and monitoring, or on a time of activity-based data-driven trigger [24]. Data that fall within any of the trigger windows are sent to a data logger system, where they are merged to form events, before being written to files for offline processing, or sent to an online monitoring system.

*TO DO: Talk about data quality as well, since I talk about good runs and bad channels in the TB calib chapter*

## 1.4 Simulation

*COMMENT: Should I divide the simulation into the individual stages? I had it like that originally, but for example the simulation of cosmics is only very short and not sure what section would I put it under*

To extract neutrino oscillation parameters, or to test a hypothesis, **NOvA** uses a series of simulations to make predictions according to various physical models [25]. The simulation chain can be divided into four parts: simulation of the neutrino beam, simulation of neutrino interactions within the **NOvA** detectors, simulation of cosmic particles interacting in the **NOvA** detector and simulation of the detector response.

To simulate the neutrino beam, **NOvA** uses the GEANT4 v9.2.p03 [26] based Monte Carlo (MC) simulation with a detailed model of the **NuMI** beamline [27], as it was described in Sec. 1.4. The simulation starts with **MI** protons interacting within the long carbon target and producing hadrons, mainly  $\pi$ ,  $K$  and  $p$ , followed by transport and possible further interaction of these hadrons within the focusing system, until finally ending with hadron decays producing the neutrino beam.

To account for the imprecise theoretical models used in GEANT4, we use the Package to Predict the Flux (PPFX) to incorporate external measurements of yields and cross sections of hadron production inside the target and other **NuMI** materials into the prediction [28]. The current version of **PPFX** is limited by the results available during its creation and only corrects the most frequent interactions while assigning

large systematics uncertainties to the rest (see Sec. 1.8). For the most common  $\pi$  production, **PPFX** uses the NA49 measurements [29] of 158 GeV/c protons interacting on a thin (few percent of interaction length) carbon target, with a few data point from Barton et al [30] to expand the kinematic coverage. These then have to be scaled to the 20 – 120 GeV/c incident proton energies seen in **NOvA** using the FLUKA [31, 32] **MC** generator. For the  $K$  production from  $p + C$  interaction, important for higher neutrino energies and electron neutrinos, **PPFX** uses the NA49  $K$  data [33] together with the NA49  $\pi$  data [29] multiplied by the  $K/\pi$  ratios of yields on thin carbon target from the MIPP experiment [34]. Lastly, for the nucleon production, **PPFX** uses the NA49 data on quasi elastic interactions [35]. All the other interactions inside **NuMI**, such as interaction in non-carbon targets, or interactions with hadrons other than protons, are either extrapolated from the previously mentioned measurements, or are not corrected for and a significant systematic uncertainty is assigned to them [28].

There's two new experiments that measured the production and interaction of hadrons on various targets and incident energies, specifically designed to improve the prediction of neutrino beams. I worked on implementing data from the NA61 experiment on hadron production from  $p + C$  interaction on a thin carbon target at 31 GeV/c [36], motivated by possible reduction in the  $K$  production systematic uncertainty. This work is still ongoing and will be implemented into **PPFX** and **NOvA** together with the rest of the NA61 measurement. The most impactful ones will be the measurement of hadron production from  $p + C$  interaction on a thin carbon target at 120 GeV/c [37] (no energy scaling required), measurements of  $p + C$  and  $p + Be$  at different incident energies [38],  $\pi + C$  and  $\pi + Be$  measurements at 60 GeV/c [39], resonance production measurements from 120 GeV/C  $p + C$  [40], and probably the most impactful one, the yet unpublished measurement of hadron production yield on a **NOvA**-era **NuMI** replica target at 120 GeV/c [41]. NA61 also measured the hadron production yield for the Tokai to Kamioka (T2K) experiment's replica target [42], which significantly reduced the neutrino flux systematic uncertainty for the **T2K** measurements [41]. The second experiment is EMPHATIC [43], which is currently analysing their data on a broad range of hadron production measurements, mainly the secondary and tertiary interactions of various projectiles with a wide range of in-

cident energies and thin target materials, complementary to the NA61 measurements.

*COMMENT: The description of neutrino interactions, including QE/Res/DIS scattering and nuclear effects will probably be in the theory chapter. If not I'll add it here.*

*COMMENT: Might have to describe some of these interaction models a bit more if any of the cross section uncertainty for the magnetic moment analysis turns up to be significant*

The output of the neutrino beam simulation is passed to the simulation of neutrino interactions inside the detectors, which is done with the GENIE v3.0.6 [44] neutrino MC generator. GENIE allows users to choose the particular models for different types of neutrino interactions and particle propagation within the nucleus, as well as possible tunes to external measurements. The four main interaction modes in GENIE are the Quasi Elastic (QE) CC scattering, the Resonant baryon production (RES), the Deep Inelastic Scattering (DIS), and the Coherent pion production (COH $\pi$ ). Special case of CC interaction with two nucleons producing two holes via Meson Exchange Current (MEC) is also considered. Particles created in these processes are then propagated inside the nucleus according to the Final State Interaction (FSI). All of these are set by the Comprehensive Model Configuration (CMC) and NOvA currently uses the N1810j0000 CMC. Additionally, NOvA adds a tune to NOvA  $\nu_\mu$ CC data for the CCMEC interactions and a set of external  $\pi$  interaction measurements to constrain the FSI model. Table 1.1 shows the list of models and tunes for different interaction modes in NOvA [7].

Table 1.1: Models and tunes used in the NOvA simulation of neutrino interactions.

Interaction	Model	Tune
CCQE	València [45]	External $\nu$ – D data [46]
CCMEC	València [47, 48]	NOvA $\nu_\mu$ CC data
RES & COH $\pi$	Berger-Sehgal [49, 50]	External $\nu$ – A data
DIS	Bodek-Yang [51, 52]	External $\nu$ – A data
FSI	Semi-classical cascade [53]	External $\pi$ – $^{12}$ C data

Since the FD is on the surface we also need to include a simulation of cosmic rays generated with the Cosmic-Ray Shower Generator (CRY) [54] MC generator. The simulated cosmic muons are also used to calibrate NOvA detectors [28].

Particles that are created from neutrino interactions and cosmic rays are propagated through the NOvA detectors using an updated version of GEANT4 v10.4.p02 [26].

The output of this simulation is the energy deposited in the scintillator, which is then passed to a custom **NOvA** simulation software [28]. The scintillation light generated by the deposited energy is parametrized using the Birks-Chou model [55], which corrects for recombination in organic scintillators at high deposited energies. The normalization factors for the produced scintillation light (the light yield), as well as for the Cherenkov light, which can affect the light readout, are tuned to **NOvA** cosmic data [9]. The light collection by the **WLS** fibres and its transport to the **APDs**, as well as the **APD** response use a parametrized simulation, which makes use of the fact that all the **NOvA** cells and their readout are generally the same across the detectors [28]. The simulation of the readout electronics is done by another custom **NOvA** parametrized model, which mainly account for a random electronics noise, with output in the same format as raw data.

Due to the high neutrino rate in the **ND**, there are neutrinos interacting in the surrounding rock creating particles that make it to the detector and act as background. To simulate these rock events we use the same simulation as for neutrino interactions inside the detector. However, since only a few particles make it into the detector, it would be very time consuming to run this simulation for every neutrino. Therefore, we create a separate simulation that includes the surrounding rock and then overlay the results into the normal **NOvA** simulation chain, which doesn't include the rock, so that the rate matches the **NuMI** neutrino rate [28].

## 1.5 Data Processing and Event Reconstruction

Both data and simulation events for all **NOvA** detectors are passed through the same event reconstruction and particle identification algorithms. The reconstruction was specifically developed with the  $\nu_e$  appearance search in mind, focusing on identifying the  $\nu_e$ **CC** signal against the  $\nu_\mu$ **CC** and Neutral Current (NC) backgrounds. Each **NOvA** detector has to deal with a different challenges, with multiple neutrinos interacting in the **ND** during one beam spill, and a large cosmic background in the **FD** [56].

The readout from each cell from the **DAQ** (see Sec. 1.3) is called a *channel* and the **DAQ** output from each channel is called a *raw hit*. **DAQ** groups hits into  $550\,\mu\text{s}$  windows and passes them to an offline reconstruction chain [56]. Reconstruction

starts by grouping hits into *slices* based on their proximity to other hits in both time and space [57]. **COMMENT: Maybe include rawhit to cellhit to recohit**

For events that produce hadronic and electromagnetic showers, we first identify lines through major features using a modified Hough transform [58]. These lines representing momentum directions are then passed to the Elastic Arms algorithm [59] to identify *vertex* candidates from their intersection points. Hits are then clustered into *prongs*, group of hits with a start point and a direction, using a k-means algorithm called FuzzyK [60, 61]. Here "fuzzy" means that each hit can belong to multiple prongs. Prongs are first created separately for each view (also called 2D prongs) and then, if possible, view-matched into 3D prongs (or just prongs) [56]. Figure 1.7 shows an example simulated electron shower with the reconstructed vertex (red cross) and prong (red shaded area) grouping all hits that should be a part of the shower together, while removing background hits in grey.**TO DO: Describe the Cosmic Ray Vertex used for data-based simulation**

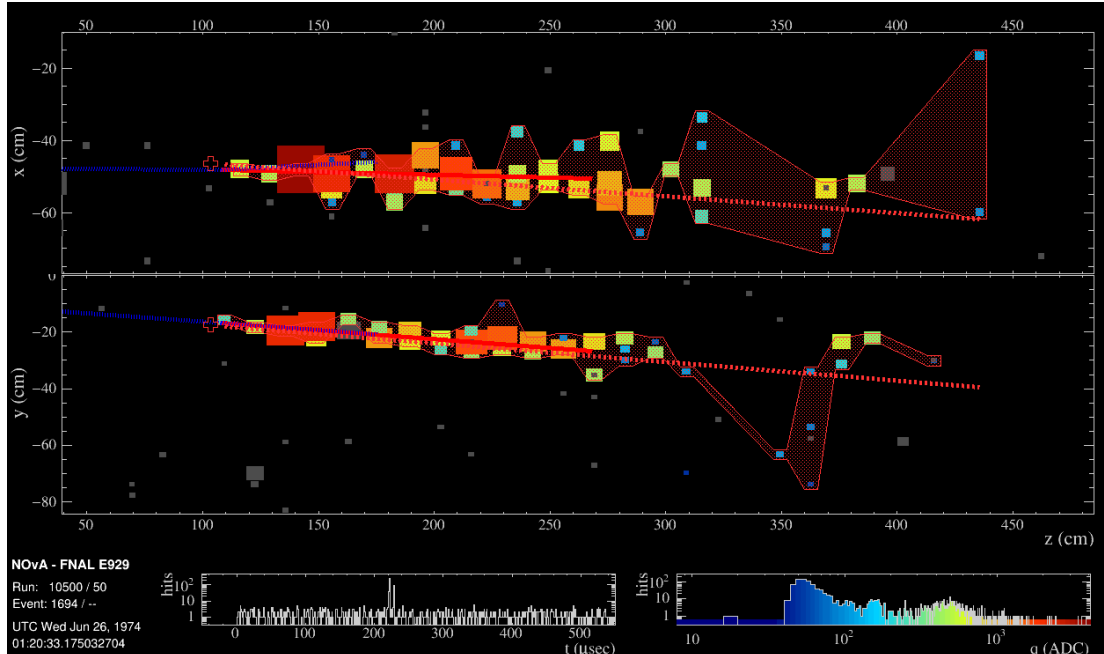


Figure 1.7: Reconstruction of a simulated single electron event in the **NOvA ND**. The red cross is the reconstructed vertex, the shaded area shows the cluster of hits into a shower and the dotted red line shows the estimated momentum of that shower. The blue dotted line shows the true momentum of the scattering neutrino and the solid red line the true momentum of the scattered electron. Figure from internal **NOvA** database.

For particles that are represented by tracks rather than showers (especially muons) we take the slice hits and form the *Kalman tracks* based on a Kalman filter [62]. In

addition to the start point and the direction, which exist also for prongs, tracks also contain information on the vector of trajectory points that make up the track and on the end point - and therefore on the track length. A parallel tracking algorithm takes in the Elastic Arms vertex and the Fuzzy-K 3D prongs and forms Break Point Fitter (BPF) tracks [63, 64], using a model of Coulomb scattering and energy loss. BPF tracks also contain 4-momentum information based on various particle assumption, most notably muon assumption. For cosmic particles, mostly muons, we use another track reconstruction algorithm, called the window cosmic track algorithm [65]. The window cosmic track algorithm uses a sliding 5 plane-long window, starting from the end of the detector, in which it fits a straight line to the recorded hits, before sliding the window forward and repeating the process. This way it accounts for possible Coulomb scattering of cosmic muons.

To identify individual particles and remove backgrounds, **NOvA** uses several Machine Learning (ML) algorithms, outputs of which are used in for Particle Identification (PID) in various **NOvA** analyses. The most common topologies for particles interacting in **NOvA** detectors are shown in Fig. 1.8. Muons are easily identifiable as a single long track which decays into an electron (or positron) if it stops inside the detector. Both electrons and  $\pi^0$ 's produce electromagnetic showers, but thanks to the low-Z composition and high granularity of the detector, there is a gap between the interaction vertex and the electromagnetic shower.

**NOvA** employs a Convolutional Neural Network (CNN) based on the GoogLeNet [66] architecture named Convolutional Visual Network (CVN) [67], which uses slice hits to classify interactions into one of the four categories:  $\nu_e$ ,  $\nu_\mu$ ,  $\nu_\tau$ , **NC**, or cosmic. Since this algorithm identifies the entire event it is also sometimes called *EventCVN*. The same architecture, but applied to the Fuzzy-K prongs and called *ProngCVN* [68], is used to identify the individual prongs based on what particles they most likely correspond to. This is useful to assign in the calculation of the prong energy, as described in Sec. 1.7. A special **ML** algorithm for identifying muons, based on a Boosted Decision Tree (BDT) with inputs from the Kalman track, is called Reconstructed Muon Identifier (REMid) [62].

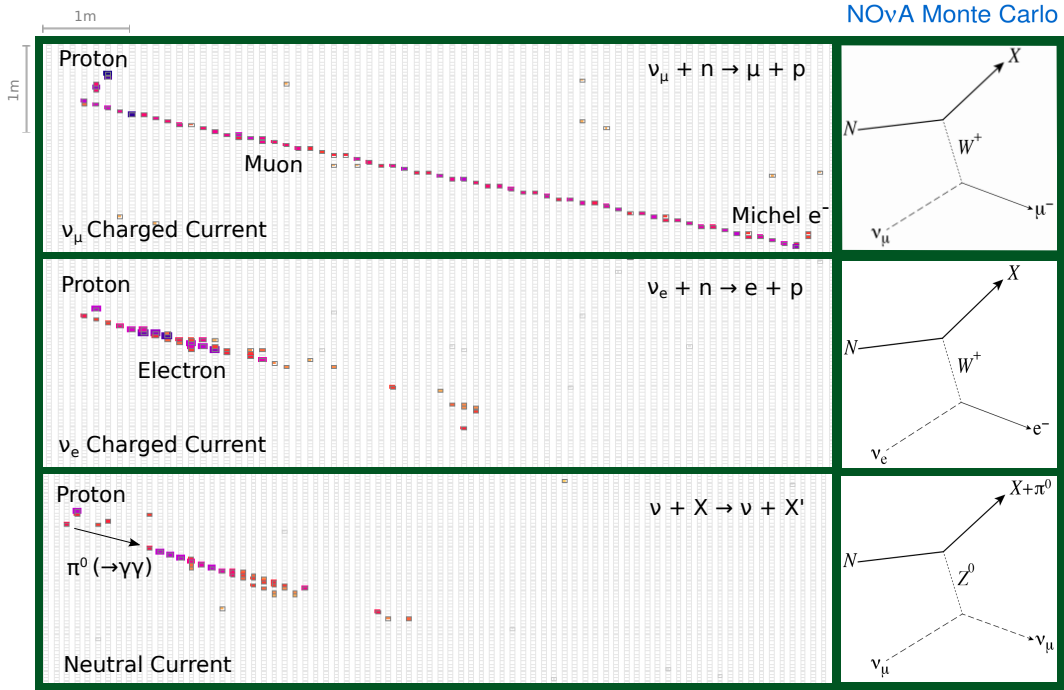


Figure 1.8: Different event topologies as seen in the **NOvA** detectors with corresponding Feynman diagrams [56]. Each event is a simulated 2.15 GeV neutrino interacting in a **NOvA** detector producing a 0.78 GeV proton and a second 1.86 GeV particle depending on the interactions type. The figure show one view and the colouring represents the deposited energy.

## 1.6 Detector Calibration

The energy deposited within the **NOvA** detectors is represented by the peak **ADC** values for each cell the particle passed through, which are obtained from the readout electronics, as described in Sec. 1.3. To convert **ADC** into physical units we need to calibrate the **NOvA** detectors [69], while accounting for the attenuation of light along the **WLS** fibres, or for differences between individual cell. The purpose of calibration is to calculate a conversion factor from  $\text{ADC} \rightarrow \text{MeV}$  units, so that the same energy deposited at any place within any detector and at any time, is recorded as the same value.

**NOvA** uses cosmic ray muons for calibration due to their abundance in the **NOvA** detectors and a consistent energy deposition. We use hits from a subsample of muons stopping inside the detectors, from a window when they are almost exactly minimum ionising particles (MIP), to calculate the absolute energy scale. The cosmic muons are collected using a periodic trigger with the same length as the beam trigger, removing

events with timestamps overlapping with the beam spill window. For the simulation of cosmic muons we use the CRY [54] MC generator, as outlined in Sec. 1.4.

*COMMENT: I talk about this selection later on in the Test Beam calibration chapter when I talk about the data-based simulation. Should I therefore elaborate more on this or is this enough?* We reconstruct the cosmic muon tracks using the window cosmic track algorithm explained in Sec. 1.5. To select good quality cosmic tracks we require that at least 80% of all hits from the reconstructed slice contribute to the track [70]. Additionally, all tracks must cross at least 70 cm along the z axis and must have at least 20% of their total track direction in the z axis, since very vertical tracks tend to not be reconstructed well. *COMMENT: There are additional selection criteria which are not as important, do I need to mention them?* To select stopping muons we look for Michel electrons, which get produced by decaying muons at the end of their tracks, as can be seen on the top panel of Fig. 1.8.

Since the energy deposited in a cell is proportional to the distance the particle travels through the cell, we use the value of the deposited energy divided by the path length through the cell as the input variable for calibration. To ensure we use precise estimate of the path length, we only use hits that satisfy the *tri-cell* condition, shown in Fig. 1.9. This means that for each hit there must be a corresponding hit in both of the surrounding cells in the same plane for the same track. This allows us to calculate the path length simply from the height of the cell and the angle of the reconstructed track. In case there is a bad channel in a neighbouring cell (right side of Fig. 1.9), we ignore this channel and look one cell further. We can then calculate the path length simply as the cell width divided by the cosine of the direction angle [69]. In case the tricell condition fails, we also evaluate the "Z *tri-cell*" condition, which requires a hit in both neighbouring planes in the same cell and in the same view. These "Z tricell" hits are saved in a separate histogram and are only used if there are no hits that would satisfy the original tricell condition. This is especially useful for the cell on the edge of the detector, which fail the tricell condition by design, as they only have one neighbouring cell in the same plane.

The calibration conversion factor from the signal recorded by the detector readout

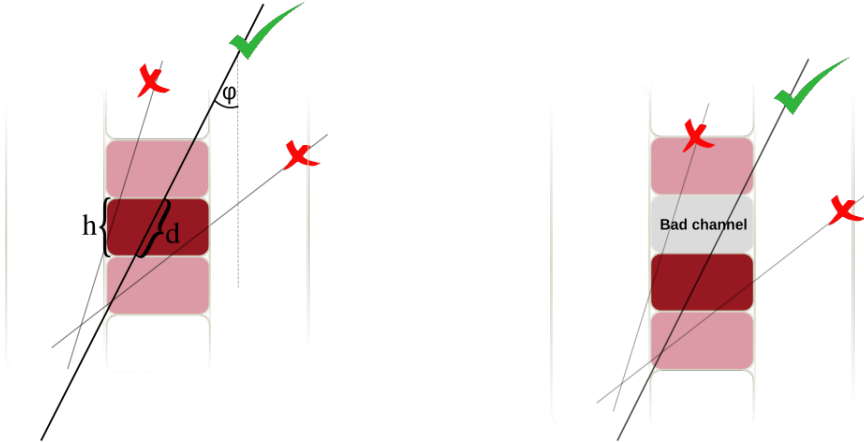


Figure 1.9: Illustration of the tricell condition. We only use hits that have two surrounding hits in the same plane to be used in the **NOvA** calibration, shown on the left plot. This is to ensure a good quality of the path length ( $d$ ) reconstruction, which is calculated from the known cell height ( $h$ ) and the reconstructed track angle ( $\varphi$ ). In case the hit is next to a bad channel, as shown on the right plot, we ignore this bad channel and require a hit in the next cell over.

and the actual deposited energy can be expressed by Eq. 1.1.

$$E_{dep} \text{ [MeV]} = \text{Signal [ADC]} \times S_d \times TS_{d,i} \times R_{d,i}(t) \times A_d(t). \quad (1.1)$$

Here we can see that calibration consists of four separate and complementary factors: the Scale ( $S_d$ ), the Threshold/Shielding correction ( $TS_{d,i}$ ), the Relative calibration ( $R_{d,i}(t)$ ) and the Absolute calibration ( $A_d(t)$ ), all described below. Each part is calculated for each detector separately, as indicated by the subscript  $d$ . The Relative and Absolute calibrations are calculated for each time period separately to account for possible changes in the energy deposition throughout the time, possibly caused by the ageing of the scintillator oil, or of the readout electronics. The time periods are either determined by running conditions and separated by significant changes to the readout or **DAQ** systems, including the summer shutdown, or by a fixed time interval.

The Threshold/Shielding correction and the Relative calibration calculate a calibration factor for each position within the detector to account for variations caused by the attenuation of light as it travels through the **WLS** fibres, or by differences between individual cells. This is denoted as a subscript  $i$  in Eq. 1.1. For data, the position of hit in a detector is described by the plane number, the cell number and the position within the cell ( $w$ ).  $w$  is calculated as the projection of the cosmic track to the central cell axis and its value is equivalent to the X axis (Y axis) coordinate of the projection

for the horizontal (vertical) cells, with the 0 value at the centre of the cell [69].

For simulation, we do not use the plane number to determine the position within a detector, as by construction all detector planes should have the exact same readout. This significantly reduced the requirements for the number of events that need to be simulated, reconstructed and calibrated, especially for the FD with 896 planes. However, in reality there are some variations in detector response between individual planes, caused by different *brightness* qualities of the fibres, zipped or twisted fibres, different qualities of the scintillator, possible air bubble, or potentially others. Since we want to include these differences into simulation without having to simulate every cell individually, we divide all cells into 12 equally populated Fibre Brightness (FB) bins based on the uncorrected average response in the center of that cell, as shown in Fig. 1.10. These brightness bins describe the relative differences in the detector response between individual cells [71].

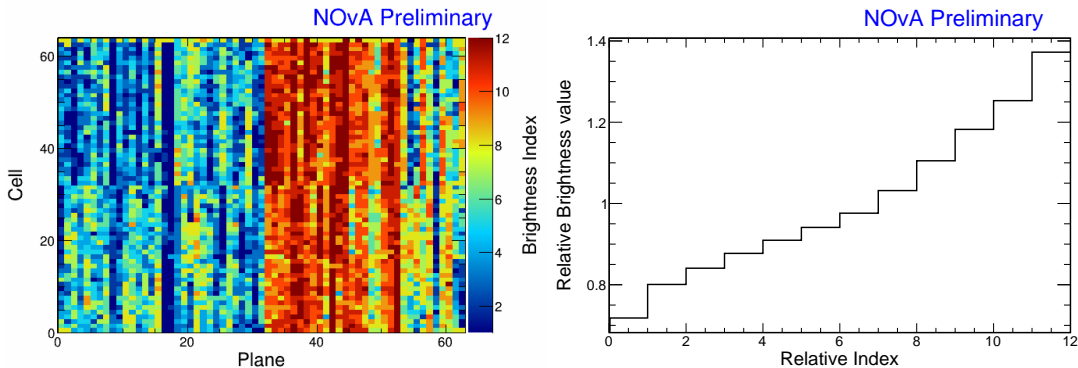


Figure 1.10: Distribution of the NOvA detector cells into 12 brightness bins (left plot), each representing a relative difference in energy response (right plot) due to different brightnesses of the fibres, scintillators, or readout. This is an example from the NOvA Test Beam detector, where the left side of the detector (planes 1-32) has clearly lower response relative to the right side of the detector (planes 33-64).

### 1.6.1 Scale

The Scale calibration factor from Eq. 1.1 is a simple conversion from the peak ADC value into the number of PEs. This factor only depends on the APD gain (which was different in the beginning of NOvA data taking) and on the FEB type (different between detectors, as described in Sec. 1.3).

### 1.6.2 Threshold and Shielding Correction

The Threshold and Shielding correction accounts for two assumptions, which hold true in most cases in NOvA, but fall short for some hits at the bottom of the detector, or far away from the readout, especially for the **FD** [69]. The first assumption is that the **ADC** response to the photon signal is linear, which is mostly true except close to the **APD** threshold. Energy deposited far away from the readout may produce photons that get attenuated enough to be shifted below the threshold. However, due to natural fluctuation, the same deposited energy may also produce photons that would make it over the threshold, therefore making it appear that the actual deposited energy was higher than in reality, introducing a bias to the calibration. The threshold correction is calculated using simulation, as the ratio between the number of simulated **PE** seen by the **APD** ( $\text{PE}_{\text{true}}$ ) and the Poisson mean number of simulation photons created in the scintillator by the same deposited energy ( $\lambda$ ).

The second assumption is that the spectrum of cosmic muons is uniform within each detector. Again, this is generally true, but breaks down at the **FD**, which is big enough that the top of the detector shields the bottom part of the detector and affects the energy distribution. The shielding correction is calculated from simulation as a ratio between the true energy deposited by a charged particle ( $E_{\text{true}}$ ) and the expected deposited energy if the particle was **MIP** ( $E_{\text{MIP}}$ ).

The total Threshold and Shielding correction is calculated for simulated events in each cell, **FB** bin and  $w$  position according to Eq. 1.2. The final correction is a fit to the mean correction value along  $w$  in each cell and **FB** bin.

$$TS_i = \frac{\text{PE}_{\text{true}}}{\lambda} \frac{E_{\text{true}}}{E_{\text{MIP}}} \quad (1.2)$$

### 1.6.3 Relative Calibration

Relative calibration corrects mainly for the attenuation of the scintillator light as it travels through the **WLS** fibre to the readout. Since the correction is calculated for each cell independently, it effectively correct for the relative differences between detector cells as well. The result of the Relative calibration is the detector response to a particle in the units of Corrected Photo Electrons (**PECORR**), which is calculated as the ratio between an average response in **PE** across the entire detector (can differ across

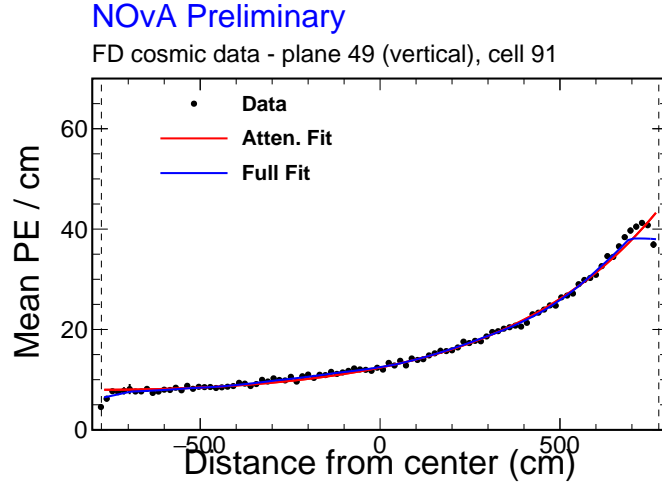


Figure 1.11: Example attenuation fit for a single cell in the NOvA FD across its full length, as shown by dashed vertical lines. The red line shows the initial exponential fit and the blue line shows the full fit after the LOWESS correction, both described in text. Figure from [72].

detectors) and the result of the “*attenuation fit*” in that particular position within the detector. This way the **PECORR** should be uniform across the detector along the plane number, cell number and  $w$  distributions [69].

To do the attenuation fit, we first create the “*attenuation profiles*” for each detector cell. Attenuation profiles are profile histograms of mean detector response over the travelled path length, in the units of PE/cm, along the position within the cell. An example attenuation profile is shown in Fig. 1.11 as black dots. We then apply the Threshold and Shielding correction described above before doing the attenuation fit, which consists of two steps.

1. The first step is a three-parameter exponential fit according to Eq. 1.3

$$y = C + A \left( \exp\left(\frac{w}{X}\right) + \exp\left(-\frac{L+w}{X}\right) \right), \quad (1.3)$$

where  $y$  is the fitted response,  $L$  is the length of the cell and  $C$ ,  $A$  and  $X$  are the fitted parameters representing the background, attenuation scale and attenuation length respectively. An example of the exponential fit is shown as a red curve in Fig. 1.11.

2. The second step is smoothing out of the residual differences between the exponential fit and the original distribution with the Locally Weighted Scatter plot

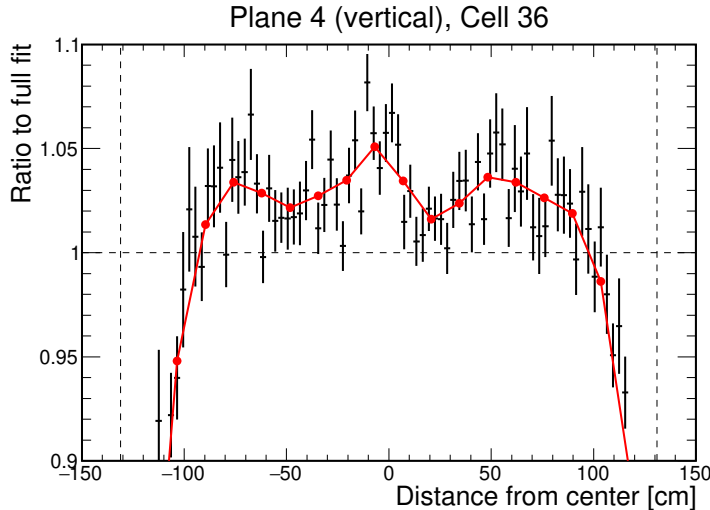


Figure 1.12: Example [LOWESS](#) correction for the residual differences after the exponential part of the attenuation fit of the [NOvA](#) Relative calibration. This is an example for a single cell in the [NOvA](#) TB detector with black point showing the residual differences and red line the [LOWESS](#) correction, both described in text.

Smoothing ([LOWESS](#)) method, shown in Fig. 1.12. We use 20 points across the length of each cell to create a smoothed distribution of the residual values. Result of the [LOWESS](#) correction is then combined with the exponential fit into the full attenuation fit, shown as a blue line in Fig. 1.11.

Even after an application of the [LOWESS](#) correction, there are sometimes large differences between the attenuation fit and the fitted response. This is usually caused by a small number of events in that cell, common for cell at the edge of the detector. To ensure a good quality of the attenuation fit, we calculate the total  $\chi^2$  between the attenuation fit and the fitted response and only call a cell *calibrated*, if the final  $\chi^2 < 0.2$ . If  $\chi^2 > 0.2$ , we ignore the results for this cell and mark it as *uncalibrated*.

#### 1.6.4 Absolute Calibration

For the absolute calibration we only use hits from muons stopping inside the detector, 1 – 2 m from the end of their tracks. This is when they are approximately minimum ionizing particles and their energy deposition is well understood. We also remove hits at the edges of each cell, to mitigate the effects at the end of the [WLS](#) fibres and the lower number of events at the edge of the detector [70].

We apply the results of the relative calibration to the selected hits to get the distribution of the corrected detector response in the units of [PECorr/cm](#), as shown on

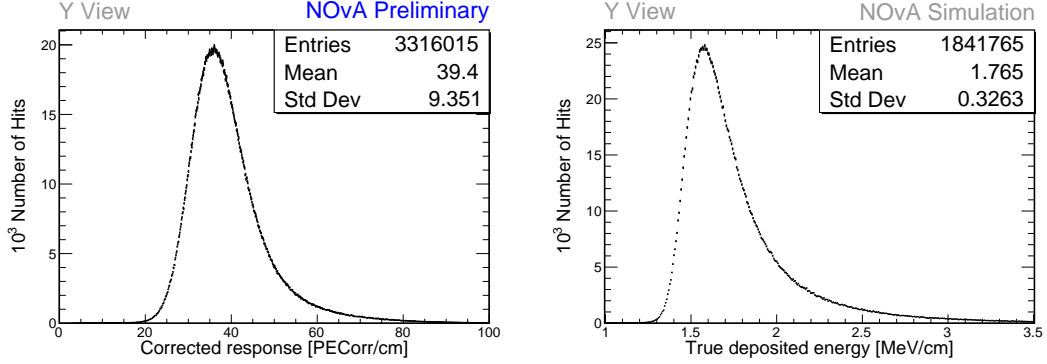


Figure 1.13: To calculate the absolute energy scale we take the mean reconstructed energy response (left) for selected stopping muons for each view and each data period or simulation, and use it to divide the simulated mean true deposited energy (right).

the left of Fig. 1.13. We then take the mean of this distribution, separately in each of the two views, and in each time period and simulation version, which we call the *reconstructed Muon Energy Unit* (MEU). Analogously, we take the mean of the true deposited energy in the units of MeV/cm from simulation, shown on the right of Fig. 1.13, and call it the *true MEU*. We then take the average over the two views and calculate the absolute energy scale for each time period and simulation version as the ratio on Eq. 1.4.

$$\text{Absolute Energy Scale} = \frac{\text{MEU}_{\text{True}} \text{ [MeV/cm]}}{\text{MEU}_{\text{Reco}} \text{ [PECorr/cm]}}. \quad (1.4)$$

We save these absolute energy scales, as well as the results of the attenuation fit, in a set of lookup tables, which are used any time a hit is recorded in the NOvA detector and processed through the NOvA data processing algorithms.

## 1.7 Energy Estimation

The deposited energy we get from the detector calibration (Sec. 1.6) is only the first step in estimating the neutrino energy ( $E_\nu$ ) required for the main NOvA analyses.

For the  $\nu_\mu$  disappearance analysis, the  $E_{\nu_\mu}$  is measured as the sum of the muon energy and the energy of the hadronic shower [7]. The energy of the muon is identified from the length of its track, without the need of the calibration results. The energy of the hadronic shower is estimated from simulation as a fit to the 2D distribution of the true  $E_{\nu_\mu}$  minus the reconstructed muon energy, versus the visible (not corrected

for the dead material) deposited energy of the hadronic system [68].

For the  $\nu_e$  appearance analysis, the  $E_{\nu_e}$  is calculated using a quartic fit to the 2D distribution of the electromagnetic and the hadronic calorimetric energies corrected for energy deposition in the dead material (PVC cells) [68]. The dead material correction is currently just a simple scaling of the deposited energy from calibration for all particles and it is calculated from the measurement of the  $\pi^0$  mass peak in the NOvA ND. This correction is correct only for electromagnetic showers and is not directly applicable to hadronic showers. The fit to determine  $E_{\nu_e}$  keeps the normalization of both the electromagnetic and the hadronic energies free, so the correctness of the dead material correction is not important. It is however used in other, non-neutrino oscillation analyses.

## 1.8 Systematic Uncertainties at NOvA

Systematic uncertainties in NOvA analyses arise from the imperfect knowledge on the individual components of the NOvA experiment, or from the known shortcomings of the prediction used to extract the results on the measured parameters. Even though different analysis in NOvA need to consider different systematic uncertainties and their effect on the results varies, there are a few commonalities across all NOvA analyses that are explained below.

Both the 3-flavour [7] and the sterile neutrino [13] oscillation analyses in NOvA use the ND to constrain the FD prediction, which significantly reduces the effect of the neutrino beam and interaction prediction systematic uncertainties. On the other hand, these are the leading sources of systematic uncertainties for the ND-only analyses, such as the cross section analyses [8–11]. The leading systematic uncertainty for the neutrino oscillation measurements comes from the detector calibration uncertainty. Significant uncertainties for all NOvA measurements also come from the neutron modelling, the detector simulation and the muon energy estimation. There are other sources of systematic uncertainties that are not mentioned here as they are sub-dominant, or specific to a certain analysis.

The systematic uncertainty on the prediction of the neutrino beam consists of two parts: the hadron production and the beam focusing uncertainties [28]. The

uncertainty for hadron production is estimated by the **PPFX** (describe in Sec. 1.4) using the multi-universe technique. Here we create 100 **PPFX** universes in which the inputs from the external measurements used to constrain the hadron production are randomly floated around their central values within their respective systematic uncertainties. Parts of the hadron production that are not constrained by external measurements are given a conservatively large systematic uncertainty. The beam focusing systematic uncertainties account for the uncertainties on the horn and target positions, the horn current, the beam position on the target, the beam spot size, and the effect of Earth's magnetic field in the beam pipe. **TO DO: Describe the beam PCA and how can we limit the beam uncertainty**

**TO DO: Describe the neutrino interaction modelling systematic uncertainties**

**TO DO: Describe the detector modelling systematic uncertainties** COMMENT: I should probably only discuss the new light level and cherenkov systematic uncertainties from the 3fl technote. This have not been published anywhere yet, but this is what I'm using for the mag. moment analysis

**TO DO: Describe the neutron uncertainty - why do we need it?** COMMENT: Should I describe MENATE or MCNP? Do I even need this here? Not sure if I'm including this in the mag. moment yet. Maybe add it only if I do...

**TO DO: Describe the calibration uncertainties**

**TO DO: Describe the muon energy scale uncertainty - if needed, maybe just briefly...**

## CHAPTER 2

# NOvA Test Beam Detector Calibration

The NOvA Test Beam experiment [73] is a sub-experiment of NOvA that aims to improve NOvA’s sensitivity to the neutrino oscillation parameters by improving our understanding of particle interactions and energy deposition in the NOvA detectors. The initial studies showed [74], that the Test Beam experiment has a potential to reduce the total systematic uncertainty on the three flavour oscillation parameters by about 10%.

The NOvA Test Beam experiment consists of a scaled down version of the NOvA detectors, placed in a test beam. Using a test beam allows us to study the response of tagged single particles with measured momenta and position in a NOvA detector. It also enables us to determine their energy resolution and the absolute energy scale without the use of a simulation. Additionally, we are able to compare the responses of the beam muons and the cosmic ray muons, to study fibre attenuation, or to validate the NOvA calibration process. The Test Beam detector was also equipped with a combination of ND and FD readout electronics and filled with a variety of NOvA scintillator oils, which enables us to make a comparison of their respective performance and particle responses [75].

All the aforementioned benefits of running the NOvA Test Beam experiment require, or benefit from, the Test Beam detector calibration. The calibration of the Test Beam detector follows the same calibration procedure as the standard NOvA detectors (outlined in Sec. 1.6), which allows for a direct comparison of the deposited energy in the Test Beam detector with the standard NOvA detectors. On top of that, the unique qualities of Test Beam allow us to use the Test Beam calibration to validate the calibration process and possibly to provide a simulation-independent absolute energy scale.

In this chapter we will introduce the NOvA Test Beam experiment in Sec. 2.1,

focusing on the Test Beam detector and especially on the aspects that could impact its calibration. In Sec. 2.2 we describe the new data-based simulation of cosmic muons that was developed for the Test Beam detector calibration as part of author’s PhD and in Sec. 2 we discuss the Test Beam detector calibration itself.

## 2.1 The NOvA Test Beam Experiment

The NOvA Test Beam experiment [76] consists of a scaled down version of the NOvA ND and FD, shown in Fig. 2.1, and a series of beamline detectors to measure and identify a range of particles from the MCenter beamline in the Fermilab Test Beam Facility (FTBF) [77].

The Test Beam detector started with commissioning runs in June 2019 and ran, with an exception of regular summer shutdowns, until July 2022, after which it was decommissioned. The Test Beam data taking is divided into *periods*, which are defined in Tab. 2.1. Period 1 only lasted for about a month and with only a half-filled detector, as explained below. It was therefore only used for detector commissioning and will not be used in any of the Test Beam physics analysis, or in the calibration.

Table 2.1: Test Beam detector data taking periods.

Period 1	June 3 <sup>rd</sup> 2019	-	July 6 <sup>th</sup> 2019
Period 2	December 5 <sup>th</sup> 2019	-	March 20 <sup>th</sup> 2020
Period 3	January 12 <sup>th</sup> 2021	-	June 27 <sup>th</sup> 2021
Period 4	November 30 <sup>th</sup> 2021	-	July 10 <sup>th</sup> 2022

Majority of the Test Beam detector and its instrumentation is identical to the other NOvA detectors, with a few exceptions that could have an impact on the calibration. We are going to identify and discuss these differences in this section.

### Beamline

The beam for the Test Beam experiment originates from the same 120 GeV Main Injector protons used in NuMI, extracted once a minute in a continuous 4.2 s spill [73]. The protons are impinged on a copper target producing mostly protons and pions, which are then directed towards a second target, producing the tertiary beam of particles used in the Test Beam detector. As can be seen in Fig. 2.1, we use two collimators

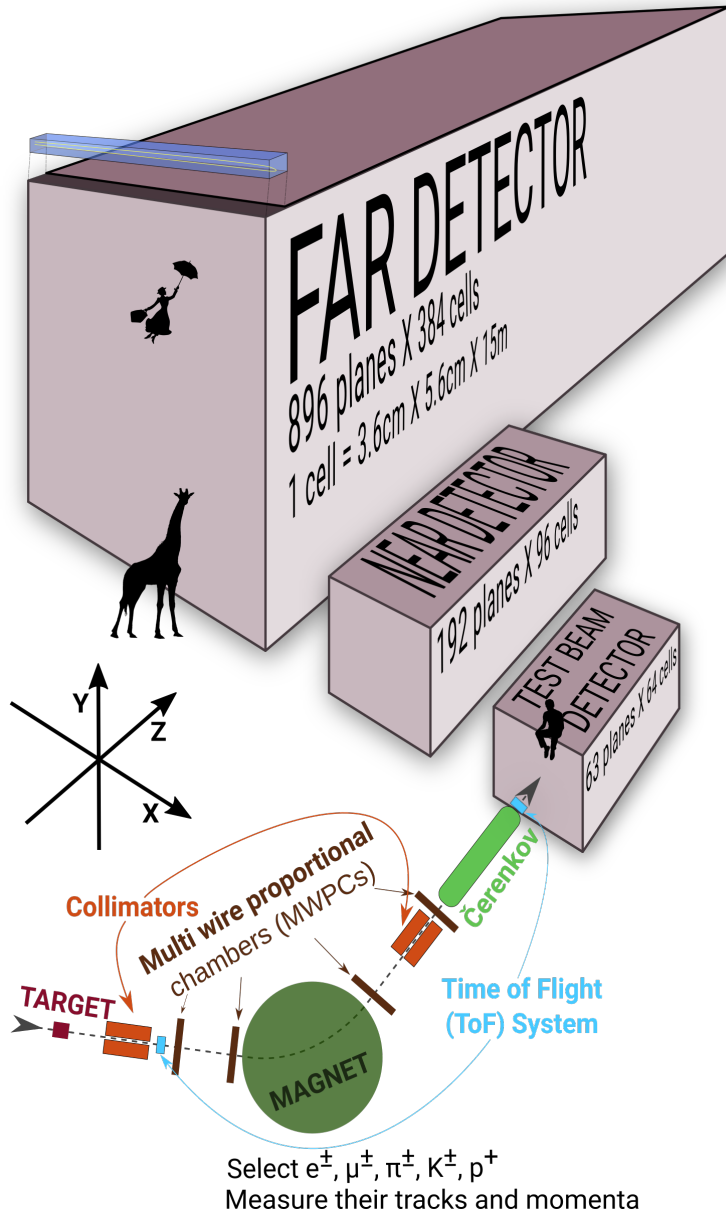


Figure 2.1: Comparison of Test Beam detector scale to the NOvA ND and FD (and a man, giraffe, or Mary Poppins). Also shown are the Test Beam beamline detectors and components (not to scale), with arrows showing the direction of the beam. The three black arrows show the orientation of the detector coordinate system.

to direct the tertiary beam and a magnet to select the desired momentum. Particle tracking is done using the four Multiwire Proportional Chamber (MWPC)s and particle identification is done with a combination of the Time of Flight (ToF) detectors and the Cherenkov detector, which is set for electron detection. There was an additional ToF detector installed ... during period ... **COMMENT: Where do I find the information on this?**

## Detector Parameters

The **NOvA** Test Beam detector consists of two 31-plane blocks, each beginning and ending with a vertical plane, with an additional horizontal plane glued in-between them to preserve the alternating pattern [78]. Each plane consists of 2 modules side-by-side, both made up of 32 cells. Each cell is 2.6 m long with an inner (without the PVC) depth and width of 5.9 cm and 3.8 cm respectively, same as for the other **NOvA** detectors. This brings the final dimensions of the Test Beam detector to 63 planes  $\times$  64 cells, or  $2.6 \times 2.6 \times 4.1 \text{ m}^3$ .

The 63 planes are numbered from 0 to 62, with even numbers corresponding to vertical planes and odd numbers to horizontal planes. Cells are numbered 0 to 63, going from bottom to top for horizontal planes and left to right, when facing the front of the detector, for vertical planes.

The detector coordinate system is illustrated in Fig. 2.1. It is centred with  $(0, 0, 0)$  in the centre of the first plane [79]. The x axis runs left to right when facing the front of the detector, y axis from bottom to top, and z axis goes along the beam direction from front to the back of the detector. Position within each cell ( $w$ ) is aligned with the x (y) axis for the horizontal (vertical) cells, with  $w = 0$  centred in the middle of each cell. The exact geometry of the Test Beam detector was measured in several alignment surveys and is saved in gdml files [80].

In the past we encountered an issue when trying to align the Test Beam detector with the beamline measurements by rotating the detector. This broke several assumptions within the Test Beam geometry [79] and manifested as uncalibrated cells in the back of the detector [81]. This was fixed by realigning both the detector and the beamline separately, based on the last alignment survey, measured during the decommissioning of the detector. *COMMENT: Should I keep this paragraph in or no?*

## Scintillator

Test Beam used a combination of the leftover **ND** and **FD** production scintillator oils and the oil drained from the **NDOS** test detector. The used scintillator oils also differ in the way they were stored since the **ND** and **FD** filling, or the **NDOS** draining, which apparently impacted its quality. These factors have a significant effect on the energy deposition within them. The distribution of individual scintillator oils and the relative

difference in their energy response can be seen in Fig. 2.2.

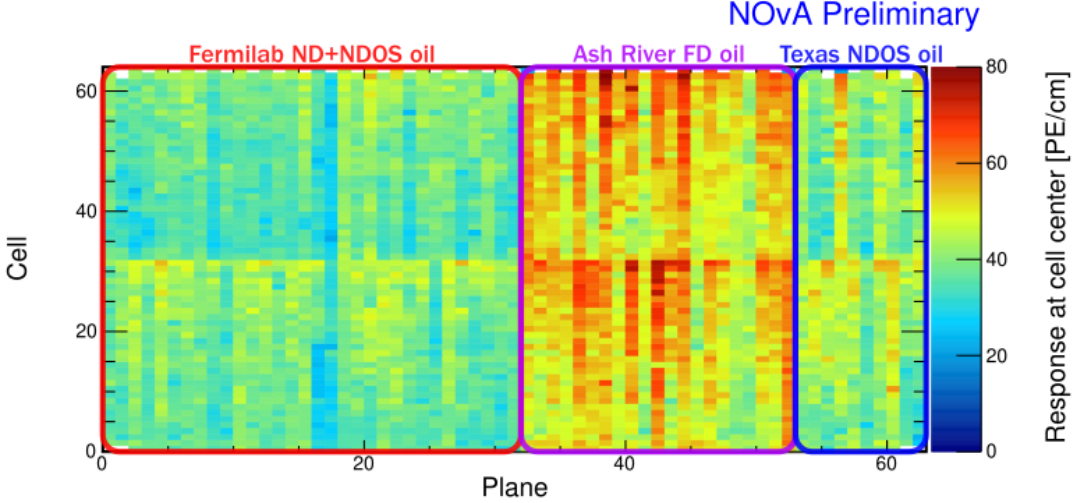


Figure 2.2: Uncorrected energy response in the centre of cells across the Test Beam detector showing a clear distinction between the different scintillator oils, labelled with coloured boxes and descriptions.

We can distinguish four samples of NOvA scintillator oil used in the Test Beam detector:

1. Mixed ND production oil and NDOS-drained oil stored in a tanker and four tanks outside in FERMILAB [82];
2. Separate ND production oil and NDOS-drained oil stored underground in barrels at the MiniBooNE<sup>1</sup> cavern [74];
3. FD production oil stored inside in Ash River in "totes" under several layers of black plastic [84];
4. NDOS-drained oil stored mainly inside at Texas A&M University and University of Texas at Austin [85, 86].

The original plan [87] was to only use the tanker/tank scintillator (sample #1). First tests showed acceptable results and the tanker oil was used to fill out almost the entirety of the first block of the detector (first 32 planes) [82]. However, when we loaded oil from tank #2 into the tanker, it became extremely cloudy and unusable, possibly due to contamination with water accumulated at the bottom of the tanks.

---

<sup>1</sup>MiniBooNE [83] is a FERMILAB experiment located close to the NOvA ND

The rest of the first block was therefore topped up with high quality scintillator from **NDOS** (sample #2). This is labelled as "FERMILAB ND+NDOS oil" in Fig. 2.2.

The first 21 planes of the second block (planes 32 to 52) were filled with the **FD** production scintillator shipped in from Ash River (sample #3) [88]. We again topped up these planes with the **ND+NDOS** scintillator (sample #2).

The last 10 planes (planes 53 to 62) [88] were filled with the "Texas" scintillator (sample #4), which has higher light yield than the one from the tanker, but lower than the Ash River one [85].

In total the Test Beam detector is filled with 5418 gallons of scintillator oil with a weight of approximately 28.6 tons [78].

## Readout

The Test Beam detector uses in total 126 **FEBs**, each reading out signal from 32 cells [78]. The readout is located on the top and right side (when looking at the front) of the detector. 118 **FEBs** are version 4.1, same as in the **FD**, and 8 **FEBs**, located in pairs on planes 16, 17, 48 and 49, are version 5.2, same as in the **ND**. As was described in Sec. 1.3, the **ND FEBs** are designed to read out data in a fester rate and we used a mix of **FEB** types to study the difference in their response and to validate both versions in the same environment [89].

## Environment

Unlike the **ND** and the **FD**, the Test Beam detector does not have any overburden to shield it from cosmic particles, which affects their rate and energies inside the detector. There is also less precise control of temperature and humidity than in the other detectors [source?], which can potentially impact the scintillator and readout performance. *TO DO: Finish this description of environmental control, maybe mention HVAC? - depends how much I want to talk about this effect...*

## Underfilled Cells Issue

The Test Beam detector is slightly tilted around the z axis by about  $0.7^\circ$  towards the readout. This caused the top cells of both modules of all the horizontal planes (cells 31 and 63) to be underfilled, creating an air bubble on the left side of the detector and

severely affecting the energy response in those cells [89]. This has been fixed [90] during the period 3 running by adding extensions to the filling ports and overfilling the horizontal cells with the **ND+NDOS** scintillator (sample #2 from the scintillator description). More details on this issue and its effects and on how it was handled in calibration are detailed in Sec. 2.3.5.

## 2.2 Data-based Simulation of Cosmic Muons

The standard **NOvA** calibration procedure described in Sec. 1.6 uses the **CRY MC** generator (see Sec. 1.4) to create the simulated cosmic ray sample for calibration. However, the **CRY** simulation proved to be highly inefficient, with only a small fraction of the simulated cosmic-ray activity resulting in selected calibration hits and the majority of particles failing to even hit the detector. This inefficiency consumed significant processing resources, disk space, and file usage. Moreover, the momentum and angle distributions in **CRY** were not well suited to the **NOvA** sites, potentially impacting the calibration accuracy.

To overcome these challenges, we developed and implemented a data-based simulation that eliminates the need for the **CRY MC** generator. Instead, we use a subset of the cosmic data sample used in calibration and pass it through the beam removal filter, reconstruction chain and a selection of high-quality cosmic muons. The selected cosmic muon events are then used as inputs to the detector simulation to create a new simulated cosmic ray sample.

This approach results in a near-perfect efficiency, ensuring that almost every simulated muon contributes to the final calibration sample, thus saving processing time, file size, and storage. Additionally, the simulated muon distributions are inherently consistent with the distributions from data. Given that the calibration chain itself is a time and computing intensive process, the reduction in simulation files and their sizes has significant benefits downstream of the file generation. On the other hand, using real data to seed the simulation could introduce undesirable bias, if we do not carefully consider possible misreconstruction or selection bias.**COMMENT: Can I re-word the last sentence?**

### 2.2.1 Reconstruction and Selection of Cosmic Data Events

It is important to choose a data sample that represents the detector in an ideal state, with as few known issues as possible. For Test Beam, we chose the period 4 data sample (see Tab. 2.1), as the other periods had complications such as faulty [FEBs](#), or underfilled cells. We only used half of the entire period 4 sample by only using every other sub-run for the simulation to only produce the necessary number of events for a successful calibration.

We designed the reconstruction and selection criteria so that the majority of the simulated cosmic muons make it into the final simulation calibration sample. Therefore, we employed a similar process to that used to create the data calibration samples. Additionally, we require all distributions of the selected events to be well-understood and to resemble those of the data calibration samples.

#### Remove Beam Spills

The first step is to remove beam spill events based on their time relative to the time of the beam spill. For Test Beam the beam spill is 4.2 s long and we remove all events within a 5 s window from the start of the beam spill, as shown in Fig. 2.3. This should leave us with mostly cosmic events.

#### Reconstruction

To use the events in the simulation, we require their vertex positions and their initial 4-momenta. We use the standard reconstruction methods from [NOvA](#), described in Sec. 1.5. First we take the raw hits and group them into slices. Then we reconstruct cosmic tracks using the window cosmic track algorithm (used for calibration samples). Since we also require the 4-momentum information we have to use the [BPF](#) tracking algorithm to identify muons and assign their momenta. [BPF](#) required a vertex and prong input information, which we get from a cosmic ray vertex and FuzzyK prong algorithms respectively. The first three steps are identical to the full reconstruction applied to get the calibration samples. Since we do not need a 4-momentum information for calibration, we do not need to use cosmic ray vertex, FuzzyK vertex, or the [BPF](#) to create calibration samples.

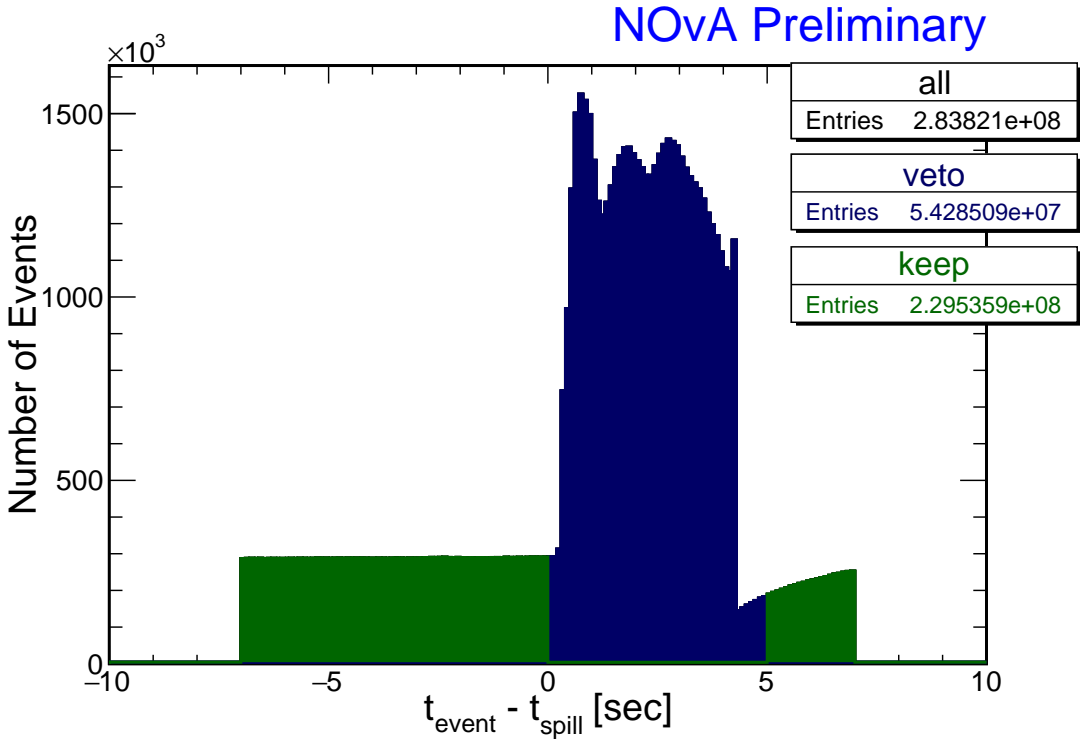


Figure 2.3: Test Beam beam spill events removed (blue) from the calibration samples. The remaining events (green) should mostly consist of cosmic particles. This example and the numbers of entries are for the full period 4 Test Beam sample.

## Selection

After the reconstruction process, we proceed to select events based on their slice' and **BPF** track's properties. The overview of all selection criteria and their corresponding cut values are listed on Tab. 2.2. In detail, the following conditions are used to select cosmic muon events for the data-based simulation:

1. We only use successfully reconstructed 3D **BPF** tracks with the muon assumption;
2. As we aim to select cosmic events originating outside the detector, we apply a cut based on the distance of each track's start position from the edges of the detector. This cut has a negligible impact on the **BPF** tracks, as indicated by the minimal difference between the red and the dotted azure lines in Fig. 2.4;
3. We remove all events whose track is parallel to the beam direction, by requiring the angle from the Z (beam) axis to be  $|\cos_Z| \leq 0.98$ . Figure 2.4 demonstrates the presence of events peaked at track lengths of approximately 410 cm and

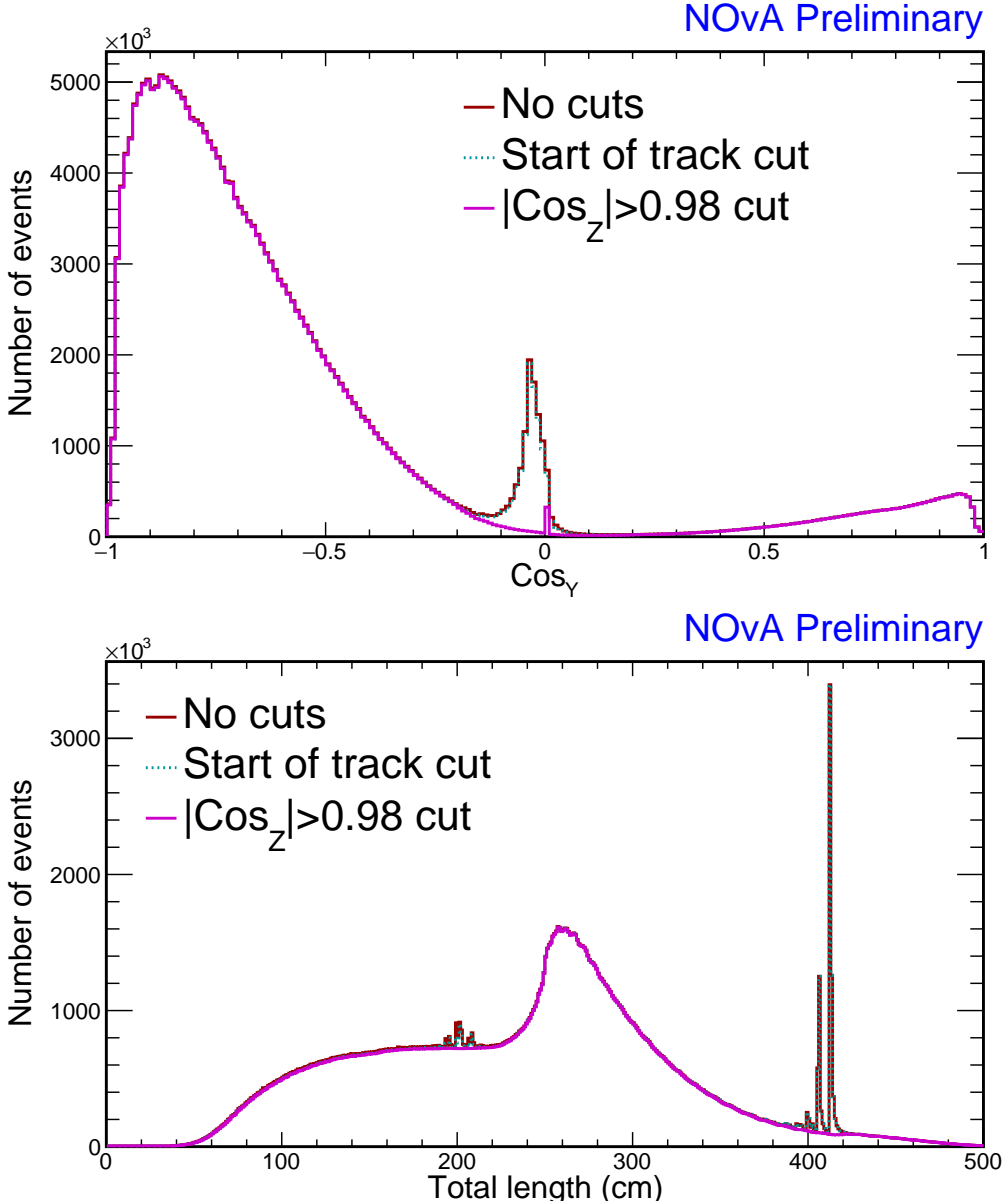


Figure 2.4: Impact of track start and maximum track angle from the z axis ( $\text{Cos}_Z$ ) cuts on the Test Beam data for the data-based simulation of cosmic muons. The track start cut has only negligible effect. The maximum  $\text{Cos}_Z$  cut effectively removes sharp peaks in the total track length distribution and events perpendicular to the Y axis. These events are all parallel with the Z axis and are most likely leftover beam events. All of the distributions are made from the period 4 Test Beam data.

200 cm, which correspond to the total and half length of the detector, respectively (or alternatively lengths of both modules and a single module). These events are strictly parallel to the beam direction and are likely remnants of beam events. Applying a cut on  $\text{Cos}_Z$  effectively removes these events without affecting the rest of the data. This cut might only be needed for the Test Beam detector and not for the near and far detectors.

4. To ensure that only events contributing to the final calibration sample are simulated, we use a selection based on the cuts used to select events for the data calibration samples (see Sec. 1.6). We call these cuts the **calibration cuts**. However, there are two caveats we need to consider when applying the calibration cuts:
  - (a) First, to create calibration samples, we apply the selection on tracks from the **Window cosmic track** algorithm instead of the **BPF** algorithm, which yield different distributions as depicted in Fig. 2.5. Notably, the **BPF** tracks have a hard cut-off at the detector edges, whereas the Window cosmic tracks are allowed to start beyond these limits. Also, the **BPF** tracks have a rugged distribution in  $\text{Cos}_Z$ , which is not present for Window cosmic tracks. This is likely caused by the detector structure, as shown in Fig. 2.6, but it is not clear how. We concluded that the rugged shape does not have any impact on the resulting simulation. Given these differences between the tracking algorithms, applying the calibration cuts on **BPF** tracks could mistakenly remove events that would pass the same selection when applied to the Window cosmic tracks.
  - (b) Second, each reconstruction algorithm has intrinsic deficiencies that can lead to misreconstructions. Applying the full calibration cuts may remove misreconstructed events that should have been included in the simulation, introducing a bias.

To address these concerns, we loosened the full calibration cuts to create a "buffer" around the selected events, allowing for fluctuations of the reconstruction algorithms while maintaining track quality. This way, events that would have been removed based on the calibration cuts applied to their reconstructed **BPF** tracks, but kept based on the calibration cuts applied to their Window cosmic tracks, now have a chance to make it into the final selection and therefore calibration sample. The differences between the full calibration cuts and the employed loosened calibration cuts applied to the **BPF** tracks are listed in Tab. 2.2 and shown in Fig. 2.5. There we also show the data calibration sample, which was created by applying the full calibration cuts on window cosmic tracks from

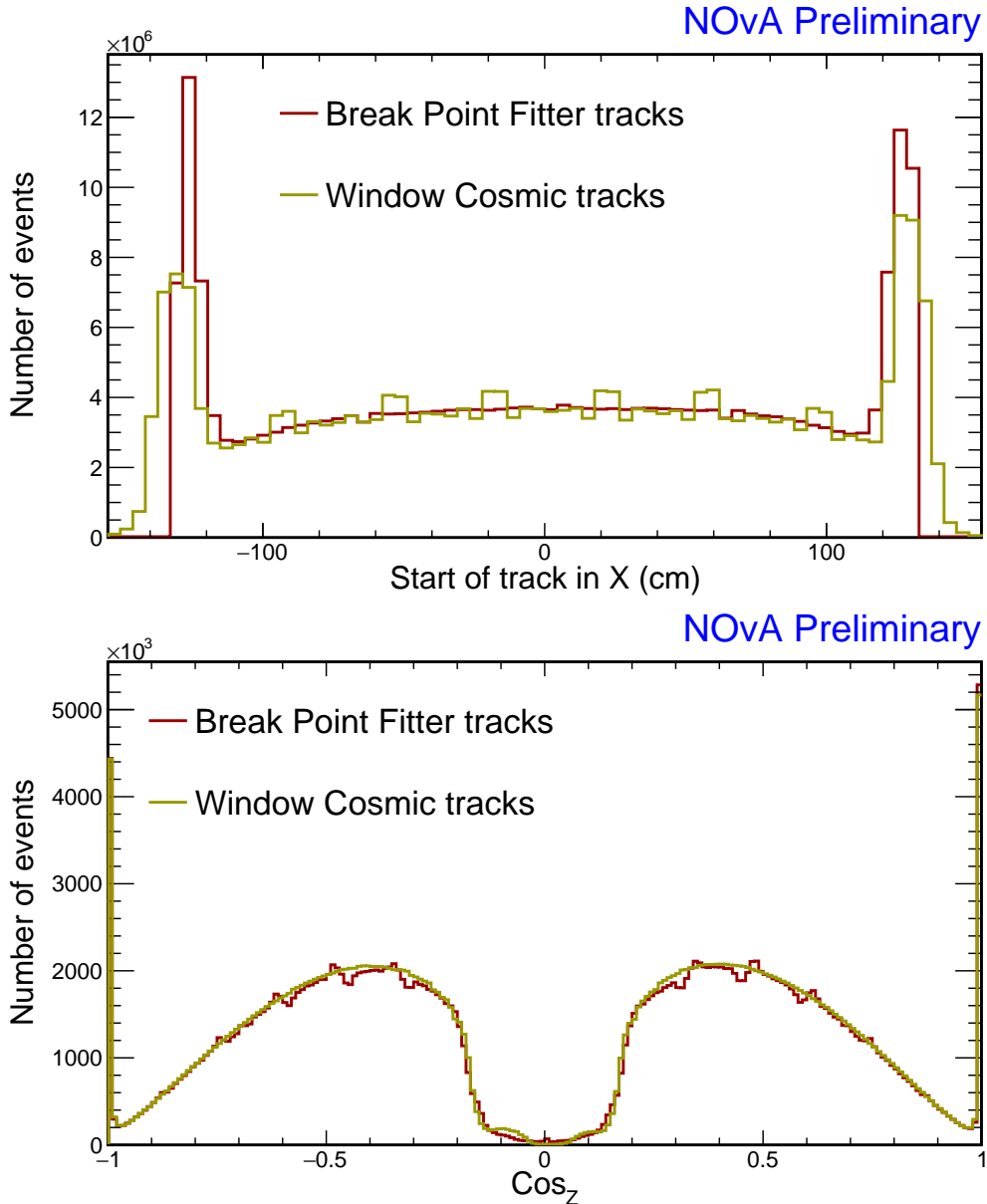


Figure 2.5: Difference between the tracks reconstructed with the BPF and with the Window cosmic track algorithms. Both distributions are for the period 4 Test Beam data (with removed beam spill) without applying any selection.

the same artdaq data sample.

During the selection process, we determine whether the muon is stopping inside the detector or passing through, based on the reconstructed track's end position. For Test Beam we say it is a stopping muon if its track ends at least 20 cm from any edge of the detector. For the far and near detector this is 50 cm. This information assists in correcting the energy of through-going muons, as outlined in the following Sec. 2.2.2.

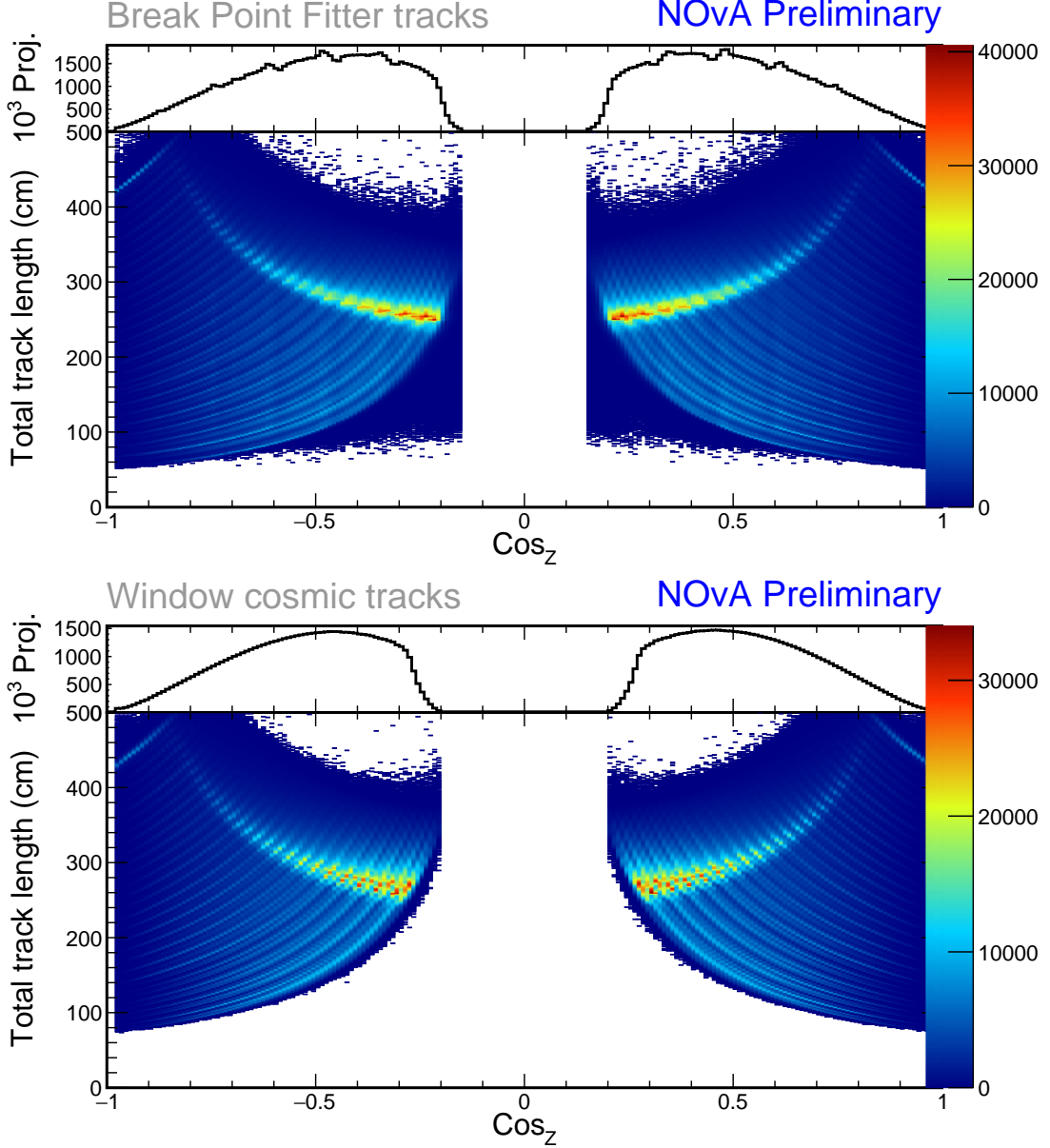


Figure 2.6: Investigating the origin of the rugged shape in the  $\text{Cos}_Z$  distribution of **BPF** tracks. The top plot is created with the Loose calibration cuts and the bottom plot with the Full calibration cuts, as described on Tab. 2.2. However, this difference in selection shouldn't matter. The long lines on the 2D plots are likely the effects of the detector structure. We can see that for the **BPF** tracks, each  $\text{Cos}_Z$  angle corresponds to a specific track length, whereas for the Window cosmic tracks there is multiple track length for each angle. This could cause the resulting shape in the  $\text{Cos}_Z$  distribution of **BPF** tracks.

## 2.2.2 Energy Correction, Charge Assignment and Smearing

Once we have the kinematic information for the selected events, we perform several tasks to get the final sample of cosmic muon events for the data-based simulation. This includes correcting energies of the through-going muons, assigning a charge

Table 2.2: Event selection of cosmic muons used for the data-based simulation (in green under Loose selection) and comparison to the Full selection cuts used to create the calibration samples in blue. The last two rows are not used for Test Beam, but are employed for the Near and Far detectors and should be examined before creating another data-based simulation for them.

Cut	Selection	
	Full	Loose
Muon assumption and 3D track from BPF		
Max. track start distance from edge	50 cm	
Max. $Cos_Z$	0.98	
Calibration sample selection	Max. number of hits in X or Y	2
	Min. difference between $Stop_Z$ and $Start_Z$	70 cm
	Min. $Cos_Z$	0.2
	Min. frac. of slice hits in track in each view	0.8
	Max. number of cells per plane in each view	6
	Max. difference in X-Y for first (last) plane	3
	Max. plane asymmetry	0.1
	Max. step size to median step size ratio	3
	Max. vertex distance from edge	10 cm
	Max. track end distance from edge	10 cm

to each muon event, and smearing and converting the information into the correct format required by the generator.

### Energy Correction

Through-going muons do not deposit all of their energy inside the detector. From the reconstructed information we cannot reliably calculate their initial energies, but we can estimate an energy that could leave the same track. In general, the energy spectrum of cosmic muons can be approximately described by a power law  $E^{-\alpha}$ , with  $\alpha \approx 2.7$  [91, 92]. The expectation value for the "true" initial energy of through-going muons can be therefore calculated as

$$\langle E \rangle = \frac{\int_{E_R}^{E_C} E \cdot E^{-\alpha}}{\int_{E_R}^{E_C} E^{-\alpha}} = \left( \frac{\alpha - 1}{\alpha - 2} \right) \left( \frac{E_C^{2-\alpha} - E_R^{2-\alpha}}{E_C^{1-\alpha} - E_R^{1-\alpha}} \right), \quad (2.1)$$

where  $E_R$  is the reconstructed energy we got from the BPF.  $E_C$  is the critical energy chosen to be 300 GeV, as we do not expect muons with higher energies to be selected due to large showers along their paths.

We use this corrected initial energy for all muons that do not stop inside the detector, as identified during selection described in Sec. 2.2.1. Figure 2.8 shows the cor-

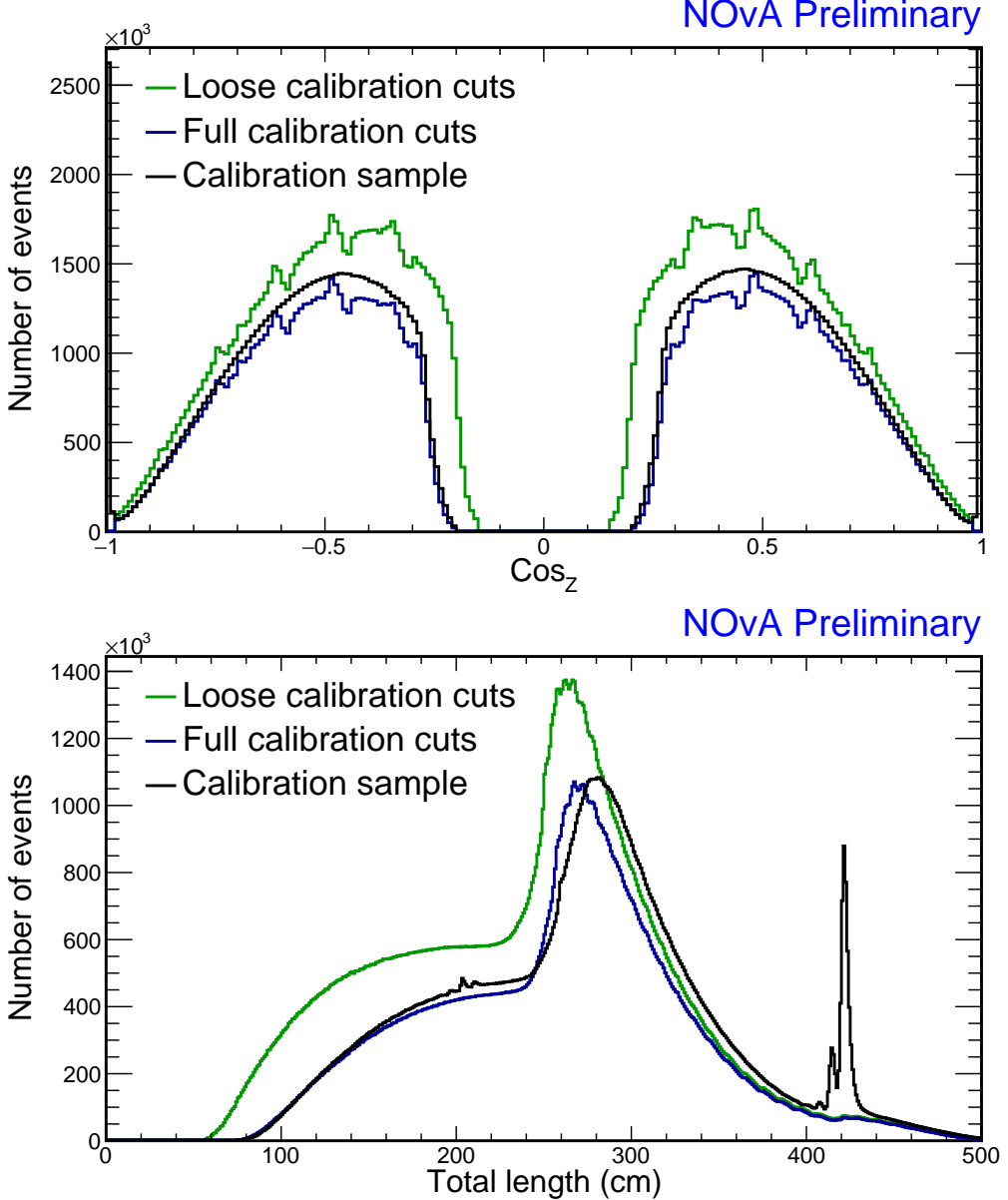


Figure 2.7: Comparison of event selections for the data-based simulation and of the corresponding data calibration sample in black. The green line represents the final selection used for the simulation, using the loosened calibration cuts, as described in text and in Tab. 2.2. The blue line shows the distributions with full calibration cuts applied to the same sample and using the same tracks. The "calibration sample" shown in black was made with the same full calibration cuts as the blue line (without the track start cut and maximum  $\text{Cos}_Z$  cuts), but applied to the window cosmic tracks instead of the BPF tracks. All of the distributions are made from the period 4 Test Beam data.

rected energy distribution of our selected events and demonstrates that the choice of the critical energy does not significantly change the correction.

This corrected energy is **not** a good representation of the true energy spectrum of cosmic muons on surface level and getting a correct energy distribution from data

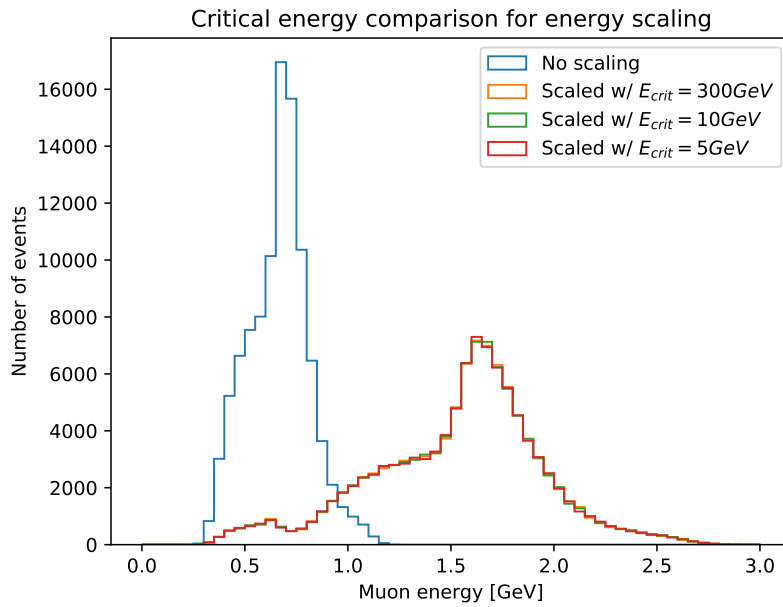


Figure 2.8: The effect of energy correction for through-going muons with various critical energies. No significant difference can be seen when using different critical energies.

would require a much more dedicated effort. The corrected energy would also be different for different [NOvA](#) detectors, since the reconstructed energy is calculated from the track length. For example, the corrected energy of cosmic muons when entering the detector would be larger for the bigger [ND](#) than for Test Beam, even though the [ND](#) is underground.

However, since this simulation is intended to be used for calibration, where we use through-going muons only for relative calibration, we do not need a perfect representation of the cosmic muon energy spectrum. Not including more energetic cosmic muons into the simulation does bias the energy deposition towards lower values, but this is corrected for during absolute calibration which only uses stopping muons, for which we assume we reconstruct their energy well from [BPF](#).

If someone were to use this simulation for something other than calibration, it would be necessary to rethink the energy correction, either by changing the energy estimation from track based algorithms to energy deposition, or by including information from external sources. It would also be necessary to include angular dependence for the energy correction as described in the PDG [92].

## Smearing

The reconstructed data is influenced by the detector structure, reconstruction efficiencies and other effects that can bias the simulation. To avoid this influence, we smear the reconstructed values by randomly changing

- the total momentum within 2%,
- the azimuthal angle uniformly,
- the polar angle within 4 mrad,
- and the X/Y and Z vertex positions within the width or depth of the cell respectively.

The size of the smearing has been decided as the best estimate of variations of these variables for cosmic muons.

## Charge Assignment

We need to tell the detector simulation whether to simulate a muon or an anti-muon. However we do not reconstruct the charge of the muons, so we have to randomly assign it based on a statistical distribution from external measurements [91]:

$$P_+ \simeq 0.539 + \frac{x}{34.5} - \left( \frac{x}{9.48} \right)^2 + \left( \frac{x}{8.27} \right)^3, \quad (2.2)$$

where  $x$  is the logarithm of the total momentum in GeV.

## Running the Simulation

We save the vertex positions, the four momenta and the assigned charge into a text file, that is then fed into the same detector and readout simulation chain, as was described for the [ND](#) and [FD](#) in Sec. 1.4. We use the fibre brightness map that is used in calibration (see Sec. 1.6) to inform the simulation about the real detector conditions. Since we want the simulated detectors to be functional copies of the ideal versions of the real detectors, it is important to provide a correct brightness file without any defects. For this simulation we use the fibre brightness map described in Sec. 2.3.1.

### 2.2.3 Validation

To validate whether the newly created simulation works as expected, we compare the new simulation with the original data it was created from. Additionally, we use the new simulation as "fake data" and pass the simulated events through the same reconstruction, selection and simulation processes as were used to create the first simulation, creating a "re-simulation" sample. This is used to validate the stability of the simulation process.

For the data-simulation comparisons we use the events from the actual calibration samples as data. This is equivalent to looking at the Window cosmic tracks with full calibration cuts described in the selection Sec. 2.2.1. We are expecting the new simulation to be similar to the data calibration sample, without a bias from the original data used for the simulation.

Figures 2.9 and 2.10 show that the angular distributions of the new simulation (pink lines) are almost the same as the distributions of the **BPF** tracks with full calibration cuts (blue dashed lines). This means that loosening up the calibration cuts (green dashed lines) did not help as expected with compensating for the underlying differences between the **BPF** tracks and the Window cosmic tracks. This can also be seen on the total track length distribution in Fig. 2.10. During the development of the event selection we created three more versions of the simulation with various event selections, including with full calibration cuts and with different loosened calibration cut values. It became clear that it is unlikely we could mitigate these track algorithm differences by changing the selection even more. Since the entire simulation process is fairly time and resource consuming and the distributions of the new simulation look reasonable and are close enough to the data, we've decided to proceed with this version of the simulation and use it in the Test Beam calibration.

The start of track comparison between data and simulation in Fig. 2.11 and 2.12 show that there are fewer events that start at the edge of the detector and the vertex positions are moved slightly towards the inside of the detector. This is likely the result of the smearing of the vertex positions and we do not expect this to have an effect on the calibration. **COMMENT:** *Should this have been mitigated? Should I mention here that the smearing is still a good idea?*

After adding the distributions for the re-simulation calibration sample, shown in

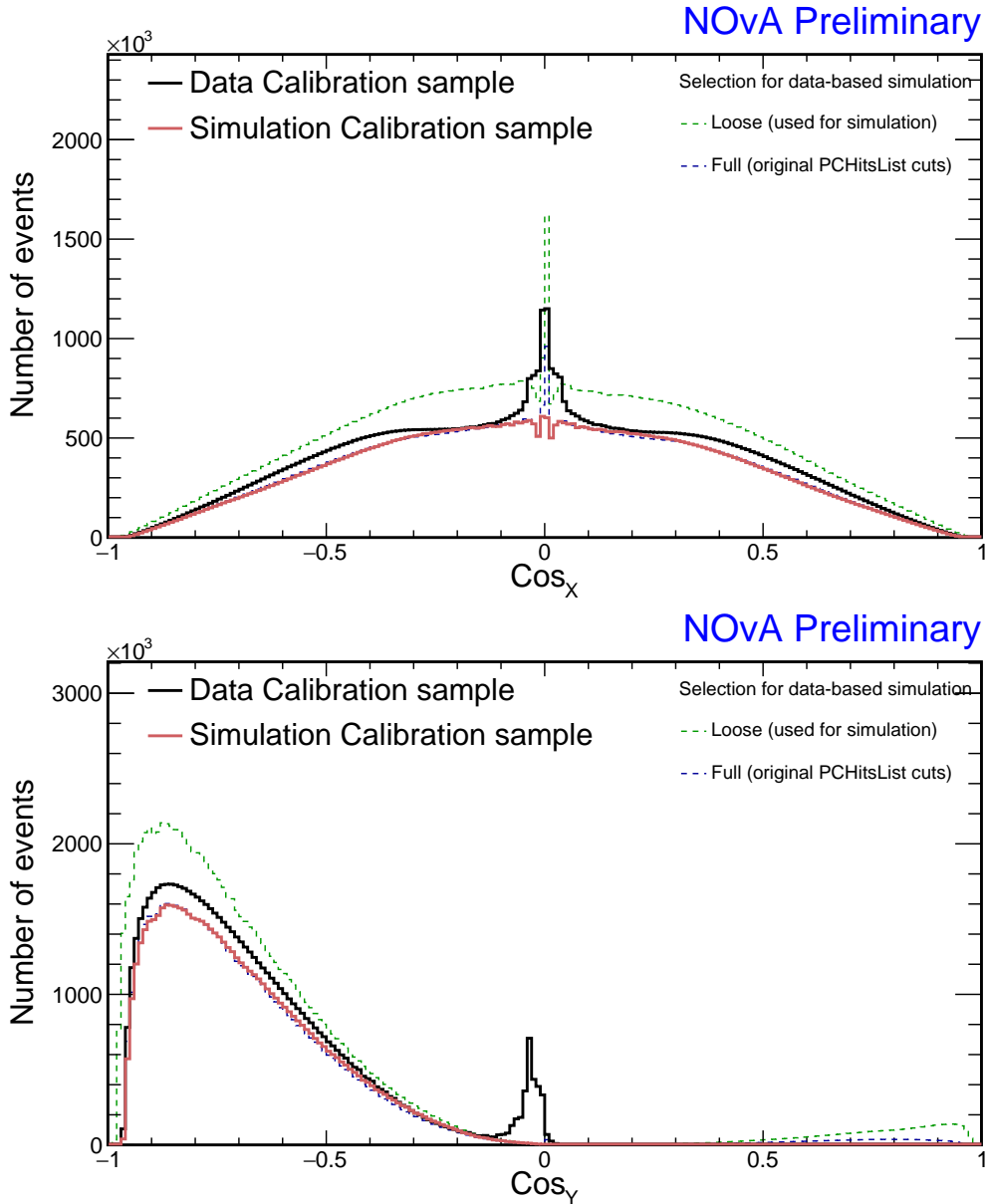


Figure 2.9: Angular distribution comparison of the newly created simulation calibration sample and the corresponding data calibration sample. We are also showing the selection of data used to create the new simulation in green and a "full calibration cuts" selection (same cuts as used for the simulation calibration sample but applied to BPF tracks instead of Window cosmic tracks) in blue.

Fig. 2.13, we can see that the tracks' starts are shifted even further towards the inside of the detector. This would support the hypothesis that this effect is caused by the smearing of the reconstructed variables. This is also likely directly related to the loss of events with longer track lengths as shown in Fig. 2.13. If tracks start a few centimetres later in the detector their tracks would get shorter by the same amount.

**COMMENT:** Should I describe every single aspect of the validation plots in here? For

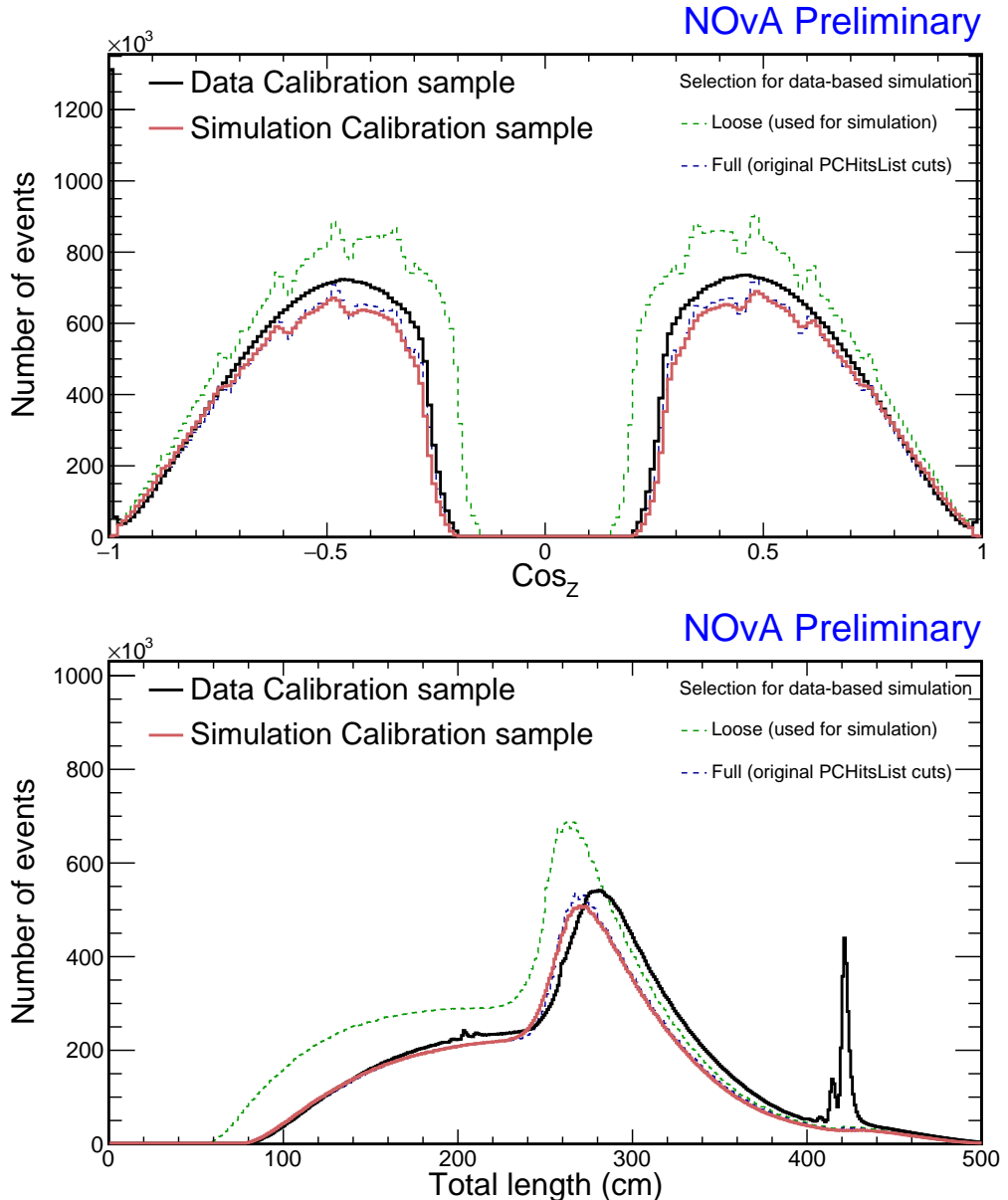


Figure 2.10: Angular and total track length distribution comparison of the newly created simulation calibration sample and the corresponding data calibration sample. We are also showing the selection of data used to create the new simulation in green and a "full calibration cuts" selection (same cuts as used for the simulation calibration sample but applied to BPF tracks instead of Window cosmic tracks) in blue.

*example the black peaks in Fig. 2.9 and 2.10? These have been explained during selection (leftover beam events) but might be good to explain them here as well and reference the selection*

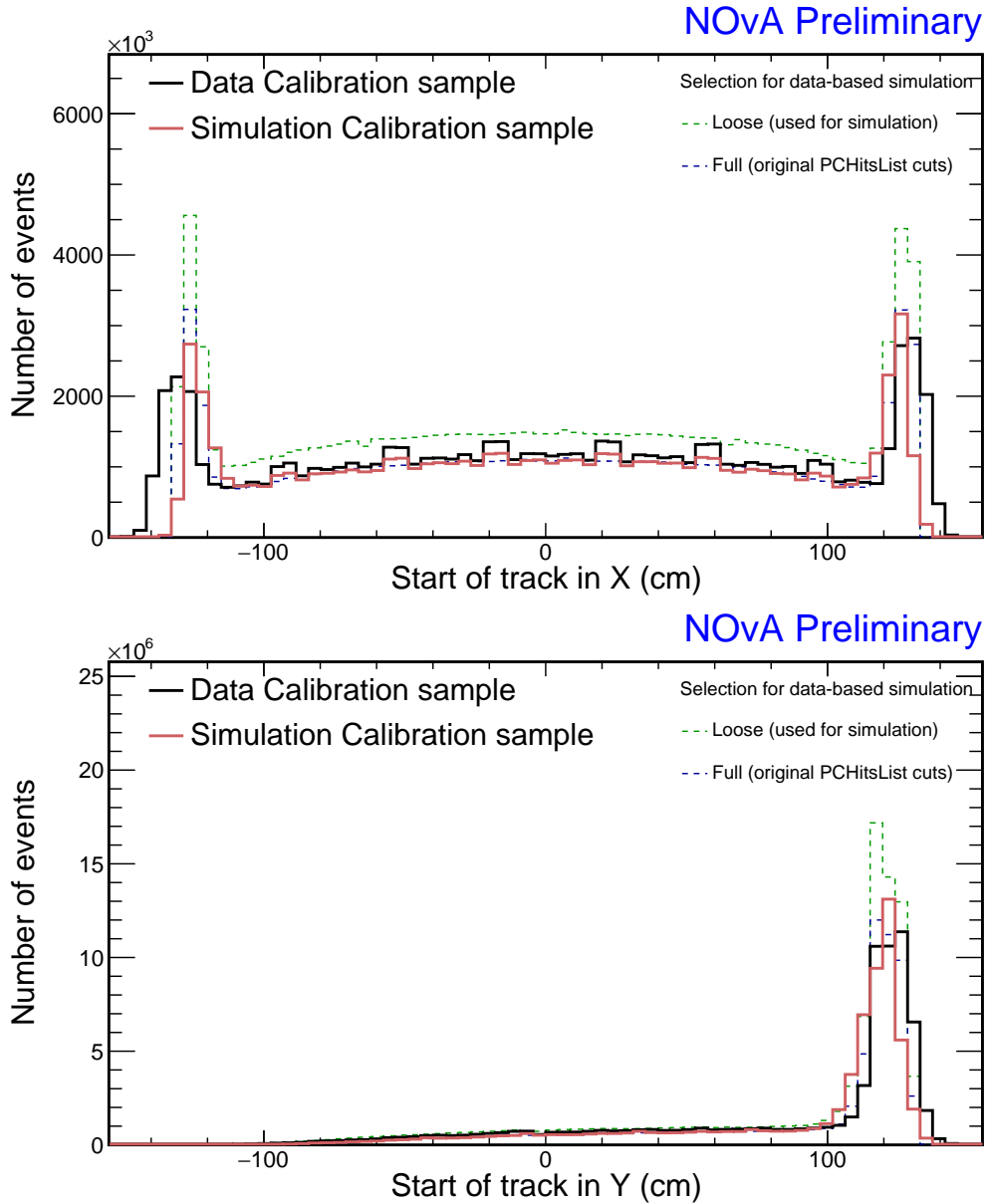


Figure 2.11: Start of tracks comparison of the newly created simulation calibration sample and the corresponding (period 4) data calibration sample. We are also showing the selection of data used to create the new simulation in green and a “full calibration cuts” selection (same cuts as used for the simulation calibration sample but applied to BPF tracks instead of Window cosmic tracks) in blue.

## 2.3 NOvA Test Beam Detector Calibration

In this section we describe the details of the Test Beam detector calibration as it was finalized in June 2023. This version includes a new purpose-made simulation and all the measured Test Beam data, with the exception of the period 1 data.

The data calibration samples for Test Beam were creating using the same procedures as the [ND](#) and [FD](#) calibration samples, described in Sec. 1.6. However, there are

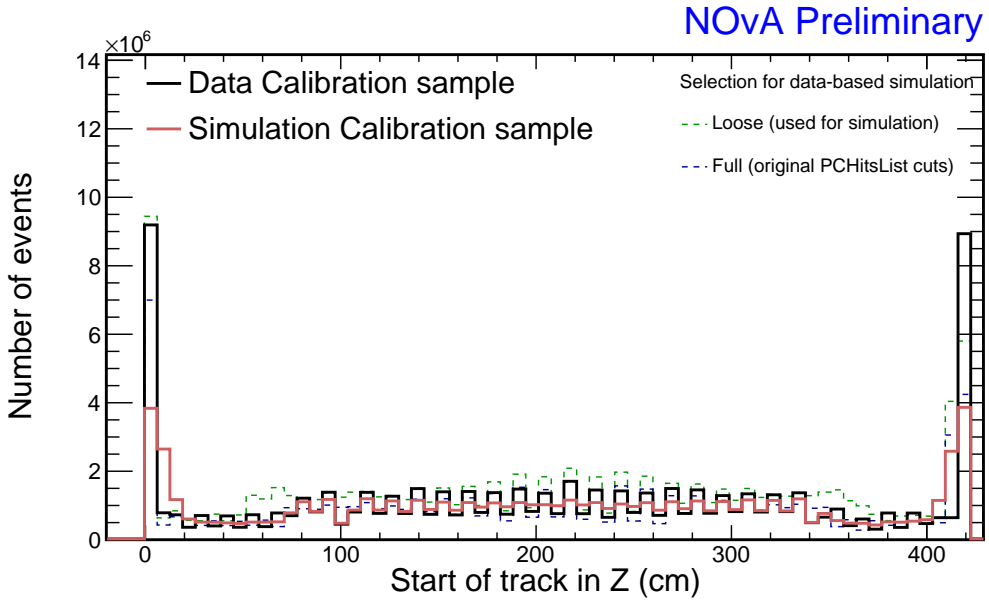


Figure 2.12: Start of tracks comparison of the newly created simulation calibration sample and the corresponding (period 4) data calibration sample. We are also showing the selection of data used to create the new simulation in green and a "full calibration cuts" selection (same cuts as used for the simulation calibration sample but applied to BPF tracks instead of Window cosmic tracks) in blue.

two cuts from the event election, that were by accident not included for Test Beam during the processing of the data samples. This can be seen on Tab. 2.2, where the two bottom rows show the two excluded cuts. One cut contains the vertex close to the edge of the detector ensuring we only use cosmic events, the other contains the end of track close to the edge, ensuring we only use through-going muons for the relative calibration. Given that we remove beam events and that all the other cuts are designed to select cosmic events, the first cut has only a negligible effect on the final selection. Additionally, the stopping muons only make up a small fraction of the total cosmic muon events, rendering the second cut also with only limited effect. Therefore, we concluded that the lack of the two event selection cuts for the Test Beam calibration samples does not have a substantial impact on the result and does not necessitate re-processing of the calibration samples, which would cost time and resources.

This section is organized as follows. We first describe the Test Beam versions of the fibre brightness map and the threshold and shielding correction introduced in Sec. 1.6. We then go over the simulation and the three data samples and for each one we introduce their respective detector conditions and how they may affect the energy

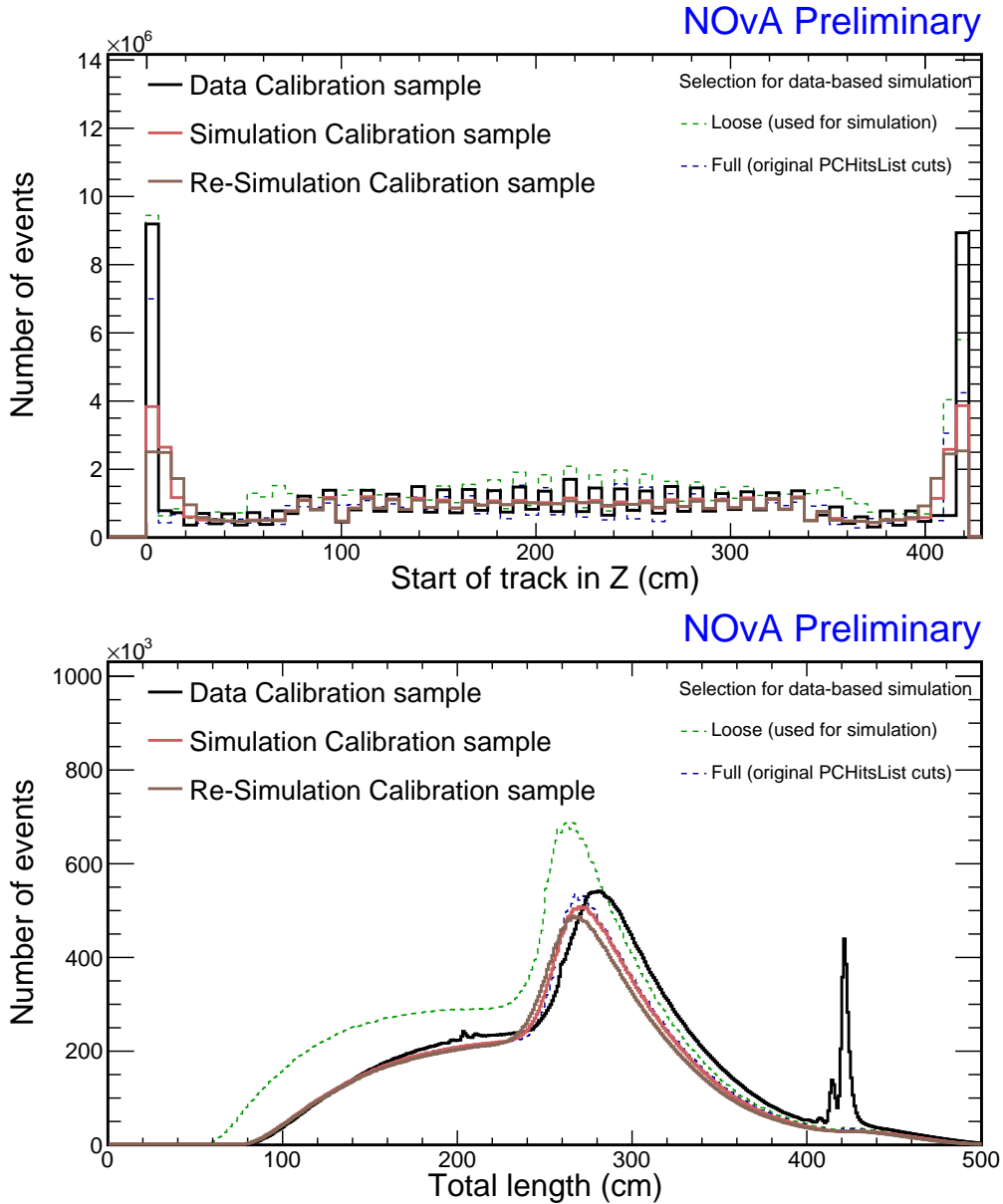


Figure 2.13: Distribution of the re-simulated events, when the new simulation is used as “fake data” for a new iteration of the simulation process discussed in this document. This is compared to the newly created simulation calibration sample and the corresponding data calibration sample. We are also showing the selection of data used to create the new simulation in green and a “full calibration cuts” selection (same cuts as used for the simulation calibration sample but applied to BPF tracks instead of Window cosmic tracks) in blue.

deposition. We show the state before the calibration process and discuss the effects that should be corrected for during calibration. We then show a selection of attenuation fit results and an overview of the relative calibration effects. Afterwards, we discuss the absolute calibration for all the samples combined, as well as the validation and conclusion of the Test Beam calibration.

### 2.3.1 Fibre Brightness

To divide the Test Beam detector into fibre brightness bins we used the attenuation fit results for period 4 Test Beam data (described in Sec. 2.3.6), as that is the best detector conditions data we have. Since we need the fibre brightness map in order to run the attenuation fits and we need the attenuation fit results to create the brightness file, we proceeded iteratively and first ran the attenuation fit with an older version of the brightness file and then used the newer fit results to create a new brightness file to be used in a new attenuation fit.

As we are only using the attenuation fit results in the centre of each cell to create the fibre brightness map, we've decided to allow some cells that initially failed the calibration condition ( $\chi^2 > 0.2$ ), to be still used for the creation of the brightness file. Otherwise, all the officially uncalibrated cells would be assigned an average response and we would lose the information on their relative brightness. As can be seen in Fig. 2.14, some attenuation fits have  $\chi^2 > 0.2$ , even though they correctly represent the energy deposition in the centre of that cell. By carefully investigating all Test Beam cells with  $\chi^2 > 0.2$  (which is doable for Test Beam, due to its small number of cells), we concluded it is safe to use all the attenuation fit results with  $\chi^2 < 0.7$ . We use this loosened calibration condition only to create the fibre brightness file and we keep the original condition for the actual calibration results.

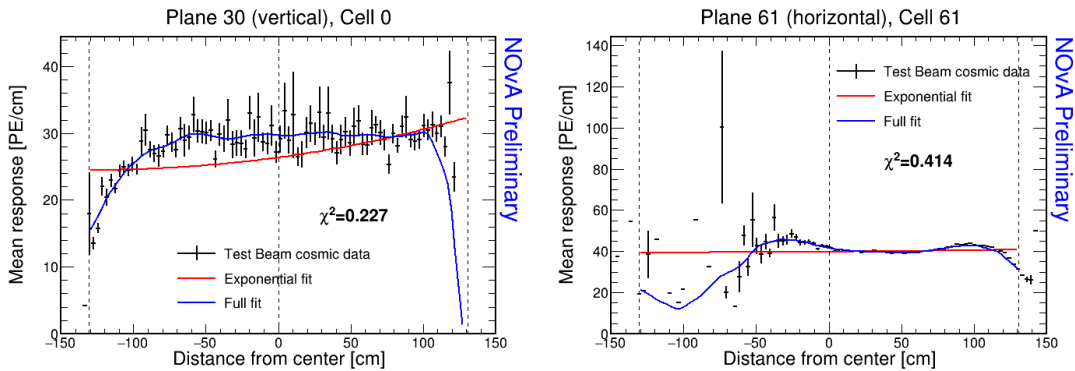


Figure 2.14: Examples of attenuation fits for two cells that fail the calibration condition, but the fit (blue line) still correctly represents the energy deposition in the centre of that cell (dashed vertical line in the middle).

The final distribution of fibre brightness bins and their corresponding relative brightnesses for the Test Beam detector is shown in Fig. 1.10.

### 2.3.2 Threshold and Shielding Corrections

We created the threshold and shielding correction for Test Beam from the new simulation described in Sec. 2.2. As can be seen in Fig. 2.15, the correction is almost uniform as a function of both the position within each cell and the cell number. This is the case for all the Test Beam fibre brightness bins and for both views.

The uniformity of the distributions is expected, as the Test Beam detector is much smaller than the FD, results of which originated the study of the threshold and the shielding effects. The cell length of 2.6 m has only a negligible impact on the energy distribution of cosmic muons or on the threshold saturation. Therefore the threshold and shielding correction for Test Beam is only a normalization factor, except for the cell edges, where there is a large variation in the energy response there anyway due to low number of events. Since we apply the correction prior to the relative calibration, which only cares about the relative differences across the detector, a correction consisting of only a shape-less normalization factor does not have any impact on the calibration results.

### 2.3.3 Simulation

We use the data-based simulation described in Sec. 2.2. Figure 2.16 shows the distribution of the tricell hits from the simulated cosmic muon events selected for calibration. The features on this plot illustrate the distribution of tricell hits in the Test Beam detector in ideal conditions and are present in all the data samples as well. We can clearly see the difference between the number of events in the vertical (even) and the horizontal (odd) planes. This is expected as cosmic muons are generally vertical and a single cosmic track often passes more horizontal planes than vertical planes. We can also see that due to the tricell condition there are no hits in cells 0 and 63, which are on the edge of the detector. The clear horizontal lines are made up by cells (0), 15, 16, 31, 32, 47, 48, (63), or in other words by the first and last cell of each 16 cell-wide extrusion that makes up half of a module (which makes up half of the Test Beam plane). As was mentioned in Sec. 1.2, these cells are 3 mm narrower than the rest, which results in fewer hits and lower deposited energy, but consistent deposited energy per path length. Overall, Fig. 2.16 shows that the tricell hits are distributed fairly uniformly in the centre of the detector, with the number of hits dropping off

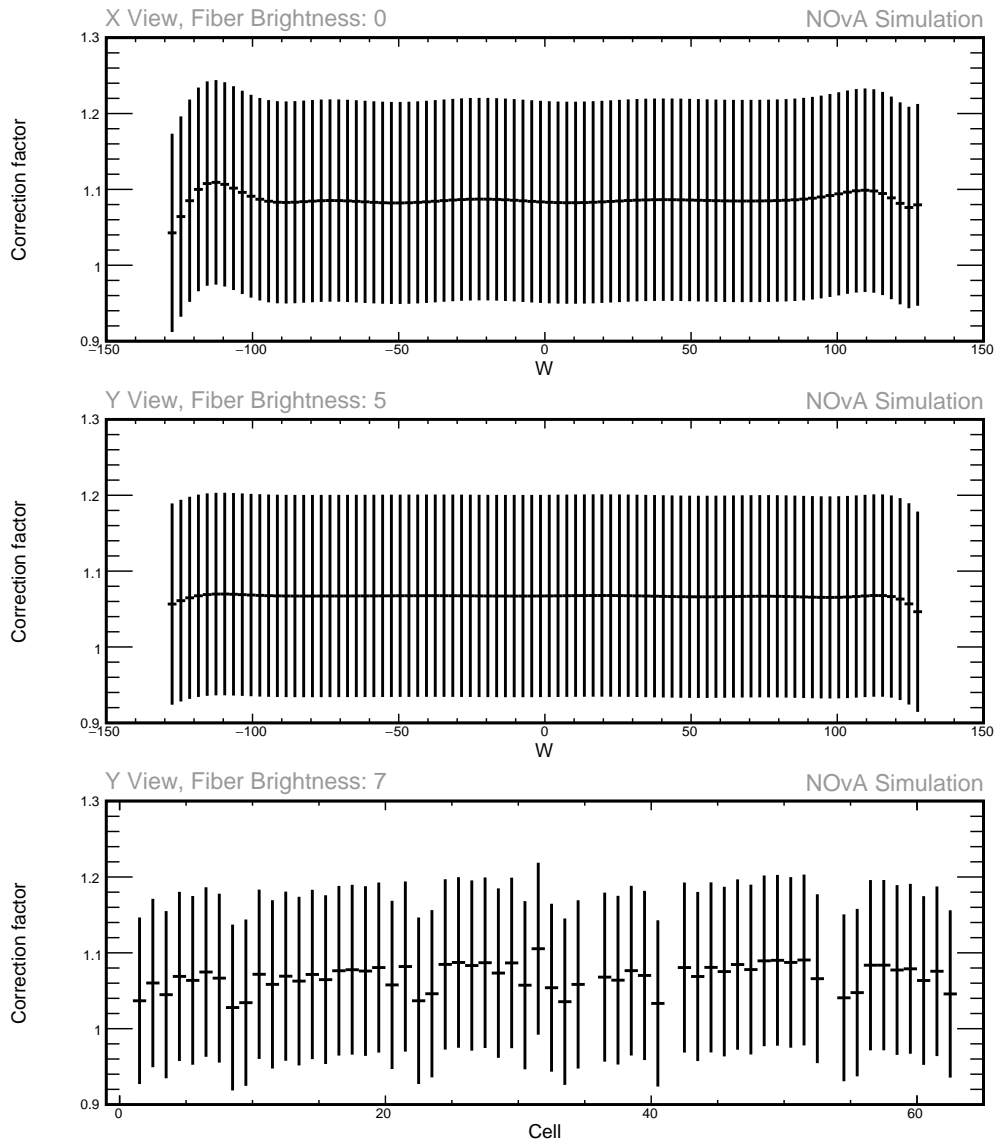


Figure 2.15: Examples of threshold and shielding corrections for the Test Beam detector.

towards the front, back and corners of the detector. This is due to the event selection applied to the cosmic tracks to be used in calibration.

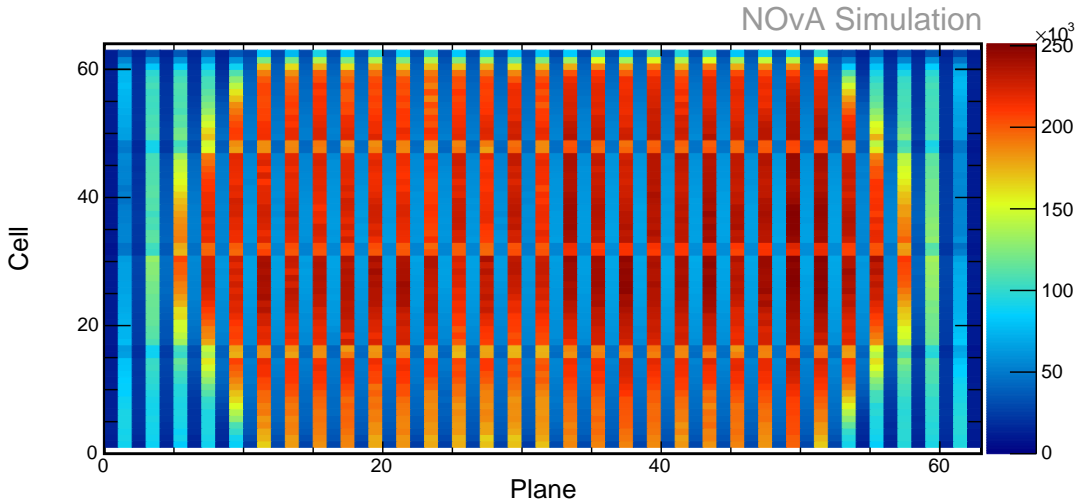


Figure 2.16: Distribution of hits used in the calibration for events in the Test Beam simulation calibration sample.

The distributions of deposited energy before calibration in units of PE/cm are shown in Fig. 2.17. We are showing the dependence on the positions within a cell  $w$ , Cell number and Plane number. These are the distributions that are supposed to be uniform after applying the results of the calibration. We can identify the main features that will need to be corrected for during calibration.

The rise of the energy response along  $w$  shown in Fig. 2.17 is caused by the attenuation of light along the **WLS** fibres. The drop of the response at the edges of the cell is caused by the fibres looping and connecting to the **APD** and the larger uncertainties at the edges of the cell are caused by lower number of hits passing the event selection and the tricell condition.

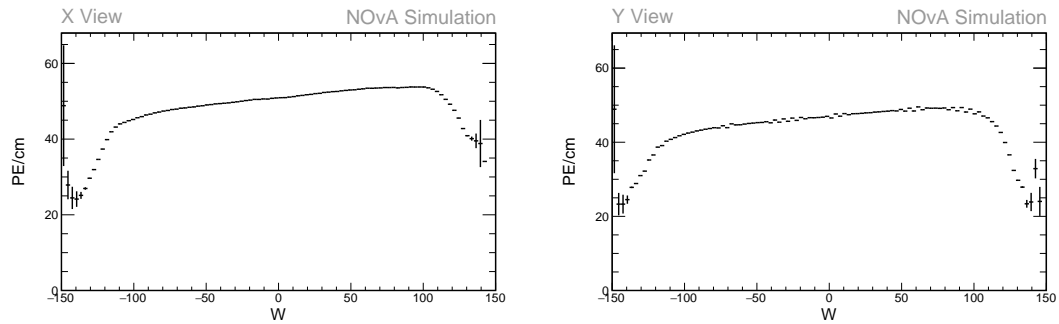


Figure 2.17: Uncorrected average energy response along the position within a cell ( $w$ ) for simulation. Left side shows distributions for the X view planes and right side for the Y view planes.

The rise of the response along the cell number shown on the middle plots of Fig. 2.18 is due to the varying distance of the cells to the readout. Since the APDs are located on a side of each module, the light from the cells on the opposite side has to travel along the WLS fibre for the additional width of the module, compared to the cells close to the readout. Light undergoes additional attenuation along these so-called pig tails, causing the difference of the energy response.

We can also see additional drops in the uncorrected energy response for cells 0, 1, 9, 10, 23, 24, 31 and 32 (and the corresponding cells in the second module). These are most likely related to the organization of the WLS fibres' connections to the APDs. As can be seen in Fig. 1.5, the fibres are connected to the total 32 APD pixels in four rows of 8 pixels. Therefore, if one side of each APD has a lower response than the rest, this could explain the drop in the energy response for the aforementioned mentioned cells. However, this has not been confirmed yet and the reason for one side of the APD having a lower response than the rest is unclear. **COMMENT:** *Also I need to make sure that the pixel organization on the APD is the way I explain it here*

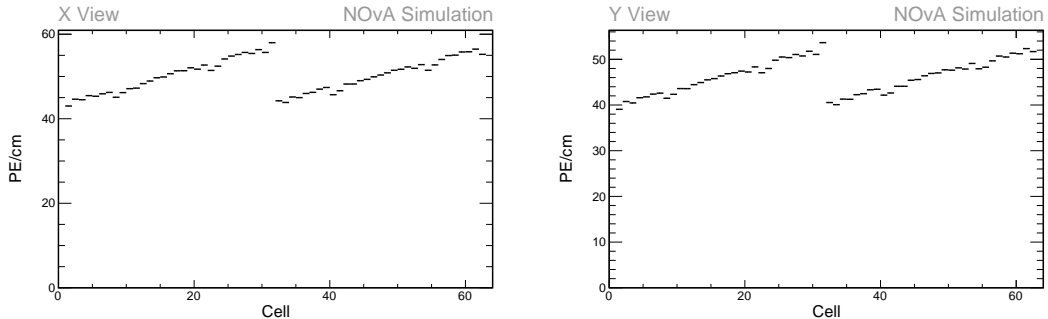


Figure 2.18: Uncorrected average energy response along cells for simulation.

The distribution of the uncorrected response along the planes is shown in Fig. 2.19. Here we can see large fluctuations in both views, but we can clearly identify the three distinctly different responses corresponding to the various scintillators used, as we described in Sec. 2.1. Additionally, planes 16, 17, 48 and 49 have a lower response relative to their neighbouring planes due to the different readout electronics used in these planes.

### Simulation Relative Calibration Results

An overview of the attenuation fit results for simulation are shown in Fig. 2.20 as a map of the average fitted response in the centre of each cell. The blank cells show the

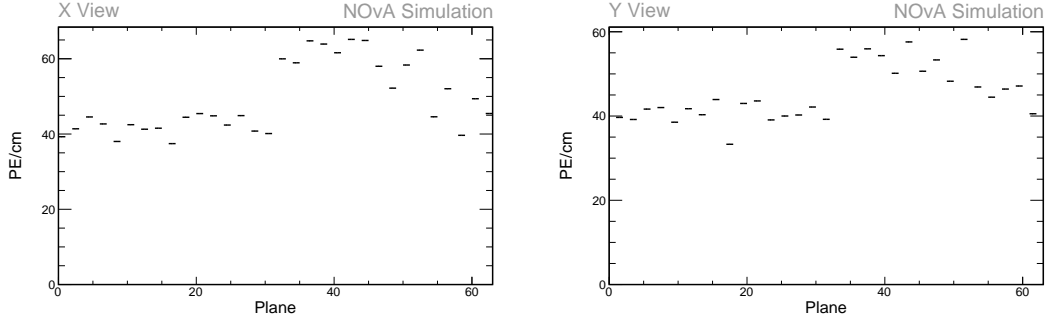


Figure 2.19: Uncorrected average energy response along planes for simulation.

uncalibrated cells which failed the calibration condition (attenuation fit  $\chi^2 > 0.2$ ). Most of the uncalibrated cells are on the edges of the detector, which is expected as those have much fewer events that pass the calibration sample selection than the rest. There are a total of 43 uncalibrated cells out of the total 4032 cells, resulting in 1.07% of the simulated detector uncalibrated.

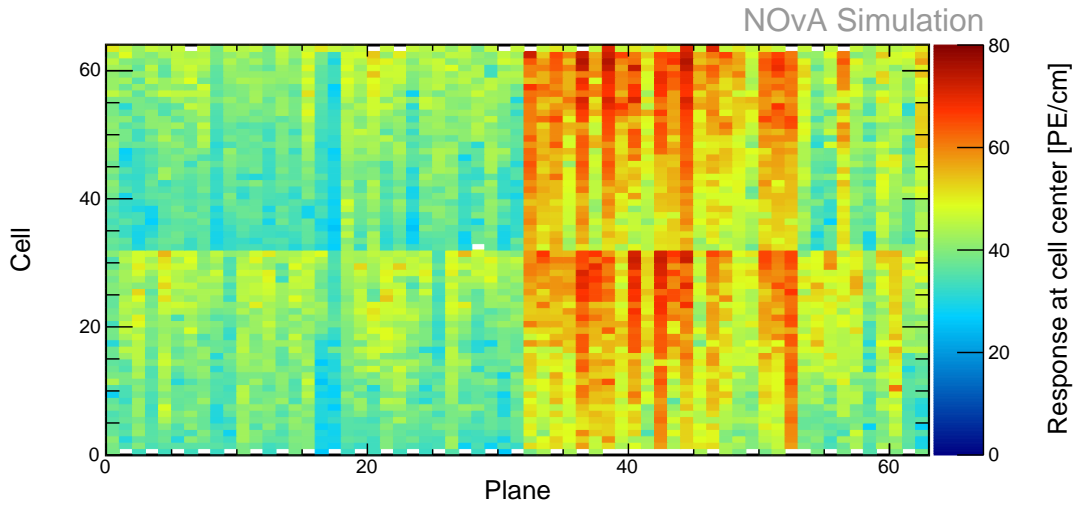


Figure 2.20: Overview of the attenuation fit results for the calibration of the simulated Test Beam detector. Each cell represents the result of the attenuation fit of the energy response in the centre of that cell. The blank cells are uncalibrated as the attenuation fit did not satisfy the calibration condition.

Examples of the standard detector response and of the response for cells on the edge of the detector are shown on the top left plot and on the two bottom plots of Fig. 2.21 respectively. Here the red line shows the initial exponential fit and the blue line the final attenuation fit after the LOWESS correction, as described in Sec. 1.6. The cells on the edge of the detector failed the calibration conditions due to the low number of entries causing large fluctuation in the mean response.

There is only one cell in the middle of the detector that is left uncalibrated. This is

the cell 32 in a vertical plane in the brightness bin 5, shown on the top right of Fig. 2.21, with  $\chi^2 = 0.227$ . It seems the reason this cell has a  $\chi^2 > 0.2$  and therefore failed the calibration condition is the unusually high response with a large uncertainty in the right-most bin. It is unclear why this bin has such an elevated mean response, but since this only causes an issue for a single cell, we decided to ignore it.

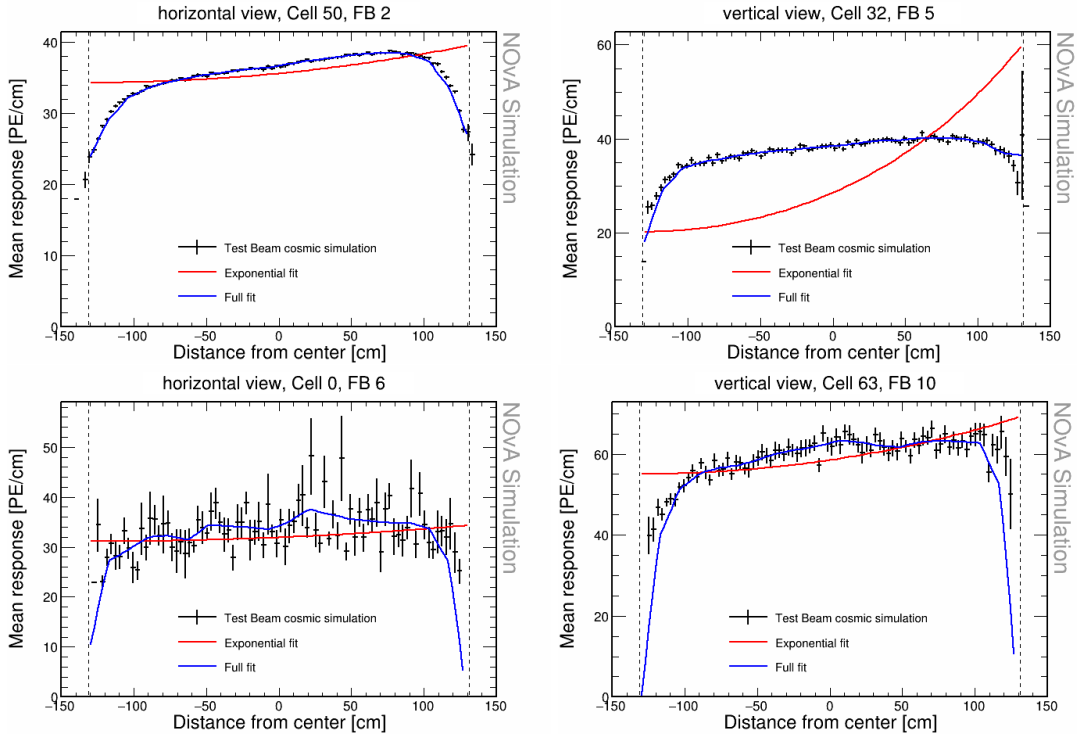


Figure 2.21: Attenuation fits for a selection of cells in the Test Beam calibration simulation. Top left is an example of a successful attenuation fit, top right is a failed fit due to statistical fluctuation in the last bin and the bottom plots show failed fits for cells on the edges of the detector.

### 2.3.4 Period 2 Data

The issue with underfilled cells described in Sec. 2.1 was present throughout the period 2 data taking. This can be clearly seen in Fig. 2.22, represented by the empty cells 31 and 63 in the horizontal planes, which were marked as bad channels and therefore ignored during production of calibration samples. This also affects the neighbouring cells to the underfilled cells, which have fewer events due to the tricell condition (see Sec. 1.6).

We can also see three noticeably darker spots than their neighbours. Specifically in plane 48 cells 38-40 and in plane 55 cells 2-4 and 45-47. These are all three cell wide,

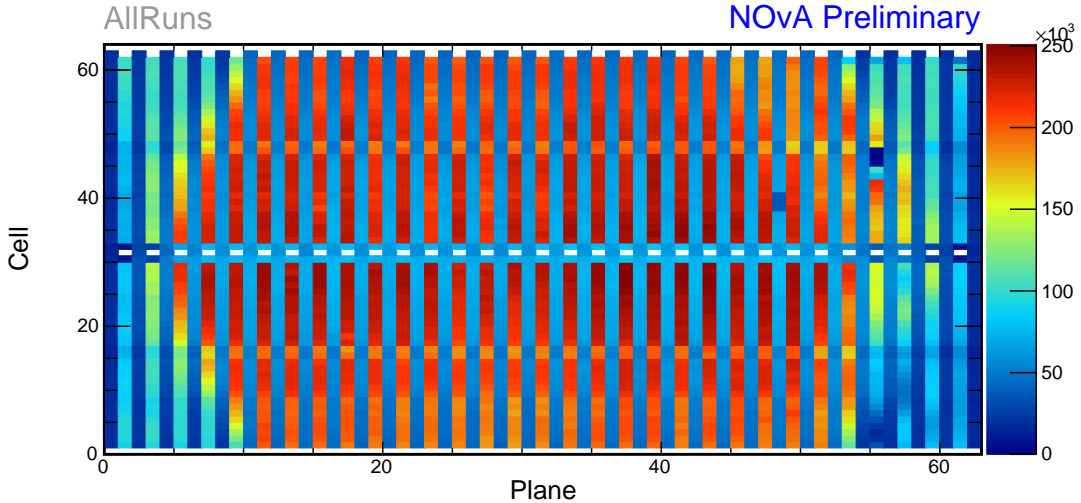


Figure 2.22: Distribution of events in the period 2 Test Beam data calibration sample.

so it is likely that the issue is only in the middle cells and their immediate neighbours are affected due to the tricell condition. The three affected cells had most likely dead channels for some portion of period 2, with cell 46 in plane 55 being dead the longest. One possible explanation proposed for dead channels in plane 55 is that it is due to switched cables from the readout to the DAQ [93], which is manifested as fewer total number of events in those cells. However, this wouldn't explain the dead channel in cell 39 of plane 48, which was caused by a different issue.

Officially, period 2 is divided into 6 epochs labelled by letters, 2a - 2f, based on the specific running conditions. The epochs mostly differ in the use of various FEB firmwares or trigger studies. We compare the energy deposition in various epochs in Fig. 2.23, 2.24 and 2.25. As can be seen, the difference between the energy response across the individual epochs is fairly small and only in normalization. There's also no clear trend of energy response falling or raising with time. The largest outliers seem to be epochs 2a and 2d. Since each individual epoch would not have enough statistics for a successful attenuation fit, we decided to calibrate the entire period 2 together, without splitting it into any smaller samples.

The only variation of energy response in shape can be seen on the distributions along planes in Fig. 2.25. Here, in the top panel of the right plot, we can see that the uncorrected response in plane 55 is noticeably higher than the rest of the detector. The exact reason for this is unknown, but it is likely caused by a fault in one of the two FEBs that make up the plane readout.

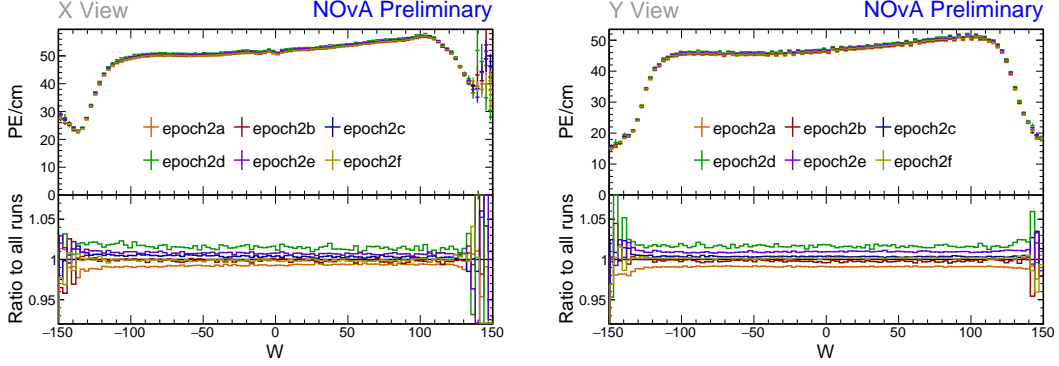


Figure 2.23: Uncorrected average energy response along the position within a cell ( $w$ ) for epochs in period 2. It is clear that there is no significant difference between the various epochs.

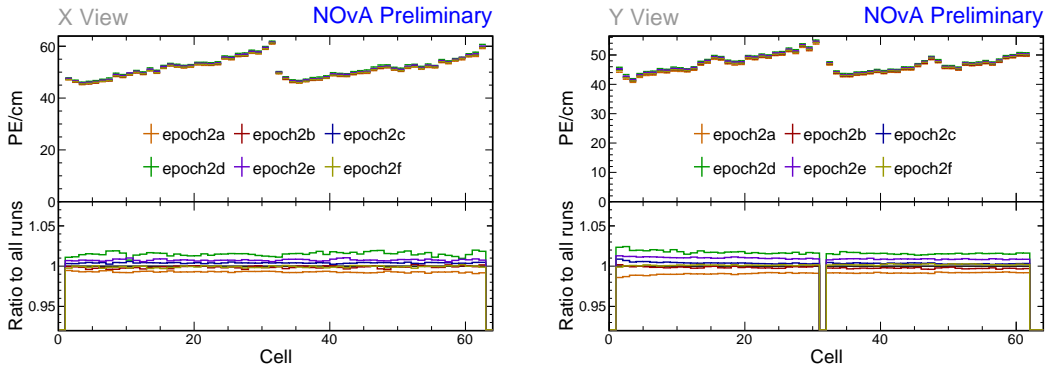


Figure 2.24: Uncorrected energy response along cells for epochs in period 2 data.

## Period 2 Relative Calibration Results

The results of the attenuation fit for period 2 are summarised in Fig. 2.26, showing the map of the fitted response at the centre of each cell. Same as for simulation, the blank cells failed the calibration condition for the attenuation fit. There are 199 cells that failed the calibration condition out of the total 4032 cells, constituting 4.94% of the detector left uncalibrated for period 2.

Most of the cells have an expected response, with steady rise towards the readout and a drop on the edges, as shown on the left plot of Fig. 2.27. This is the same as was shown for simulation.

Some cells have a non-regular response across the cell, with one or more regions with a drop in the energy response, as shown on the right plot of Fig. 2.27. These low regions are (almost certainly) a real physical effect caused by zipped, or possibly even twisted, WLS fibres [94]. This effect is present in all the NOvA detectors. As can be seen, the attenuation fit is capable of fitting this response and therefore the

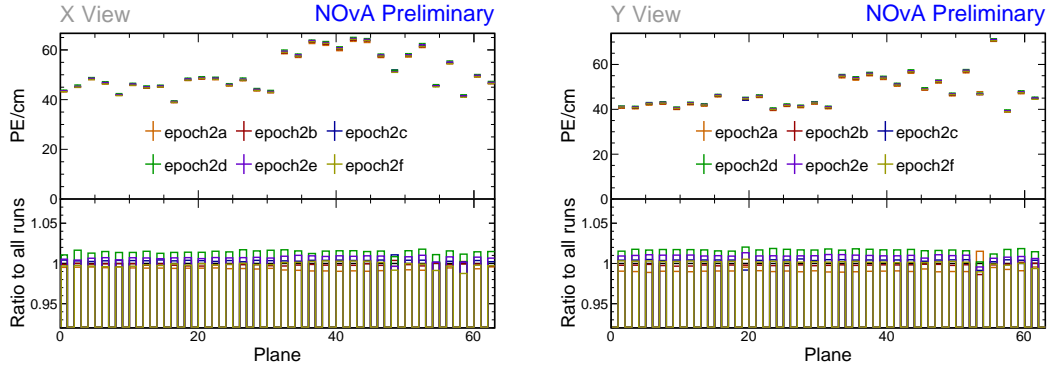


Figure 2.25: Uncorrected average energy response along planes for epochs in period 2 data.

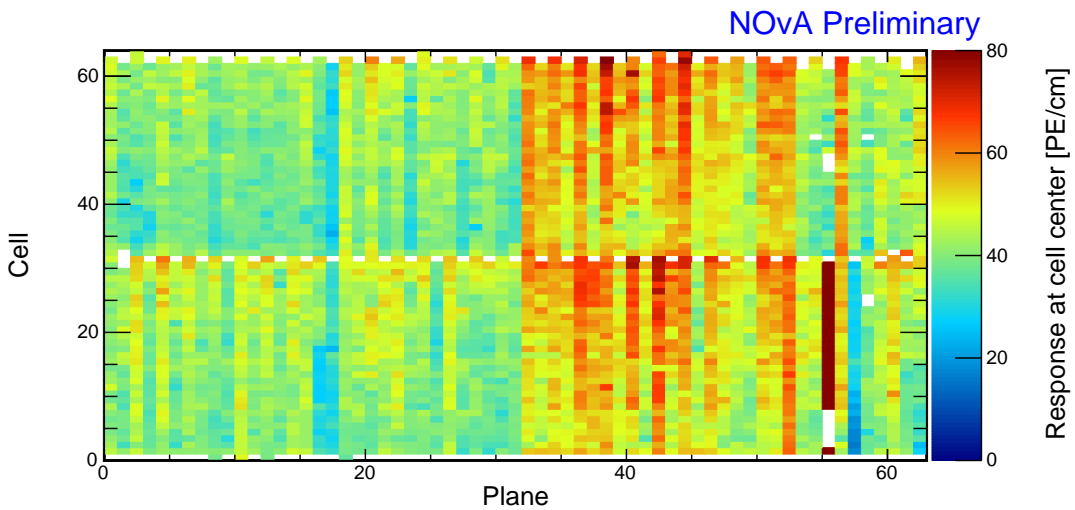


Figure 2.26: Overview of the relative calibration results for the Test Beam detector period 2 data. Each cell represents the result of the attenuation fit to the energy response in the centre of that cell. The blank cells are uncalibrated.

relative calibration corrects for this effect in data. However, zipped fibres are not included in simulation for any of the detectors, which could potentially cause issues with the [ADC](#) threshold in simulation. It was decided that this does not have a significant impact and it would not be worth the amount of work required to include all the zipped fibres into the simulation.

Since the underfilled cells were marked as bad channels, we didn't attempt to calibrate them. Their neighbours have fewer events due to the tricell condition, but majority of them pass the calibration condition, as shown in Fig. 2.28. The decision to mark the underfilled cells as bad channel was motivated by the fact that bad channels get skipped by the tricell condition and the neighbouring cells to the underfilled cells can therefore be included in calibration. The fact that majority of the neighbour-

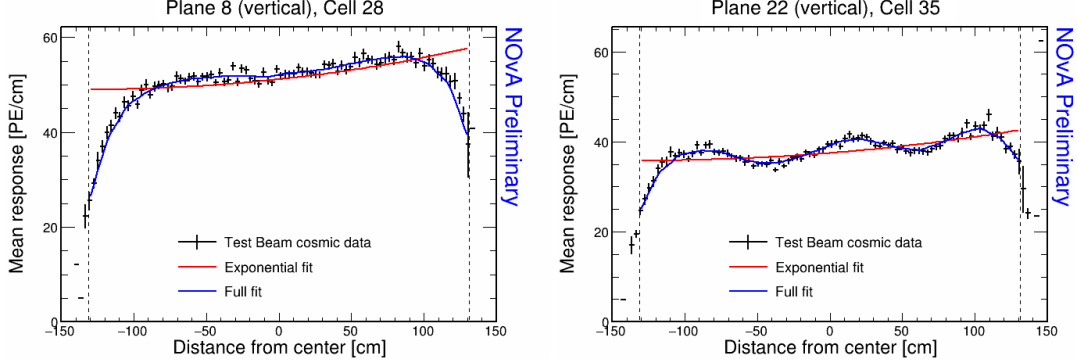


Figure 2.27: Attenuation fits for a selection of cells in period 2. Left plot shows an example of the standard energy deposition in the Test Beam. Right plot shows the effect of zipped fibres.

ing cells to the underfilled cells do get calibrated clearly proves that this was a good decision.

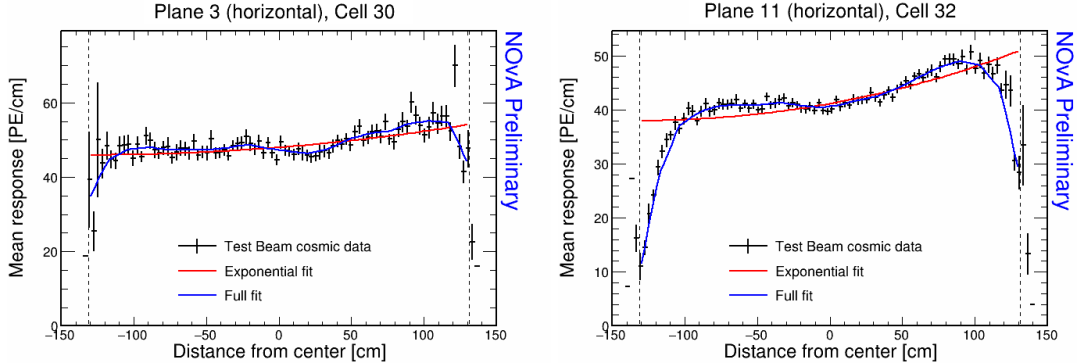


Figure 2.28: Fit to the energy response in period 2. The cells neighbouring the under-filled cells have fewer events and therefore larger fluctuations than the "usual" Test Beam cell.

The neighbouring cells in plane 1 don't pass the calibration condition due to low statistics and therefore large fluctuations, as shown in Fig. 2.29. This is likely due to a combination of the tricell condition and plane 1 being on the edge of the detector, which typically has fewer (accepted) hits than the center, as shown in Fig. 2.22.

The left half of plane 55 has more than  $3\times$  larger response than the surrounding planes, as shown on the left plot of Fig. 2.30. Similarly, the left half of plane 57 has slightly lower response than the surrounding planes, as shown on the right plot of Fig. 2.30. This is due to the corresponding APDs/FEBs incorrectly recording a scaled up/down energy response than the real energy deposited in the detector. The cause of this scaled response is not known. Since this effect is present for all data, not only for the cosmic muons used for the calibration, it is important to correctly calibrate it out.

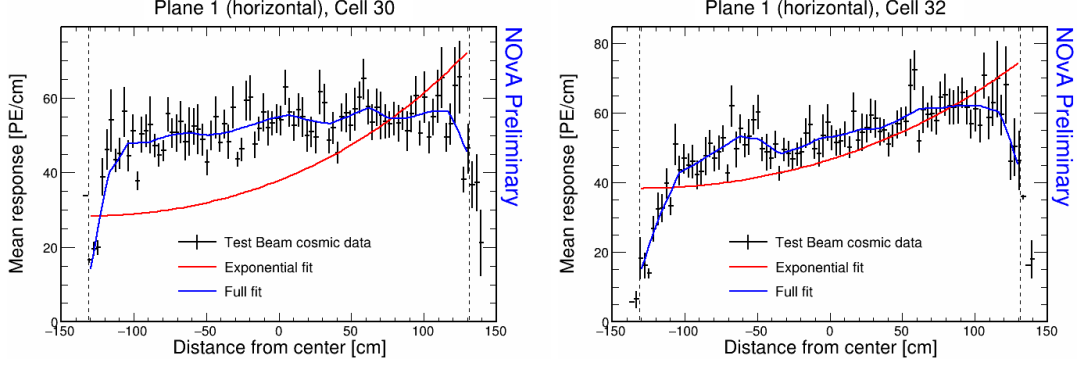


Figure 2.29: Fit to the energy response in period 2. The neighbouring cells to the underfilled cells in plane 1 are uncalibrated due to low statistics.

A reason for concern is that this issue can arise if these FEBs were only affected for a limited time out of the entire calibrated period. Since we are doing the attenuation fit on the average response across the whole calibrated period, if an FEB records a standard response for half of the time and  $7\times$  larger response for the second half, calibration is going to assume the response was  $4\times$  larger the entire time, which would be incorrect. However, since both of the affected planes are in the back of the detector, we decided to ignore this effect for period 2.

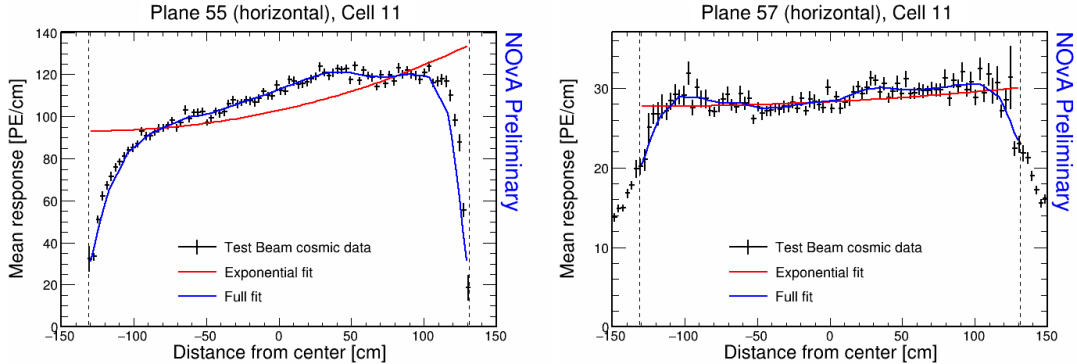


Figure 2.30: Fit to the energy response in period 2. Lower halves of planes 55 and 57 have a different scale of energy response than the surrounding planes.

As was discussed above, there are three dead channels with lower number of hits, possibly caused by swapped cables. These are located in planes 48 and 55. An example of one of the dead channels in plane 55 is shown on the left of Fig. 2.31 together with one of the neighbouring cells on the right. As can be seen in Fig. 2.26, the dead channel in plane 48 and its neighbours were successfully calibrated despite the lower number of hits.

Several cells in the end of the Test Beam detector are uncalibrated due to the

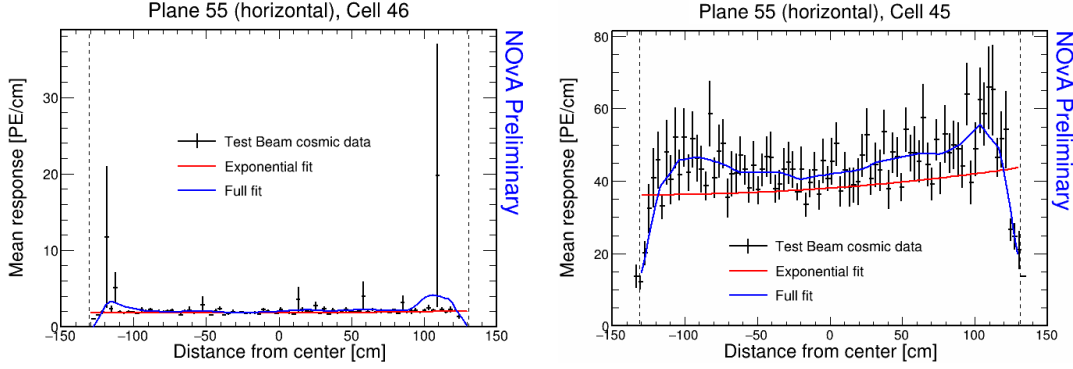


Figure 2.31: Fit to the energy response in period 2. Cells with swapped readout cables have almost no recorded events as shown on the left. This also affect their neighbouring cells due to the tricell condition as shown on the right.

histogram bins on the edges of the cell having an unusually high response, or no events at all, as shown in Fig. 2.32. It is unknown if this is a real physical effect, possibly related to the fibres, or if it is unfiltered noise hits, issue with the binning, or something else entirely. Since these cells are in the end of the detector, we decided to ignore them.

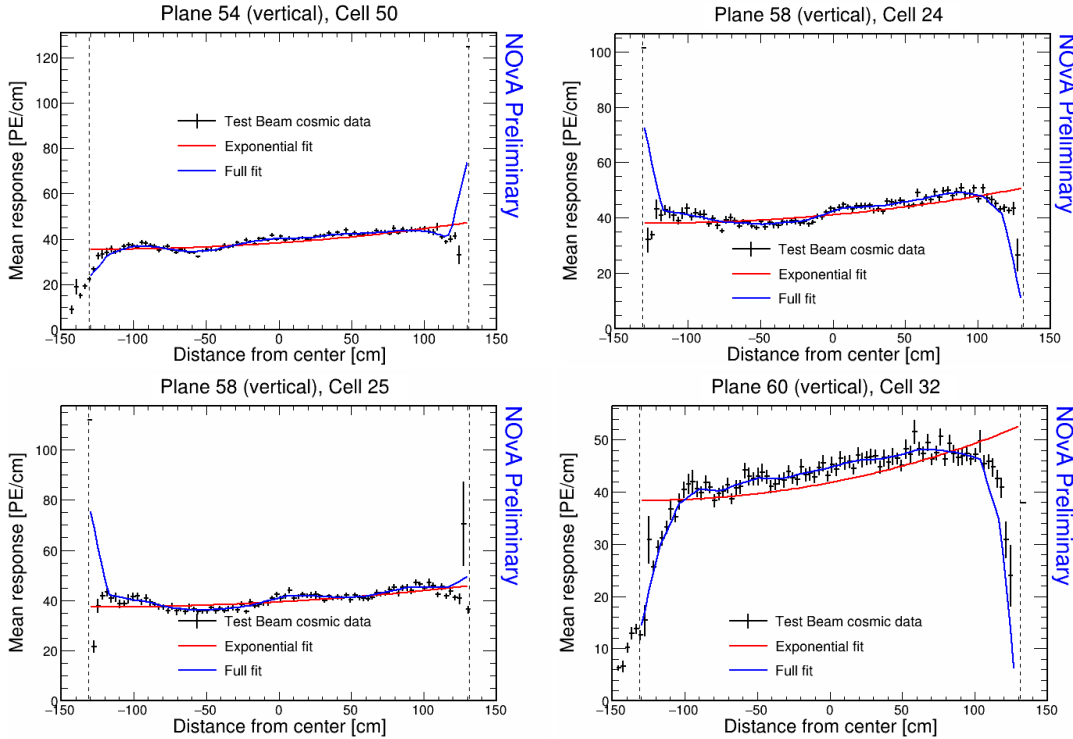


Figure 2.32: Fit to the energy response in period 2. Examples of cells that have an unusually high or low energy response at the edge of the cell. These cells are not calibrated.

### 2.3.5 Period 3 Data

The underfilled cells were refilled (or overfilled) during the period 3 data taking. This was the main motivation for dividing period 3 into individual epochs as shown on Tab. 2.3. Another major event that could impact the Test Beam data is the replacement of several faulty FEBs, which motivated the creation of epoch 3e.

Table 2.3: Test Beam period 3 epochs, their start dates and the reason for their separation.

Name	Start date	Reason for creating the epoch
Epoch 3a	January 12 <sup>th</sup> 2021	Underfilled cells
Epoch 3b	April 21 <sup>st</sup> 2021	Overfilling the back 9 horizontal planes and the 7th horizontal plane from the front
Epoch 3c	April 27 <sup>th</sup> 2021	Overfilling of the 15 front horizontal planes (except the 7th, which was already done) and the 14th horizontal plane
Epoch 3d	April 30 <sup>th</sup> 2021	Overfilling of the remaining 8 horizontal planes
Epoch 3e	May 12 <sup>th</sup> 2021	FEB swaps

The refilling of the underfilled cells can be clearly seen on the cell hits distribution in Fig. 2.33 and on the distribution of energy deposition across horizontal cells (Y view) in Fig. 2.35.

From the cell hits distributions in Fig. 2.33 we can also see there are a few channels (cells) that were likely dead for a certain time and weren't recording the same number of events as the surrounding cells. This is specifically plane 48, cell 39 in all of period 3 and plane 18, cell 31 in epochs 3d and 3e. Cell 39 in plane 48 was also affected in period 2.

The energy distributions across cells and planes in the X view (vertical) in Fig. 2.35 and 2.36 shows, that the top half of plane 58 has a very distinctly different energy deposition compared to the rest of the cells. Specifically, that the energy response in this module was larger in epoch 3a, then got lower in epochs 3b and 3c, until getting significantly lower for epochs 3d and 3e. However, Fig. 2.33 shows that module has the same number of events as the surrounding modules. This is one of the FEB that got replaced between epochs 3d and 3e. and as will be shown below this is the FEB with the largest impact on the calibration out of the faulty FEBs replaced before the

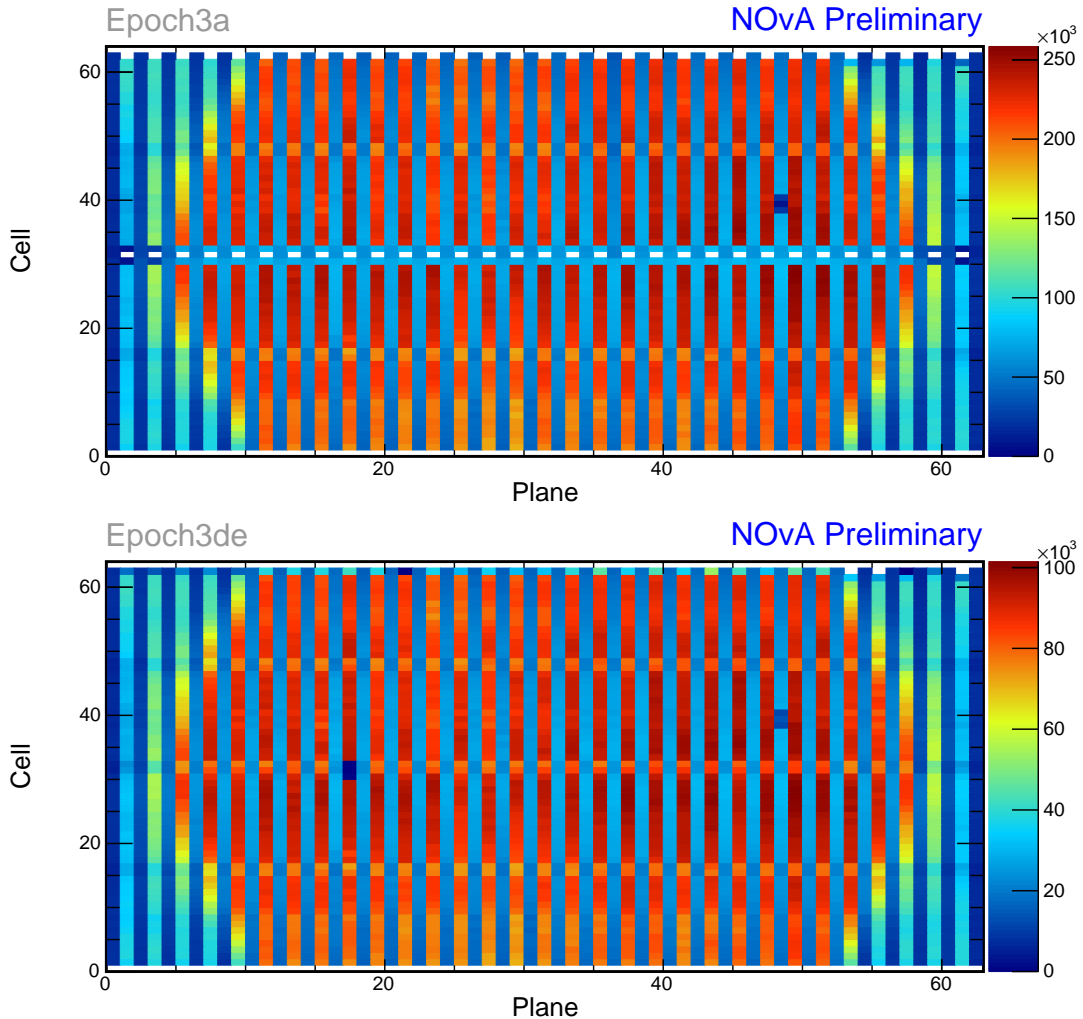


Figure 2.33: Distribution of events in the period 3 Test Beam data calibration sample. Comparison of Epoch 3a data before the refilling of the underfilled cells and Epoch 3de (combination of Epochs 3d and 3e) after the full refilling.

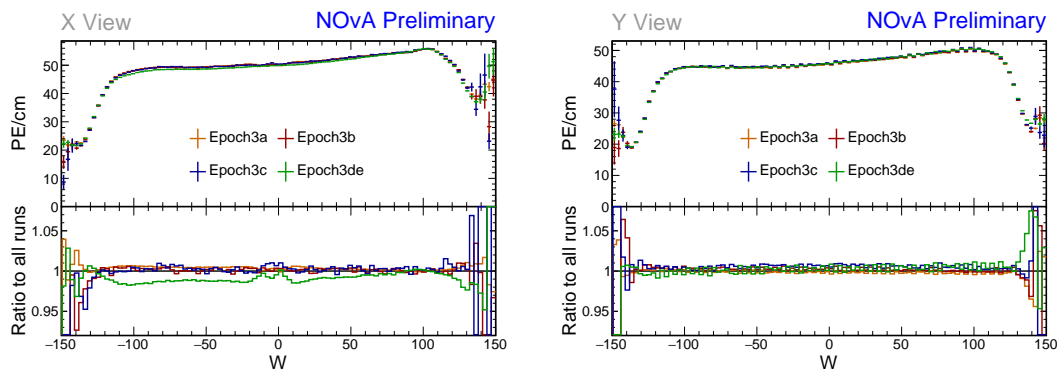


Figure 2.34: Uncorrected average energy response along the position within a cell for epochs in period 3 data.

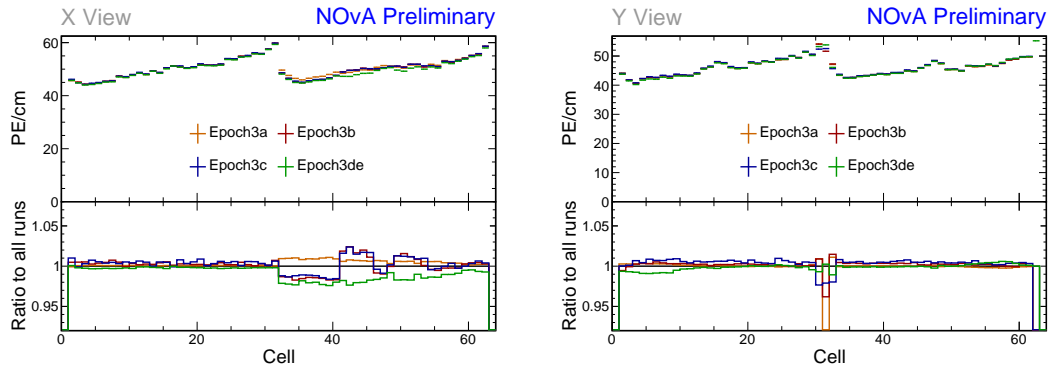


Figure 2.35: Uncorrected average energy response along cells for epochs in period 3 data.

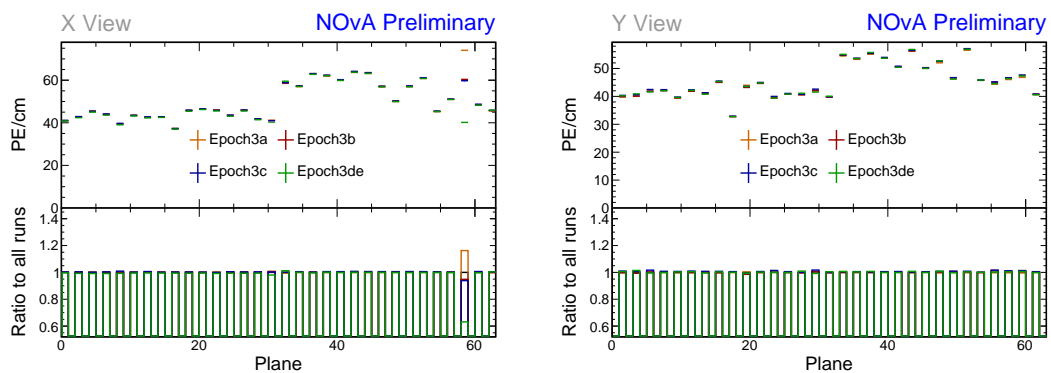


Figure 2.36: Uncorrected average energy response along planes for epochs in period 3 data.

start of epoch 3e.

From the aforementioned considerations, we decided to calibrate epochs 3a, 3b and 3c together, which are all the epochs containing any underfilled cells, and to separately calibrate epochs 3d and 3e together. The faulty **FEB** in the top of plane 58 is far enough in the back of the detector, that we didn't find it necessary to calibrate epochs 3d and 3e separately. Also epochs 3b and 3c only contain a few days worth of data, therefore they wouldn't have enough statistics for a successful attenuation fit.

### Combined Epochs 3a, 3b and 3c Relative Calibration Results

The results of the attenuation fit for the combined epochs 3a, 3b and 3c are summarised in Fig. 2.37, showing the map of the fitted response at the centre of each cell. There are 182 uncalibrated cells out of 4032, constituting 4.51% of the detector.

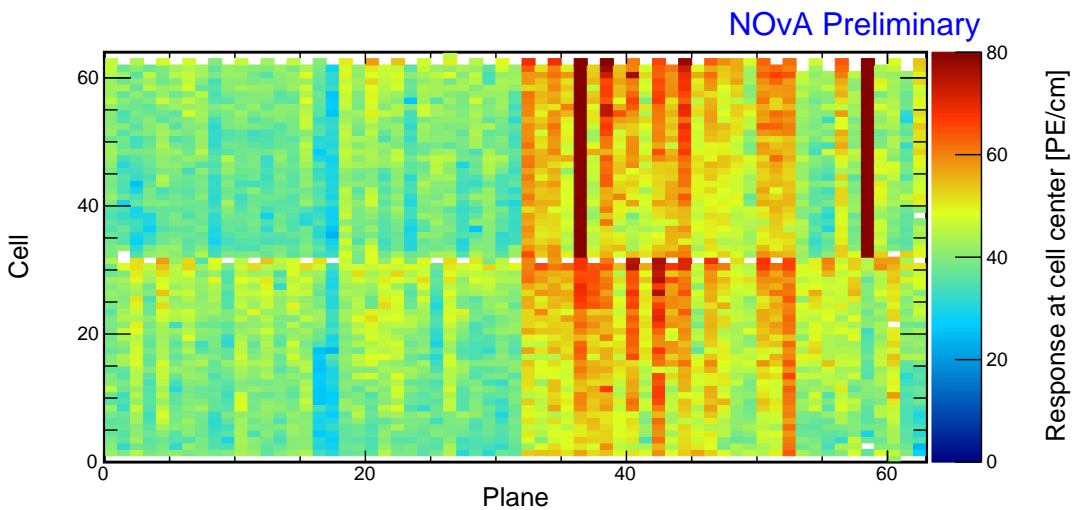


Figure 2.37: Overview of the relative calibration results for the Test Beam detector period 3, combined epochs 3a, 3b and 3c data. Each cell represents the result of the attenuation fit to the energy response in the centre of that cell. The blank cells are uncalibrated.

We can see that some of the underfilled cells that have been refilled for epochs 3b or 3c, but were underfilled for epoch 3a which makes up the majority of this calibrated data, are now calibrated thanks to including these two short epochs into the same attenuation fit. An example of energy deposition in such a cell is on the left side of Fig. 2.38.

Same as in period 2, most of the neighbouring cells to the underfilled cells are calibrated, except for cell 32 in plane 1, shown on the right of Fig. 2.38. This is due to

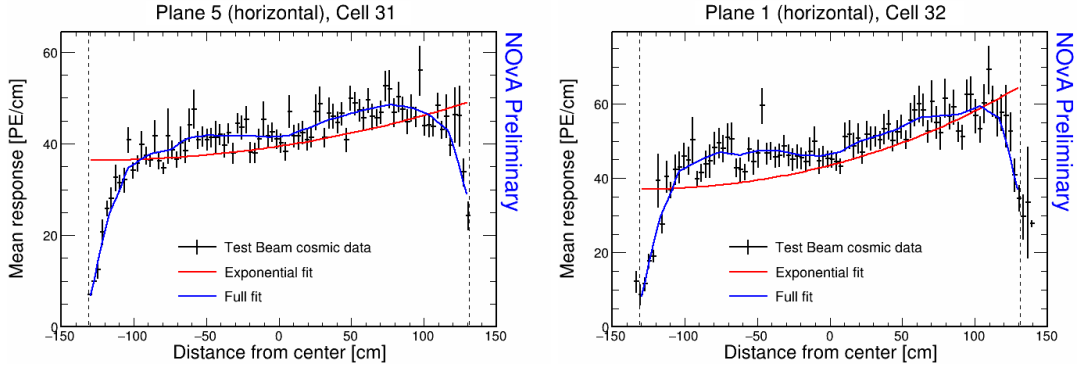


Figure 2.38: Fit to the energy response in epochs 3a, 3b and 3c. Some underfilled cells that have been refilled in epochs 3b and 3c are now calibrated as shown on the left plot. Cell 32 in plane 1 is the only neighbouring cell to the underfilled cell that didn't manage to get calibrated due to low number of events.

the low statistics at the edges of the detector, same as in period 2.

There is a couple of notably faulty FEBs with a different energy response than their neighbours. Besides the expected top half of plane 58, which has about  $5\times$  larger response than the usual, there is also the top half of plane 36, which has about  $2.5\times$  larger response as its neighbours. This could mean that the FEB in plane 36 was faulty only for a limited time compared to the FEB in plane 58. This is a reason for concern, as this could mean that using the results of this attenuation fit for hits in this module when the FEB wasn't faulty would give an incorrectly large correction (and therefore small "corrected response"), whereas hits during the period when the FEB was faulty would have smaller than required correction (and therefore larger corrected response). Given that plane 36 is in the middle of the detector, this might affect some Test Beam analysis results. It is possible this might have to be mitigated in the future, whether with an additional uncertainty, or by improving the calibration.

**COMMENT:** *Should I talk about this further? We decided not to correct this since it would take more time and it might not be a huge problem. But this is probably the most problematic part of the calibration.* The energy deposition for these cells is shown in Fig. 2.39. As plane 58 is in the end of the detector and its readout was likely faulty for the majority of the calibrated period, we decided to ignore this FEB.

Similarly to period 2, there are a few cell in the back of the detector that have a sharp rise in the energy response at the edge of the cell, which causes the attenuation fit to fail the calibration condition. This can be seen in Fig. 2.40 with significantly different mean responses at the edge bins pulling the attenuation fit to incorrect val-

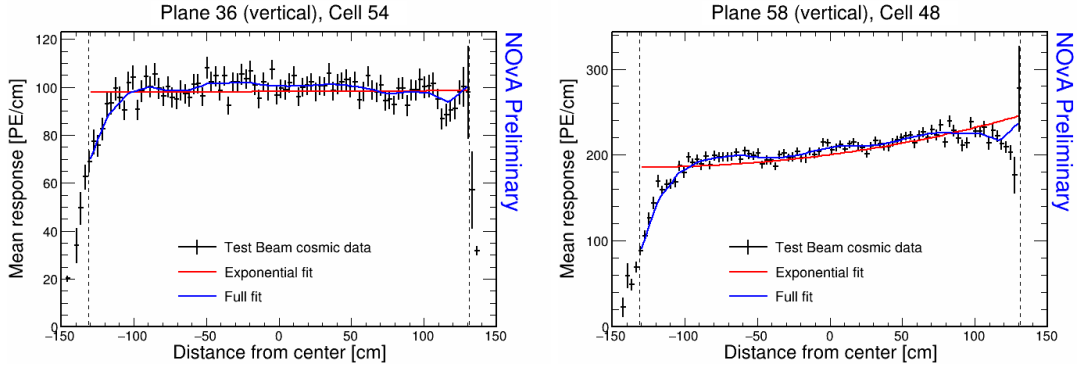


Figure 2.39: Fit to the energy response in epochs 3a, 3b and 3c. The most obvious faulty FEBs that have a significantly larger energy response than their neighbours.

ues. Given this is happening only in the end of the detector, we decided it should be safe to ignore this effect.

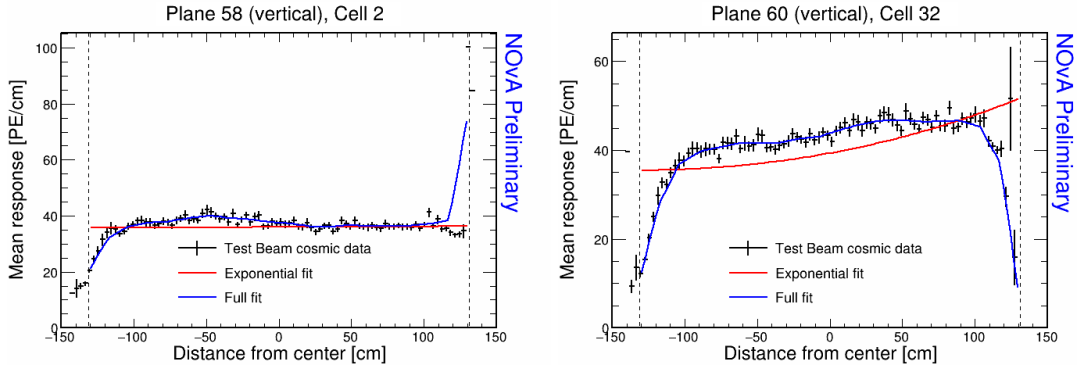


Figure 2.40: Fit to the energy response in epochs 3a, 3b and 3c. Some cells are not calibrated due to large fluctuations at one edge of the cells.

### Combined Epochs 3d and 3e Relative Calibration Results

The results of the attenuation fits for epochs 3d and 3e are shown in Fig. 2.41. There are 182 uncalibrated cells out of 4032 total cells, making up 4.51% of the detector. The uncalibrated are now however almost entirely concentrated at the edges and at the end of the detector.

Figure 2.41 shows the expected uncalibrated cells in plane 17 surrounding the dead channel discussed above (or possibly still an underfilled cell). The energy deposition for this cell and one of its neighbours is shown in Fig. 2.42.

Epochs 3d and 3e should have all the previously underfilled cells now refilled, but as can be seen in Fig. 2.41, there's several of these cells that are still uncalibrated. The energy deposition in these cells is shown in Fig. 2.43. Here we can see, that these

NOvA Preliminary

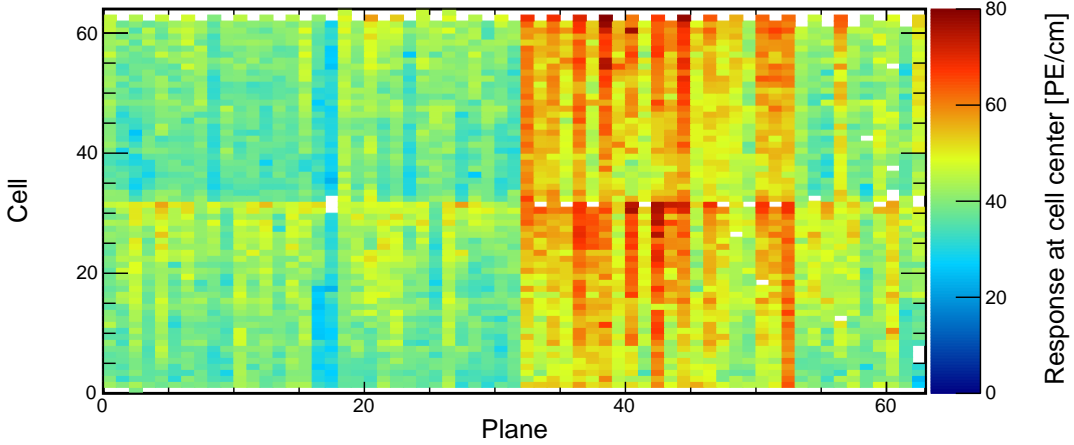


Figure 2.41: Overview of the relative calibration results for the Test Beam detector period 3, combined epochs 3d and 3e data. Each cell represents the result of the attenuation fit to the energy response in the centre of that cell. The blank cells are uncalibrated.

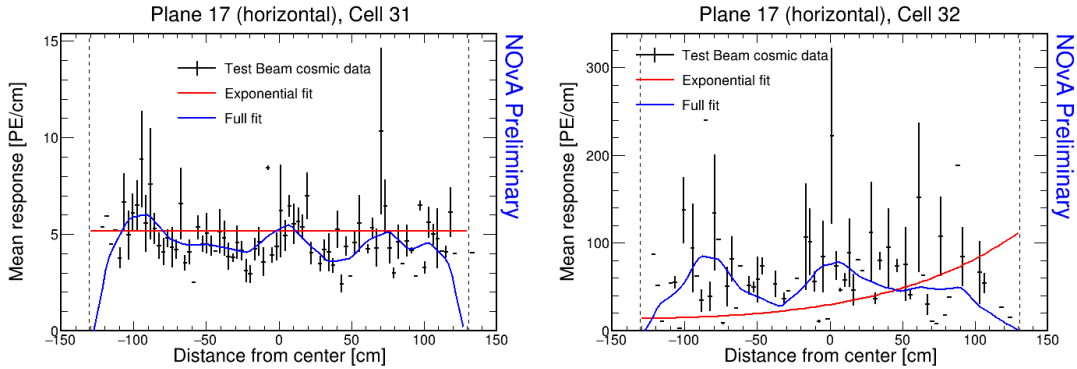


Figure 2.42: Fit to the energy response in epochs 3d and 3e. Possibly dead channel or still underfilled cell.

cells have a fairly large discrepancy between the left and right side of the cells. This is caused by using different scintillator oils for the initial filling of the cells and for the refilling. Specifically, as was described in Sec. 2.1, these cells have been initially filled with the Ash River and the Texas oils, which have higher energy depositions compared to the NDOS oil that was used for the refilling during period 3. These oils clearly didn't mix properly, which caused a difference in energy deposition in different parts of the cells.

This is a physical effect that should be accounted for in the calibration and as we can see, the attenuation fits are actually performing reasonably well. Additionally, these cells are in the middle of the detector and leaving them uncalibrated would almost certainly have an impact on the Test Beam analyses. The large  $\chi^2$  value of the

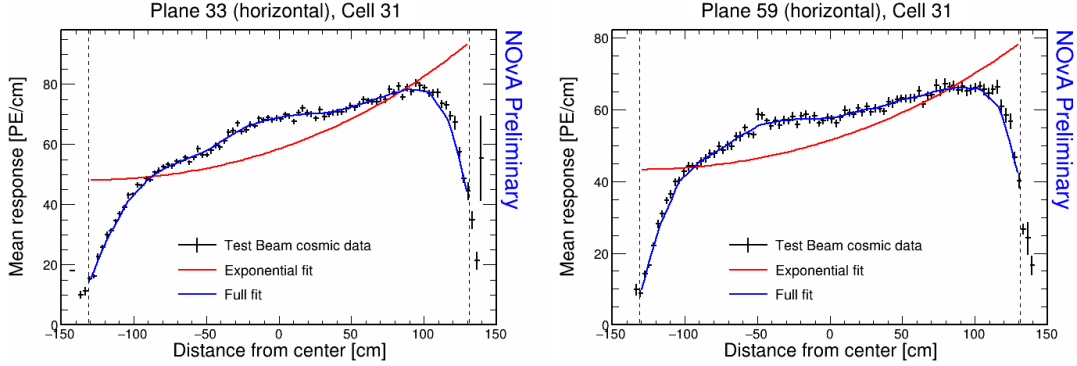


Figure 2.43: Fit to the energy response in epochs 3d and 3e. The scintillator oil used for refilling of the underfilled cells has lower energy response than the oil used for the initial filling. These oils didn't mix properly causing a different energy response in the left and right side of the cell.

attenuation fit is most likely caused only by the unusual shape of the distribution, which the fit is not designed for. We have therefore decided to manually change the  $\chi^2$  values for these cells inside the cvs tables (which hold the results of the attenuation fits), so that their  $\chi^2 < 0.2$  and these cells are officially considered calibrated, even if they originally weren't. The "corrected" distribution of the attenuation fit results for epochs 3d and 3e is shown in Fig. 2.44. The number of uncalibrated cells was reduced by 8 to 174, or 4.32% of the detector.

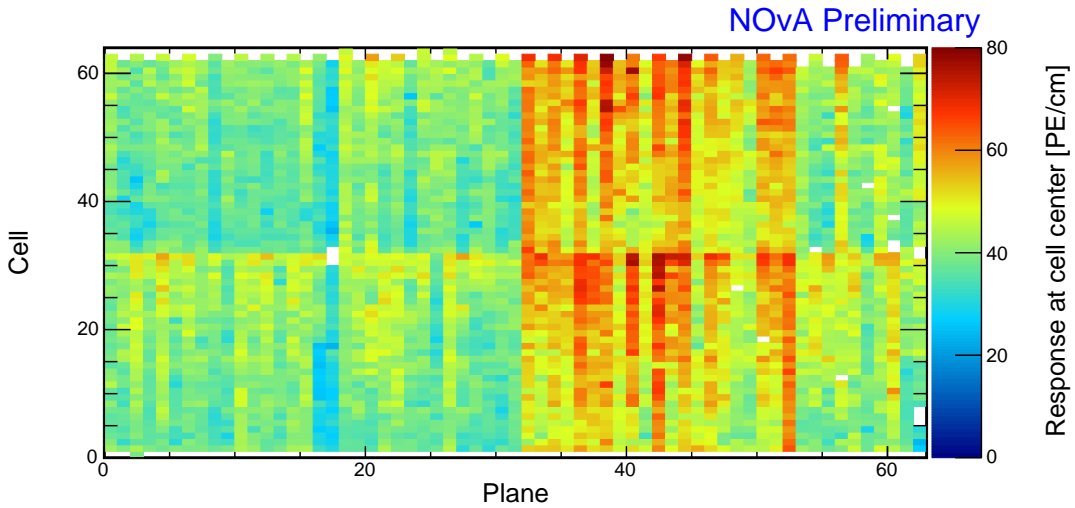


Figure 2.44: Overview of the relative calibration results for the Test Beam detector period 3, combined epochs 3d and 3e data. Each cell represents the result of the attenuation fit to the energy response in the centre of that cell. The blank cells are uncalibrated. The previously uncalibrated cells in the middle of the detector were artificially marked as calibrated after careful considerations.

Some of the cells in the back of the detector have a rise, or drop in energy depo-

sition at the edge of the cell, as can be seen in Fig. 2.45. This is similar to the effect seen in period 2 and epochs 3a+3b+3c and since it's again concentrated in the end of the detector, we ignored these cells and left them uncalibrated.

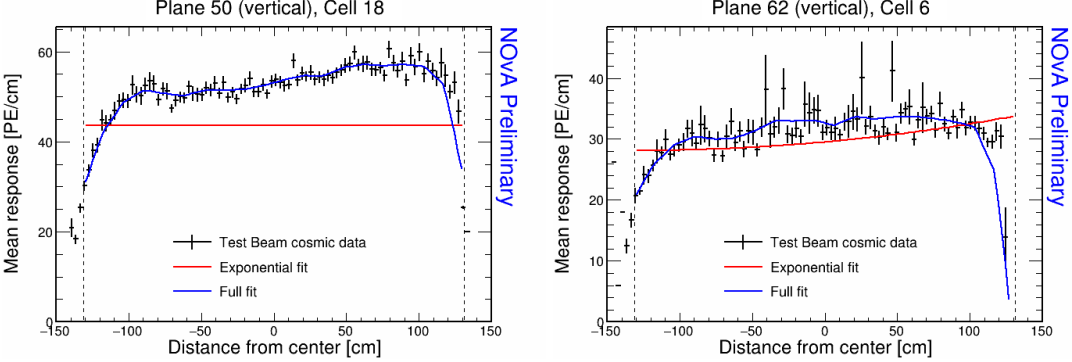


Figure 2.45: Fit to the energy response in epochs 3d and 3e. Some cells have a drop, or a rise of energy response at the edge of the cell. This can be cause by low statistics.

### 2.3.6 Period 4 Data

The period 4 Test Beam data taking period is the best data we managed to collect with almost ideal detector conditions. There are a few commissioning runs in the very beginning of period 4, which uncovered some dead channels or faulty FEBs that were immediately fixed. These runs constitute epoch 4a, shown on the top of Fig. 2.46. There is also a few runs during which we performed studies in which we masked parts of the detector to help with the FEB saturation [95], which can clearly be seen in the middle of Fig. 2.46. Bottom part of Fig. 2.46 shows that the rest of the period 4 data does not have any noticeable faults in the distribution of hits across the detector.

Figures 2.47, 2.48 and 2.49 show that the epoch 4a and the cell masking study did have a noticeable impact on the energy deposition across the detector. Both of these special periods only span a short time and contain a very limited number of hits. We therefore decided to ignore these runs and only calibrate the rest of the period 4 data, using these results for all runs in period 4. *COMMENT: I assume here that the runs from the cell masking studies will not be used in the TB analyses. Is that correct?*

### Period 4 Relative Calibration Results

Results of the attenuation fits for period 4 are summarised in Fig. 2.50. We can see that almost the entire detector is now calibrated. The only exceptions consists of cells

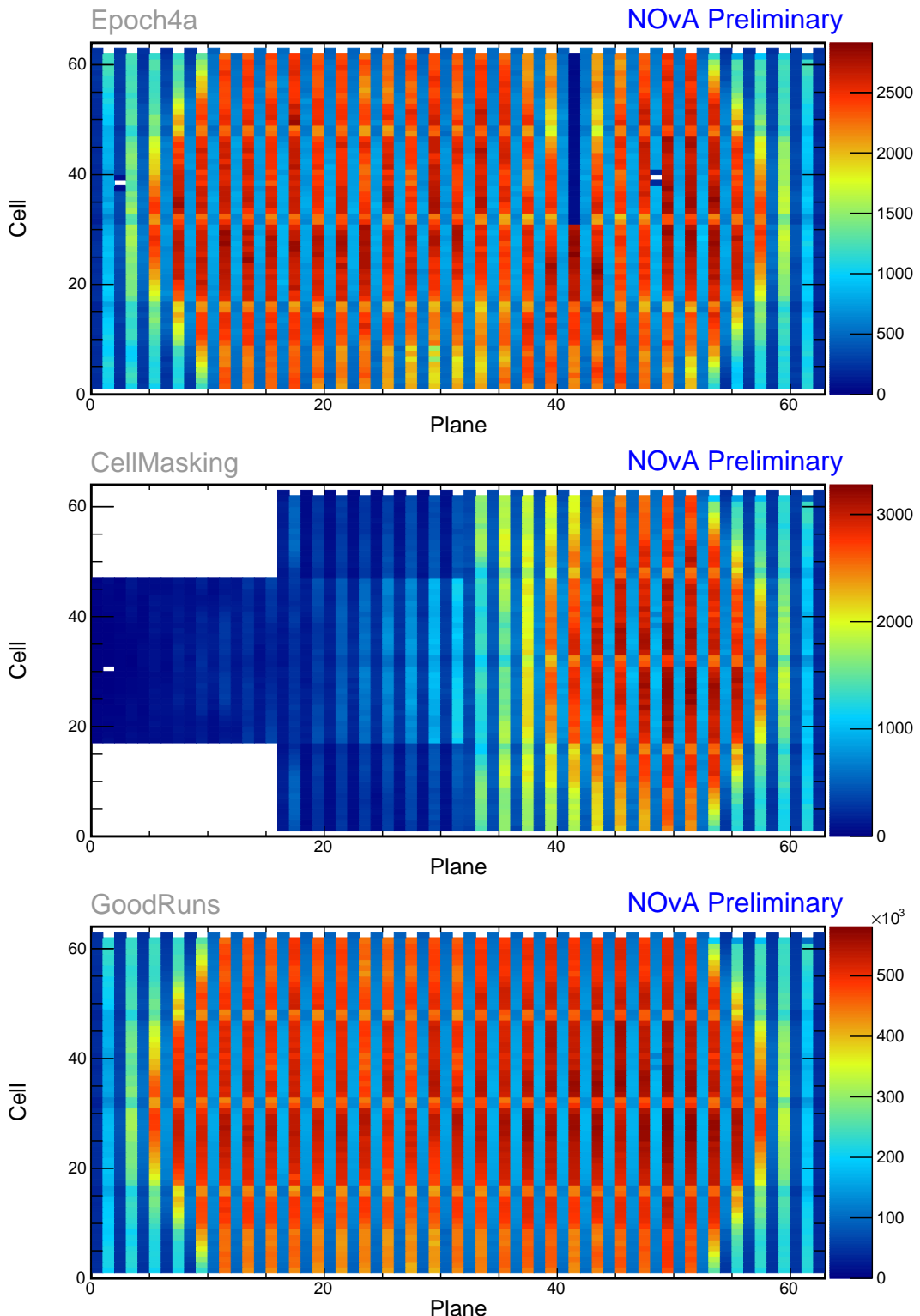


Figure 2.46: Distribution of events in the Test Beam period 4 data calibration sample. The top plot shows the first three commissioning runs, the middle plot the status of the detector during the Cell Masking studies and the bottom plot shows the rest.

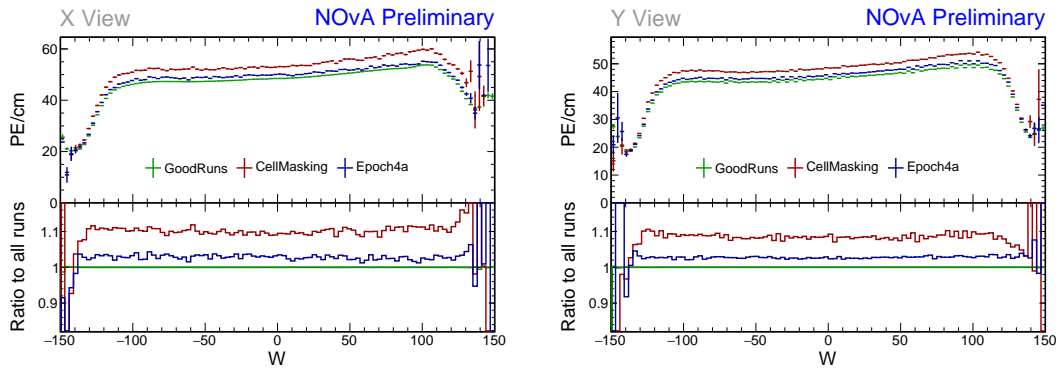


Figure 2.47: Uncorrected average energy response along the position within a cell ( $w$ ) for epochs in period 4 data.

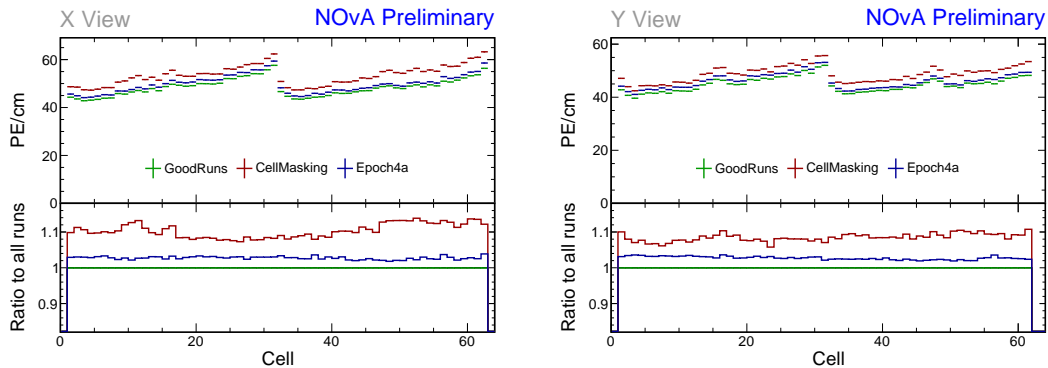


Figure 2.48: Uncorrected average energy response along cells for epochs in period 4 data.

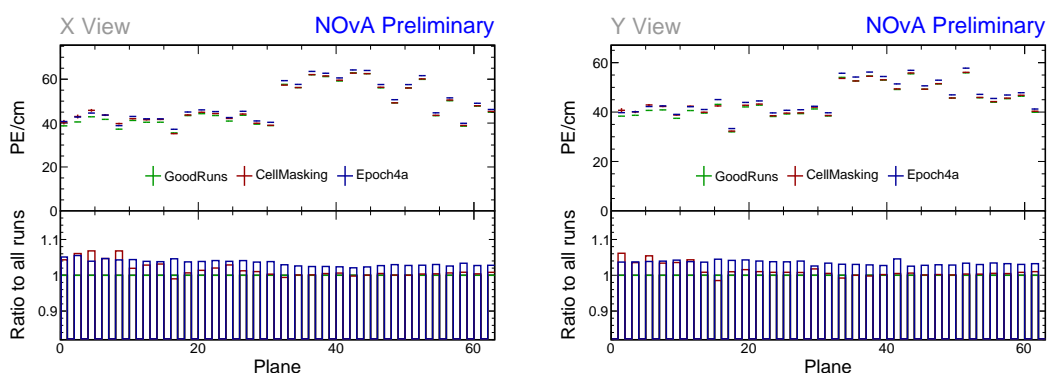


Figure 2.49: Uncorrected average energy response along planes for epochs in period 4 data.

on the edge of the detector, 7 formerly underfilled cells (left plot in Fig. 2.51), and one cell 47 in plane 54 with an unusually high response at the edge of the cell (right plot in Fig. 2.51).

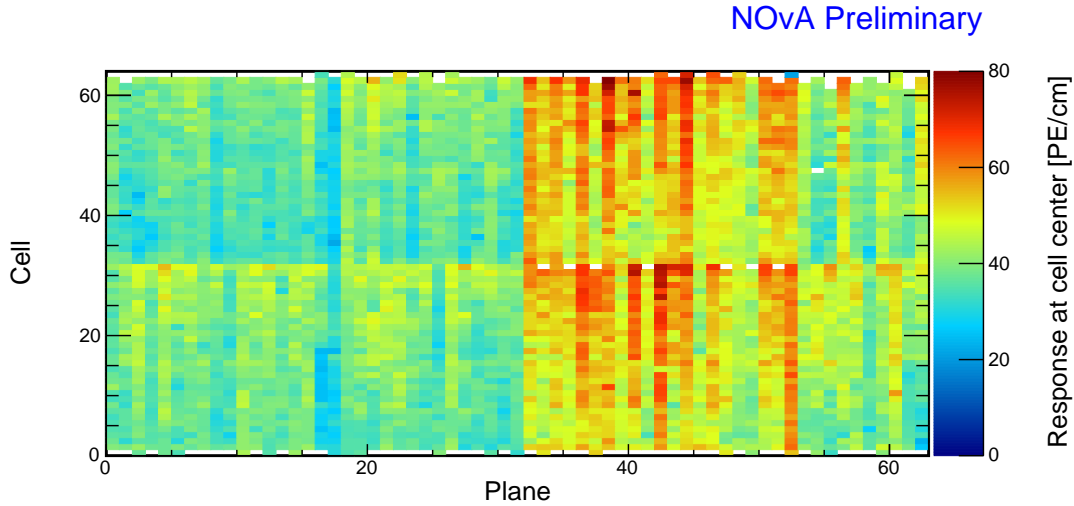


Figure 2.50: Overview of the relative calibration results for the Test Beam detector period 4 data. Each cell represents the result of the attenuation fit to the energy response in the centre of that cell. The blank cells are uncalibrated.

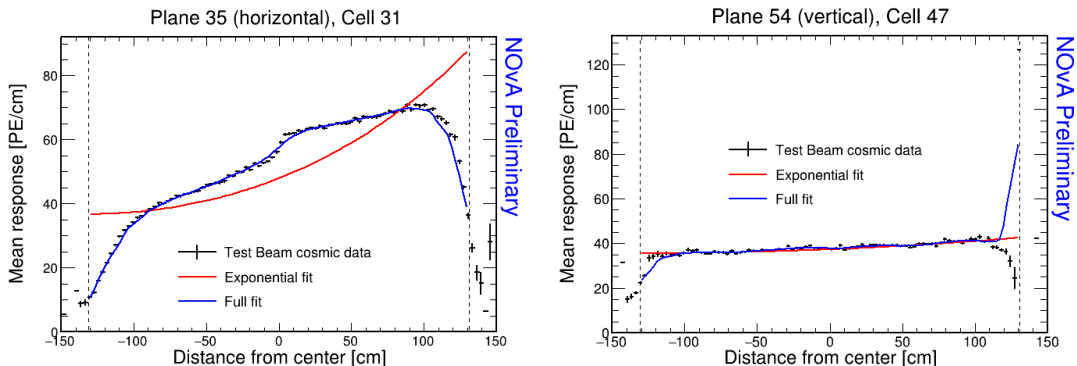


Figure 2.51: Fit to the energy response in period 4. Previously underfilled cells refilled with a scintillator of a different quality causing an unusual distribution of energy deposition (left). Unusually high energy response at the edge of the cell 47 (right).

We treated the formerly underfilled cells the same way as in epochs 3d and 3e, by manually changing the  $\chi^2$  of their attenuation fits inside the csv files to be  $< 0.2$  and therefore making them officially calibrated. The "corrected" distribution of the relative calibration results is shown in Fig. 2.52. There are 108 uncalibrated cells out of 4032, totalling 2.68% of the detector, almost exclusively on the edges.

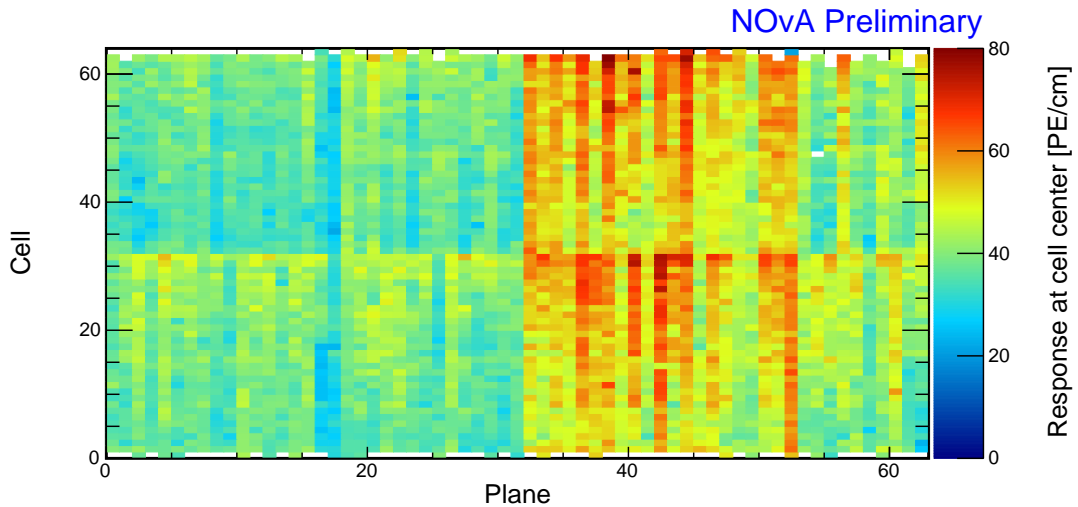


Figure 2.52: Overview of the relative calibration results for the Test Beam detector period 4 data. Each cell represents the result of the attenuation fit to the energy response in the centre of that cell. The blank cells are uncalibrated. The previously uncalibrated cells in the middle of the detector were artificially marked as calibrated after careful considerations.

End of the current version of the thesis!

Anything after this point was simply copied from the technote and hasn't been review yet

### 2.3.7 Absolute Calibration Results

To get the absolute energy scale we look at the stopping muon sample, apply the relative calibration results and the absolute calibration cuts to select only well-understood minimum ionising muons. The absolute calibration cuts are mostly the same as for the other detectors (hits 1-2 m from the end of track, pathlength  $> 0$ , PE  $> 0$ , PECorr  $> 0$ , PECorr/cm  $< 100$ ), but with a smaller cell window  $-80 < w < 80$  cm to remove hits at the cell edges.

We then look at the distributions of the reconstructed energy response in units of PECorr/cm (for all data and simulation samples), and true energy response in units of MeV/cm (only for simulation) in each view, as shown in Fig. 2.53. The mean of these distributions is the  $\text{MEU}_{\text{Reco}/\text{True}}$  value for each view, with an uncertainty calculated as  $\text{StdDev}/\sqrt{N_{\text{Entries}}}$  from the distribution. The MEU for each sample and view is shown on Tab. 2.4.

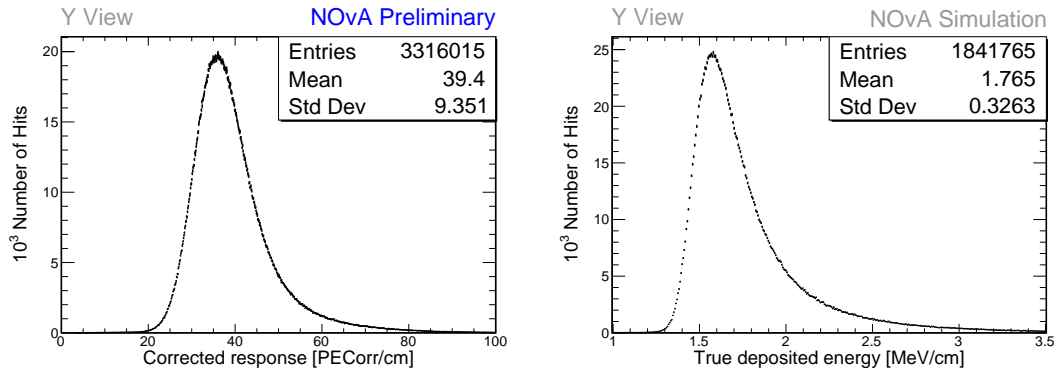


Figure 2.53: Example distributions of reconstructed (left) and true (right) energy response of stopping muons 1-2 m from the end of their tracks. The mean of the reconstructed (true) response is the reconstructed (true) MEU unit.

Sample		X view		Y view		Combined	
		NHits	MEU	NHits	MEU	$\text{MEU}_{\text{Reco}}$	$\sigma_{\text{MEU}_{\text{Reco}}}$
Data	Period 2	2.322e+05	38.70	1.413e+06	39.40	39.05	0.02
	Epochs 3abc	2.638e+05	38.49	1.621e+06	39.40	38.94	0.02
	Epochs 3de	1.049e+05	38.63	6.725e+05	39.42	39.02	0.03
	Period 4	5.268e+05	38.63	3.316e+06	39.40	39.01	0.01
Simulation		2.829e+05	40.17	1.842e+06	39.93	40.05	0.02

$$\text{MEU}_{\text{True}} = 1.7722 \text{ MeV/cm} \quad \sigma_{\text{MEU}_{\text{True}}} = 0.0003 \text{ MeV/cm}$$

Table 2.4: Table of the absolute calibration results.  $\text{MEU}_{\text{Reco}}$  values (top table) are in units of PECorr/cm and  $\text{MEU}_{\text{True}}$  values (bottom table) are in units of MeV/cm

We don't apply the absolute energy scale separately for each view, instead we

combine the two views into a single  $\text{MEU}_{\text{Reco}}$ , or  $\text{MEU}_{\text{True}}$  value. To combine the  $\text{MEU}$  value we take a simple average  $(\text{MEU}_X + \text{MEU}_Y)/2$ , without accounting for the different statistics of the two views. To get the uncertainty on the final value, we calculate it as  $\sigma_{\text{Combined}}^2 = \sigma_X^2 + \sigma_Y^2$ . In the past (and for the other NOvA detectors), this uncertainty was calculated as  $1/\sigma_{\text{Combined}}^2 = 1/\sigma_X^2 + 1/\sigma_Y^2$ . This uncertainty is however **not** the uncertainty used in NOvA for the absolute energy scale. Instead, we use a data-simulation comparison of special samples to derive an uncertainty on the absolute energy scale [? ]. The final combined values are highlighted in Tab. 2.4. Here  $\text{MEU}_{\text{Reco}}$  values are all in units of PECorr/cm.

For each calibrated sample we write the combined  $\text{MEU}_{\text{Reco}}$  value into an `calib-  
abs_consts.csv` file, together with its uncertainty and with the  $\text{MEU}_{\text{True}}$  value, which is common for all samples.

### 2.3.8 Results

The results of the relative and the absolute calibration, in form of the csv files, are stored in `/grid/fermiapp/products/nova/externals/calibcsvs/` and are applied within NOvASoft in the calibration tag v15.09 and higher.

The csv files follow the official NOvA calibration naming convention, which is `calib-{abs/atten}-{consts/points}.{nd/fd/tb}.{data/mc}.{version}.{pe}`. Here `version` is the calibration tag (i.e. v15) and `period` is the range of runs for that sample (i.e. `r100857-r101356` for the combined epochs 3a, 3b, and 3c, or `r-r` for simulation, since it is not divided into different periods).

To create the calibration tag we've asked Lisa Koerner for help. Lisa is a NOvA calibration expert who wrote the instructions for calibration tagging [? ]. It is possible to do it ourselves following these instructions, but it is advised to consult the detector systematics group before hand.

We have also stored the final calibration results in a special location created for safekeeping of Test Beam calibration files: `/nova/ana/testbeam/calibration/`. Here we have also copied all of the attenuation profiles used in the relative calibration. These can be very useful in case someone wants to re-do the calibration, as it allows to skip the prestaging of the calibration plist samples (the pliststop samples are much smaller and therefore easier to prestage). If there has been no change to

the calibration samples, it is possible to skip the creation of attenuation profiles and reuse the existing files.

### 2.3.9 Validation

To validate the results of the Test Beam calibration we look at the stopping muon sample used for the absolute calibration, since these events have the most consistent and reliable energy deposition.

In plots in Fig. 2.54-2.67 we look at distributions of variables used during the calibration, namely  $PE$ ,  $PECorr$ ,  $Pathlength$ ,  $PE/cm$  and  $PECorr/cm$ . Their distributions are over a range of variables we tried to correct the energy deposition in, namely position within a cell  $w$ , cell number, plane number, track angles and time.

The most important validation plots are the distributions of  $PECorr/cm$ , which should be completely flat. This would mean that all the deposited energy results in an equivalent recorded energy wherever and whenever in the Test Beam detector it occurred. As can be seen on the validation plots, this was successfully achieved and the  $PECorr/cm$  distributions are mostly flat across all studied variables.

The distribution of  $PECorr/cm$  across cells in X view in Fig. 2.58 seems fairly scattered, however this is mostly due to the better resolution of this plot and the dispersion of the energy deposition across cells isn't large enough to constitute further investigation.

The distributions of  $PECorr/cm$  across planes in the X view (Fig. 2.58) shows a noticeable smaller corrected energy response of stopping muons in plane 36. This means that the relative calibration over-corrected the energy response due to the through-going muons having unusually high energy response (as shown in Fig. 2.39), but not the selected stopping muons. The most likely cause is that the impacted FEB was "faulty" only for a certain period of time. In that case the corrected energy response would be correct for the period when the FEB was faulty, but would be under-estimated for the period when the FEB behaved "normally". The  $PECorr/cm$  over Plane plot shows the average over these responses.

The corrected response across planes in Y view (Fig. 2.58) shows a slight incline in the first half of the detector. We do not know where does this slope come from, but it is not big enough to be of concern and we decided to ignore it.

The distributions of energy deposition in time (Fig. 2.66 and 2.67) show a non-trivial dependency. The detector response could be influenced by environmental factors (temperature and humidity) and by scintillator or readout ageing. Neither of these factors are well understood within NOvA and Test Beam detector could be potentially used to shine more light on this issue. However this is a topic for a separate study and is out of scope of this technical note.

Technically, we would expect the distributions of  $PECorr/cm$  to also have the same **scale** for all data samples and for simulation. As can be seen on all the validation plots, the data samples have a reasonably similar scale of  $PECorr/cm$ , but this is noticeably different for simulation. This is caused due to the data-based simulation we are using does not have a correct energy estimation for through-going muons, which have generally underestimated energies [? ]. This results in an over-estimated correction from the relative calibration. However, this is not an issue, since we only use stopping muons to calculate the absolute energy scale and stopping muons have correct energies in the new simulation.

## 2.4 Conclusion

We have successfully calibrated the NOvA Test Beam detector for all the Test Beam run periods in both data and simulation. The calibration results are implemented in the v15.09 version of the NOvASoft calibration tag. We haven't attempted to estimate the uncertainty of the calibration, which is a separate task out of scope of this technical note.

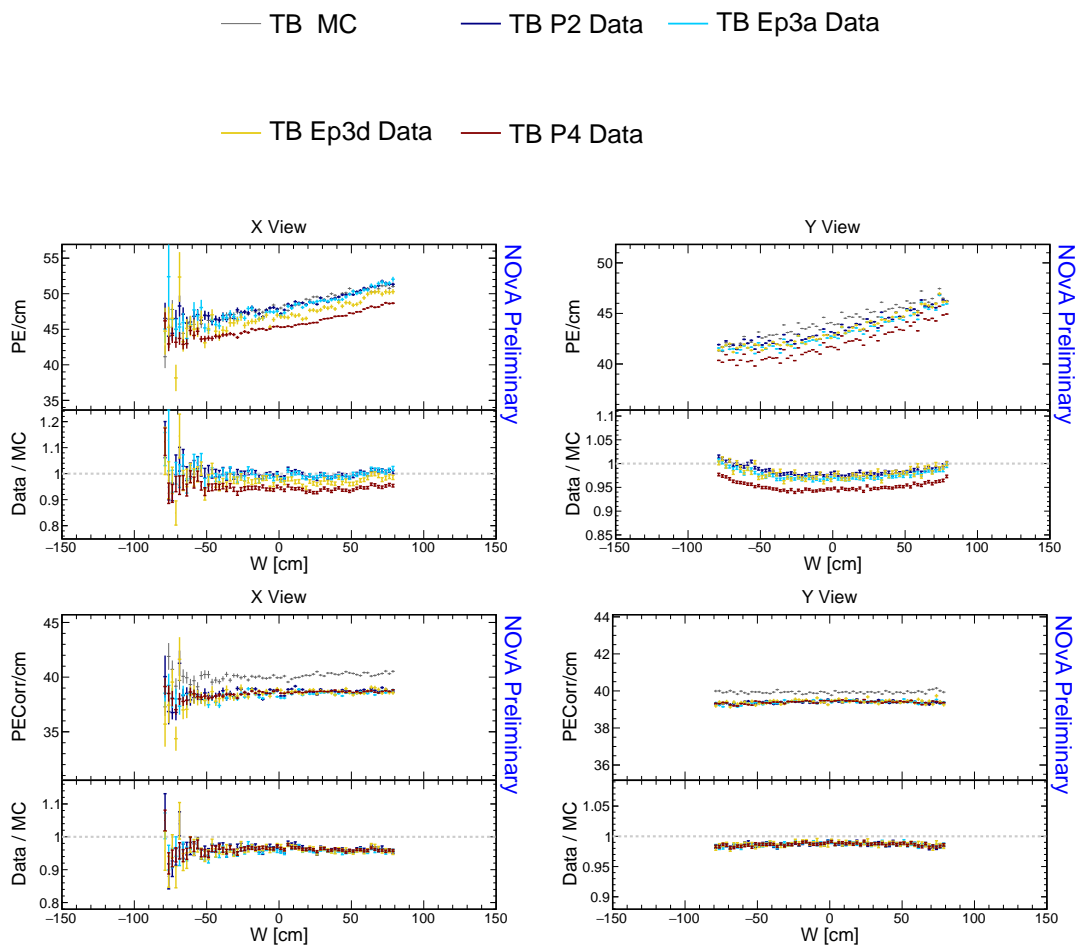


Figure 2.54: Distributions of stopping muons within a 1-2 m track window from the end of their tracks across the position within a cell.

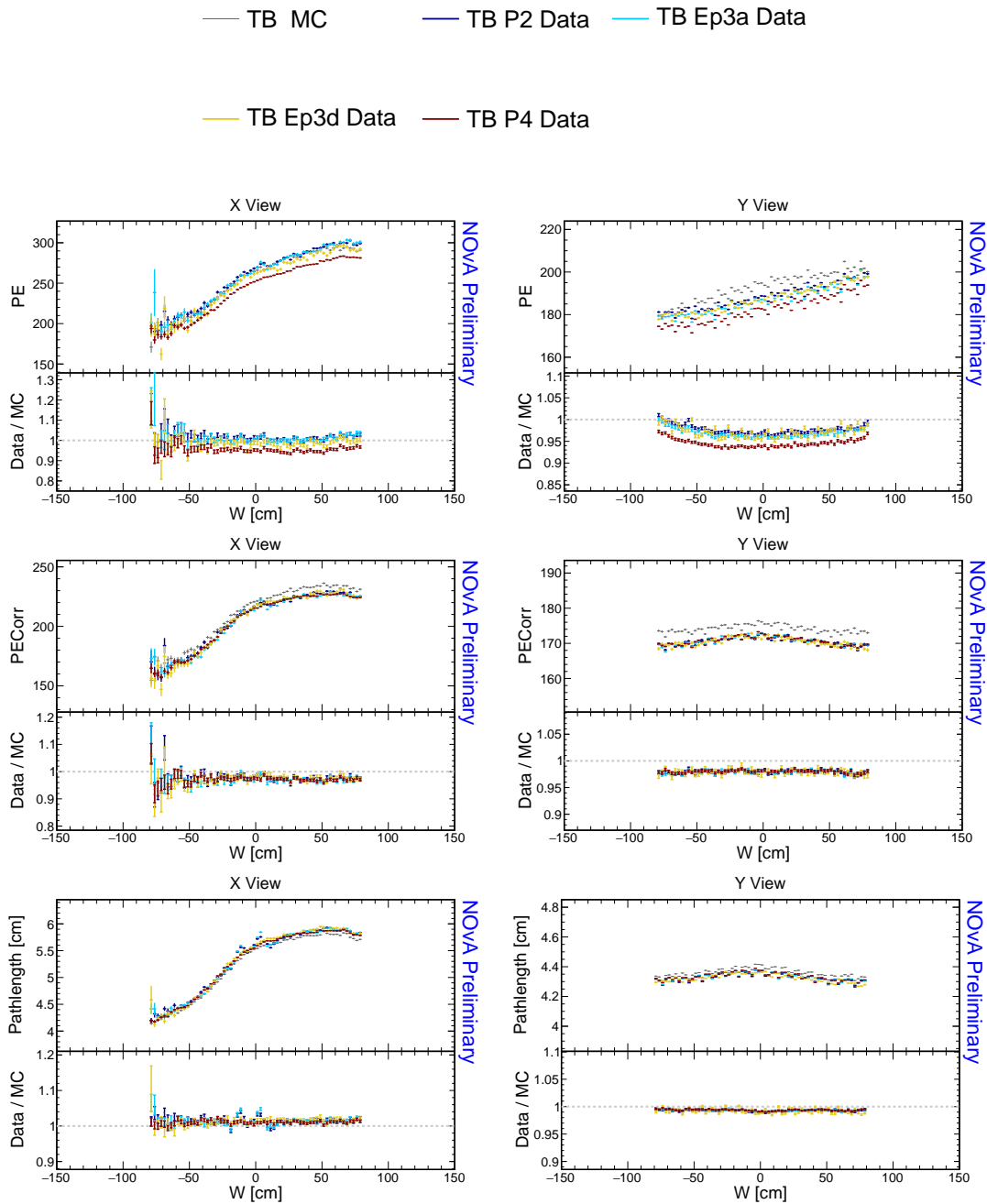


Figure 2.55: Distributions of stopping muons within a 1-2 m track window from the end of their tracks across the position within a cell.

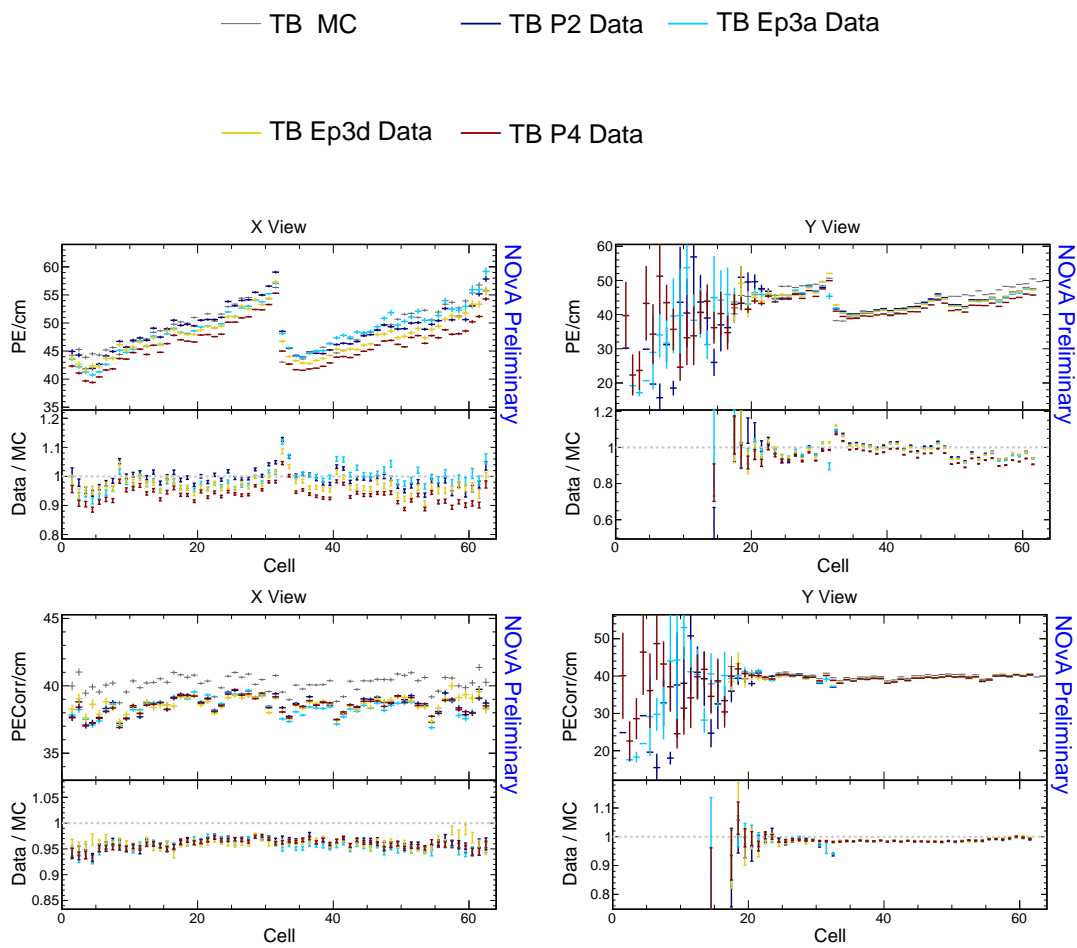


Figure 2.56: Distributions of stopping muons within a 1-2 m track window from the end of their tracks across the cells of the detector.

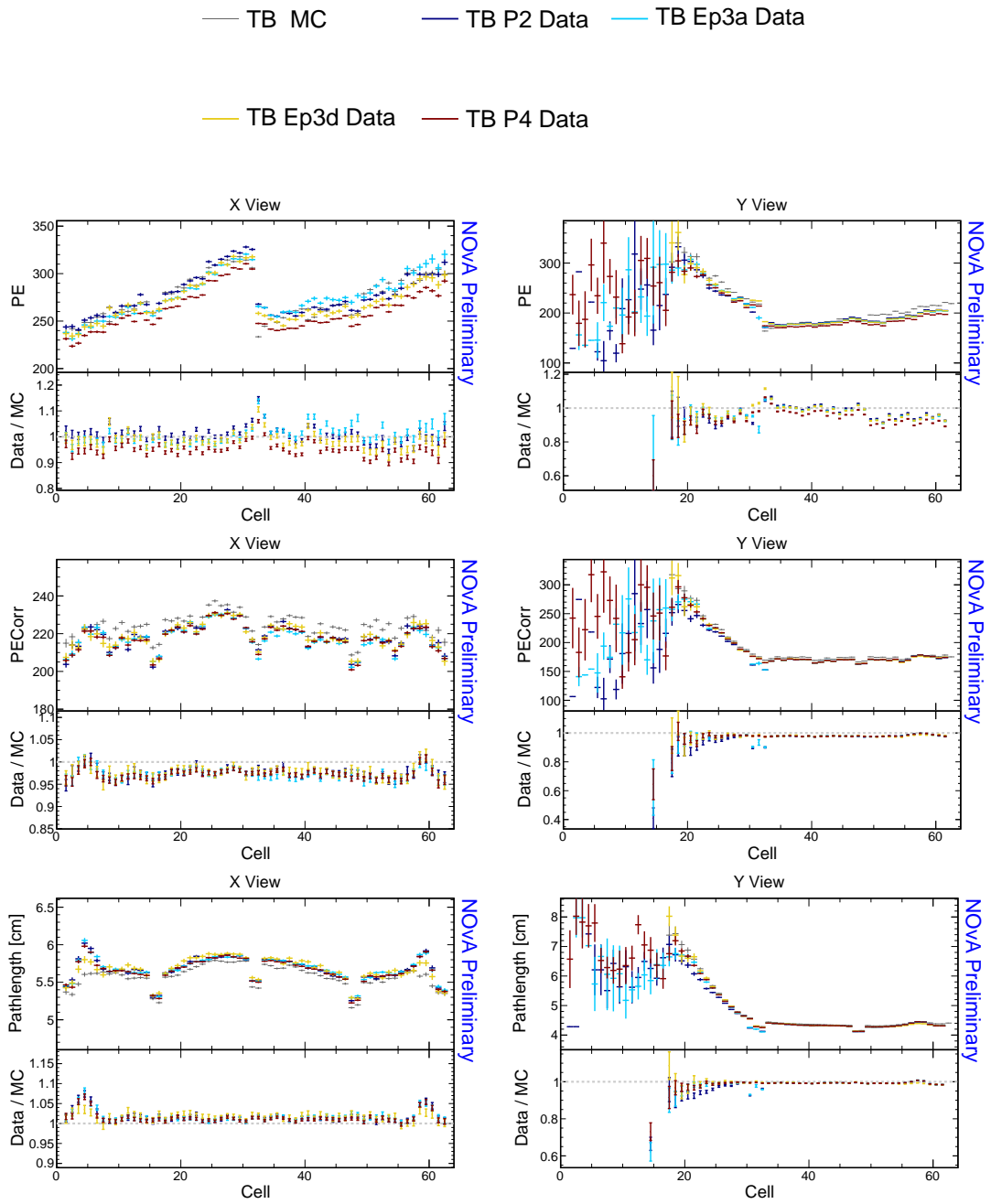


Figure 2.57: Distributions of stopping muons within a 1-2 m track window from the end of their tracks across the cells of the detector.

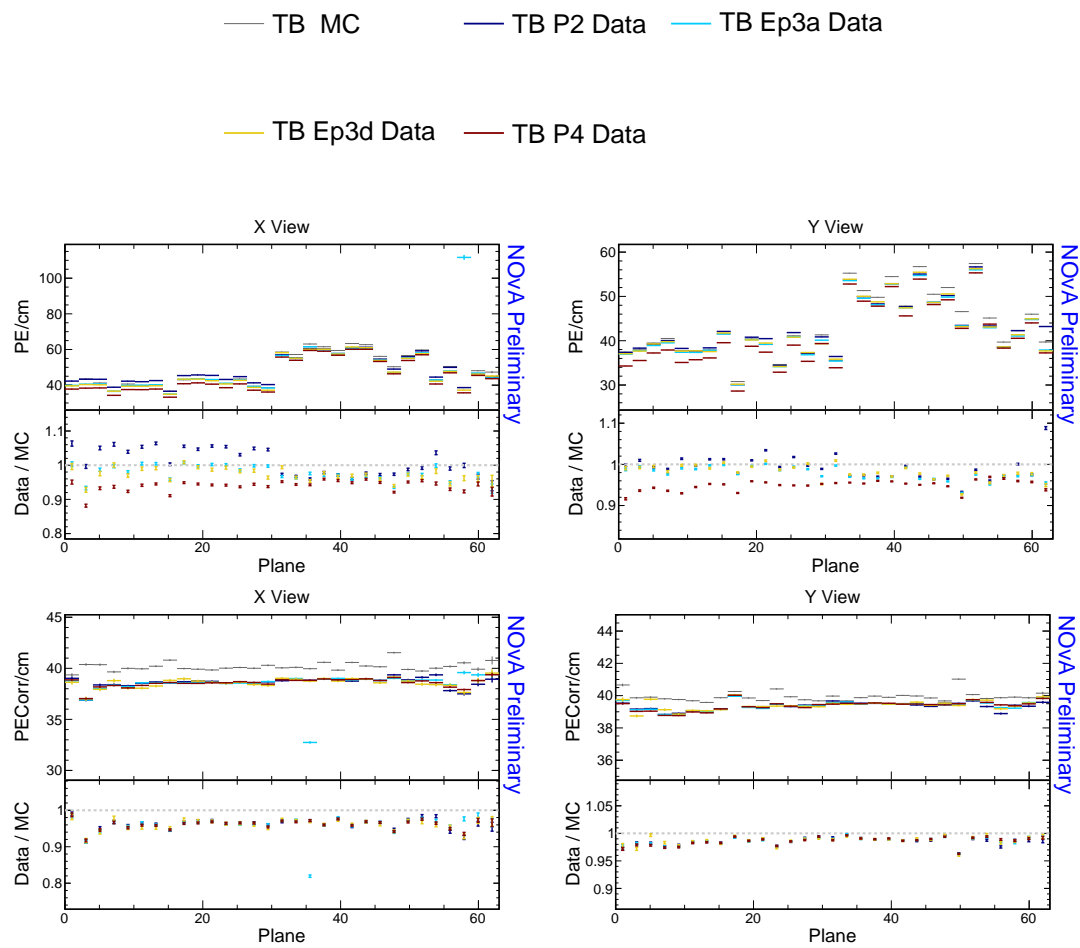


Figure 2.58: Distributions of stopping muons within a 1-2 m track window from the end of their tracks across the planes of the detector.

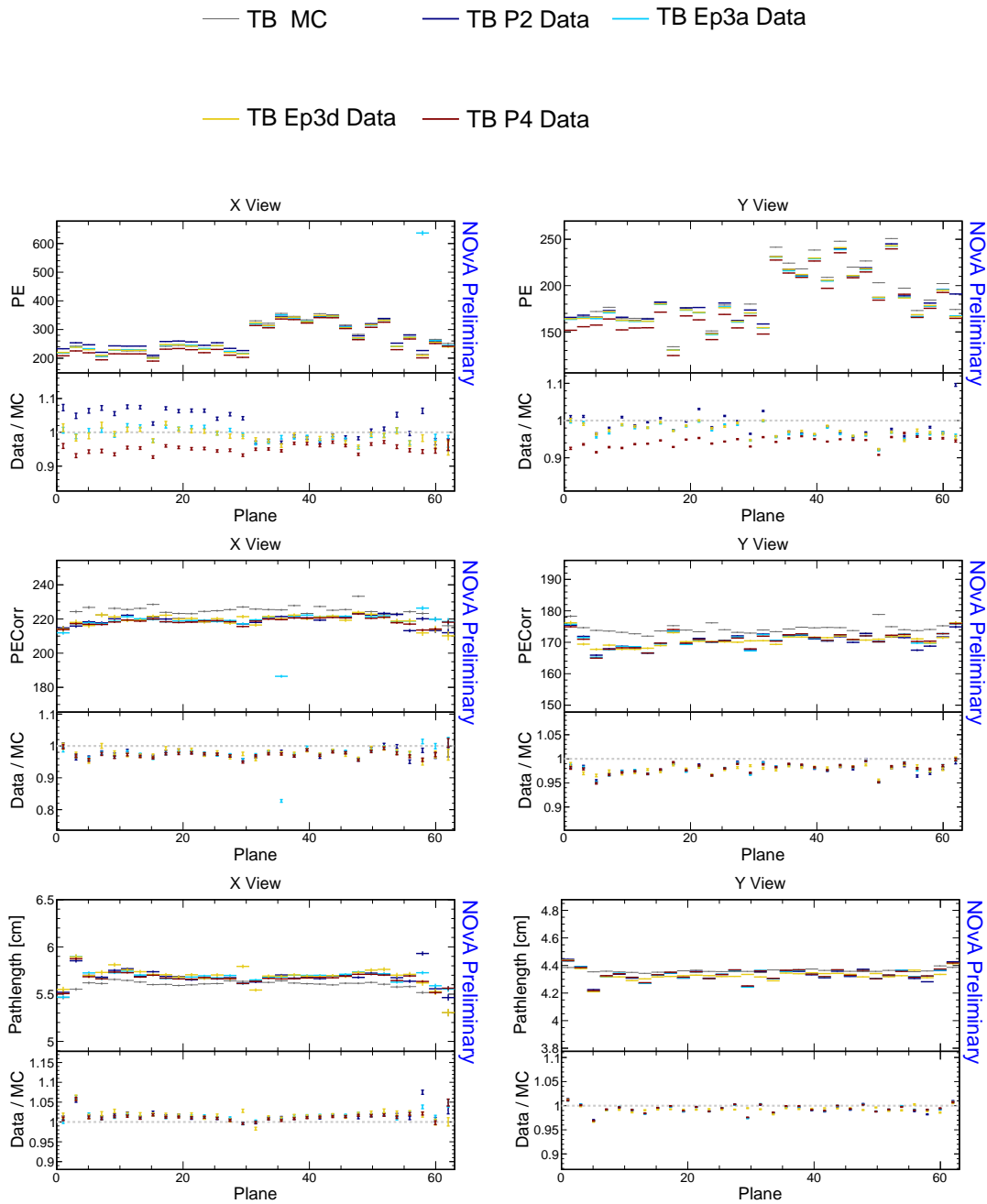


Figure 2.59: Distributions of stopping muons within a 1-2 m track window from the end of their tracks across the planes of the detector.

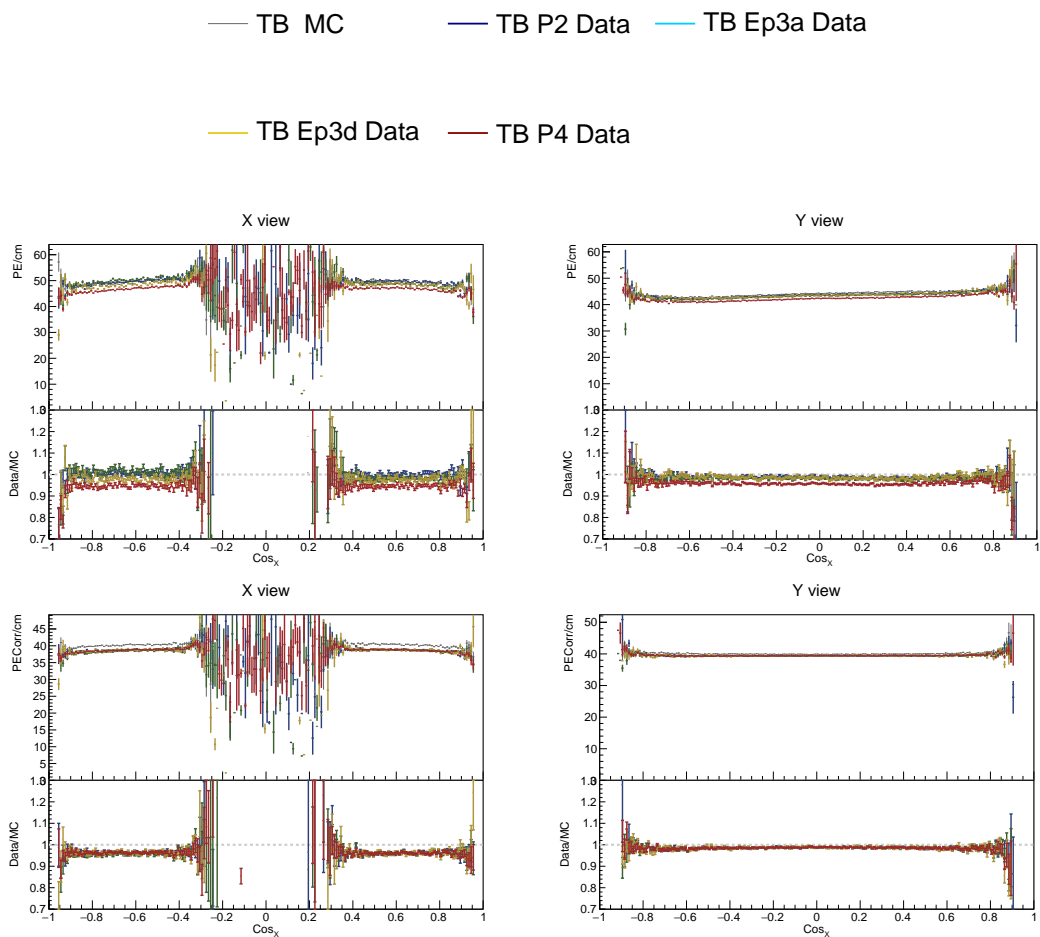


Figure 2.60: Distributions of stopping muons within a 1-2 m track window from the end of their tracks across the cosine of the track angle from the X (horizontal) axis.

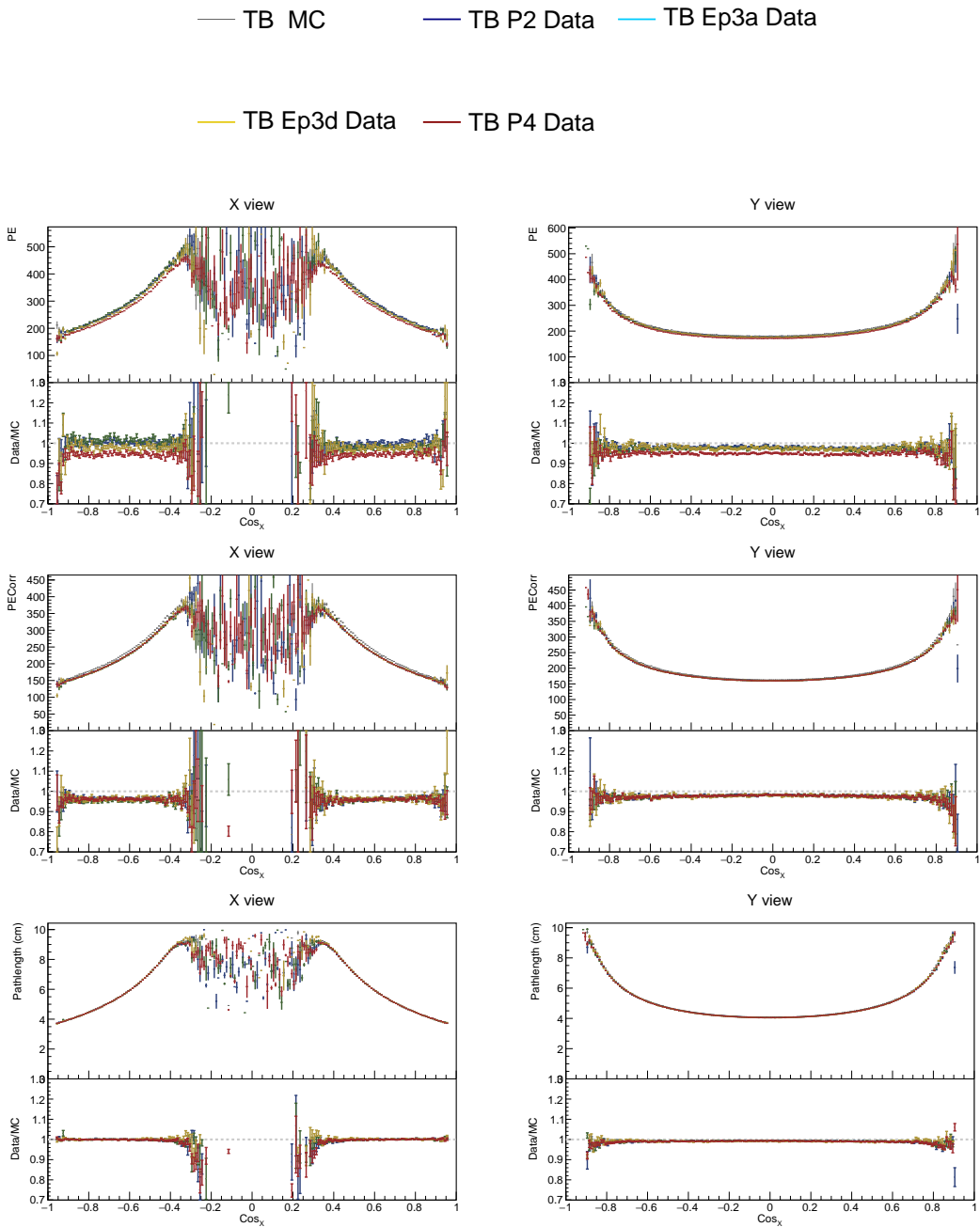


Figure 2.61: Distributions of stopping muons within a 1-2 m track window from the end of their tracks across the cosine of the track angle from the X (horizontal) axis.

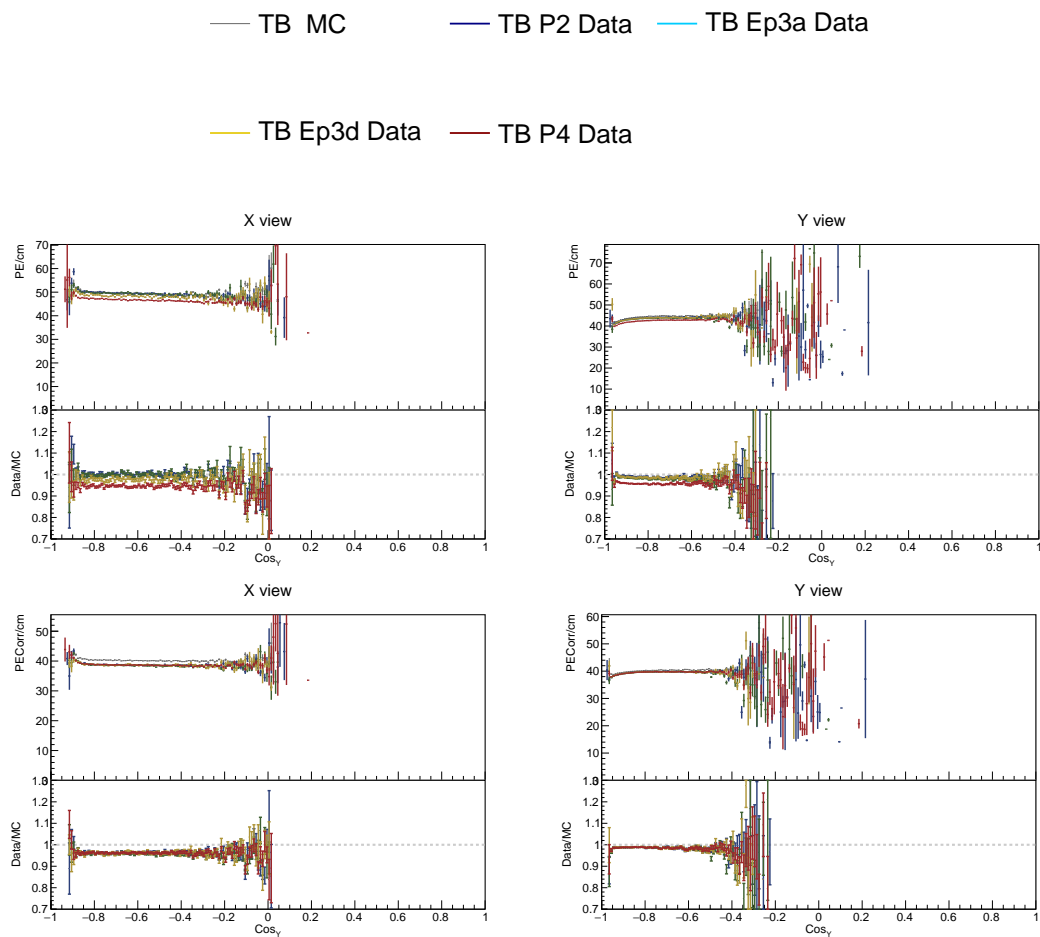


Figure 2.62: Distributions of stopping muons within a 1-2 m track window from the end of their tracks across the cosine of the track angle from the Y (vertical) axis.

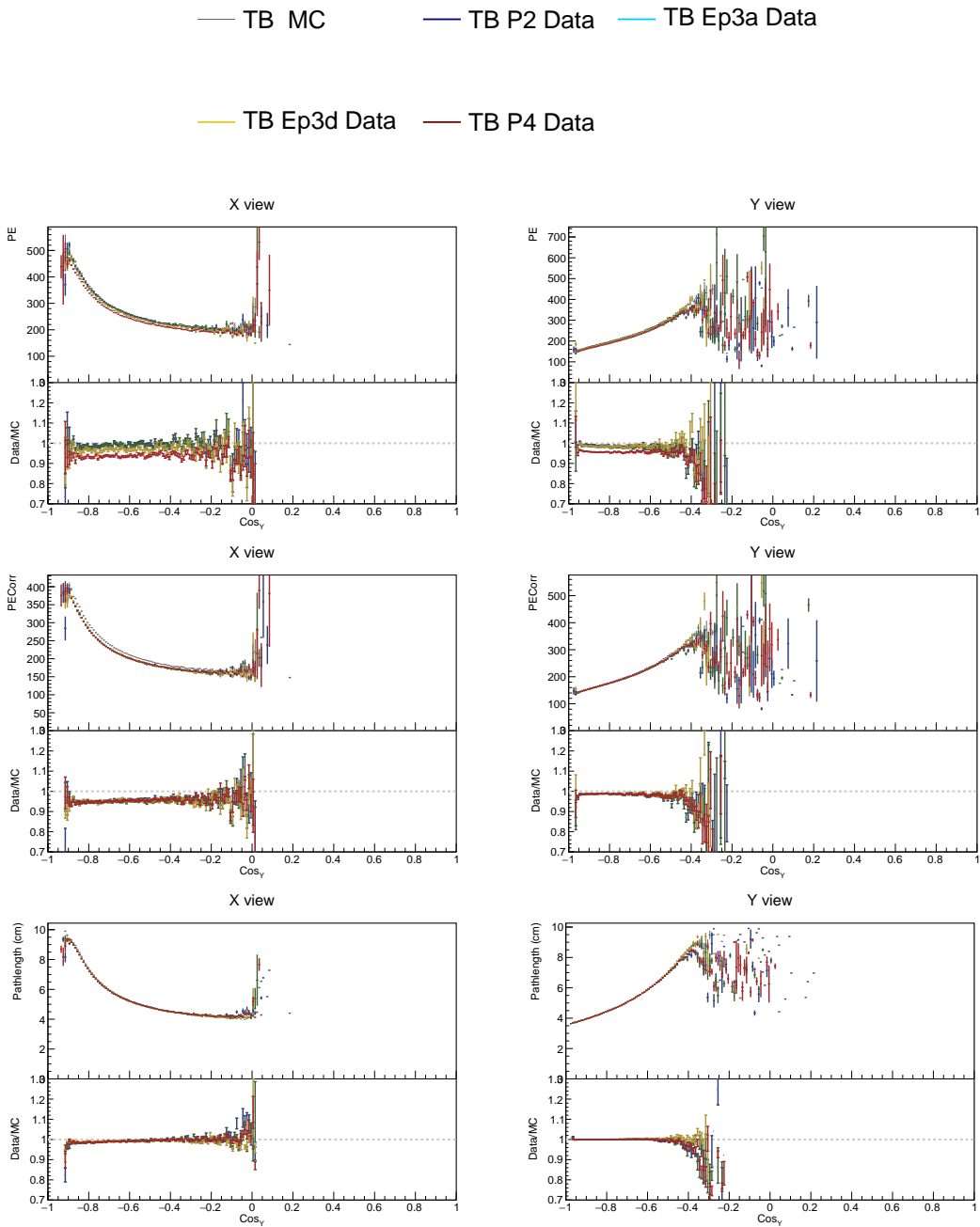


Figure 2.63: Distributions of stopping muons within a 1-2 m track window from the end of their tracks across the cosine of the track angle from the Y (vertical) axis.

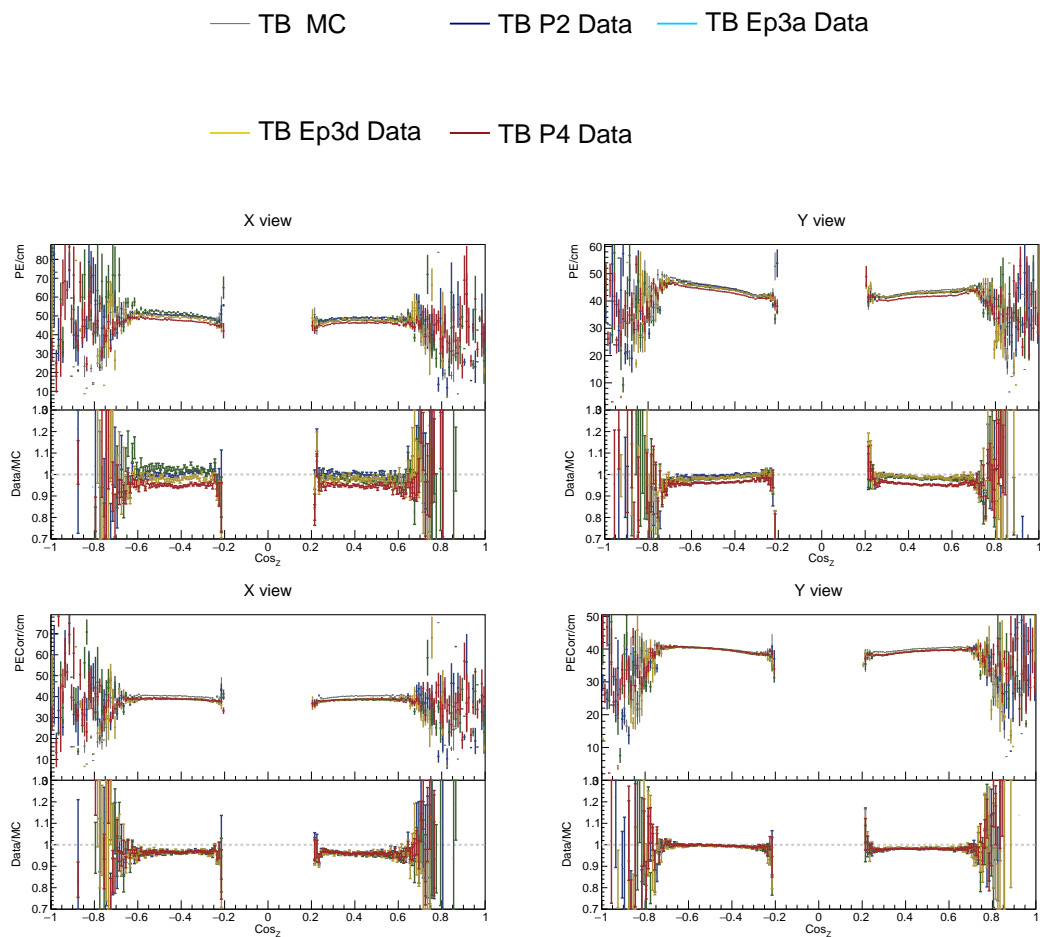


Figure 2.64: Distributions of stopping muons within a 1-2 m track window from the end of their tracks across the cosine of the track angle from the Z (beam) axis.

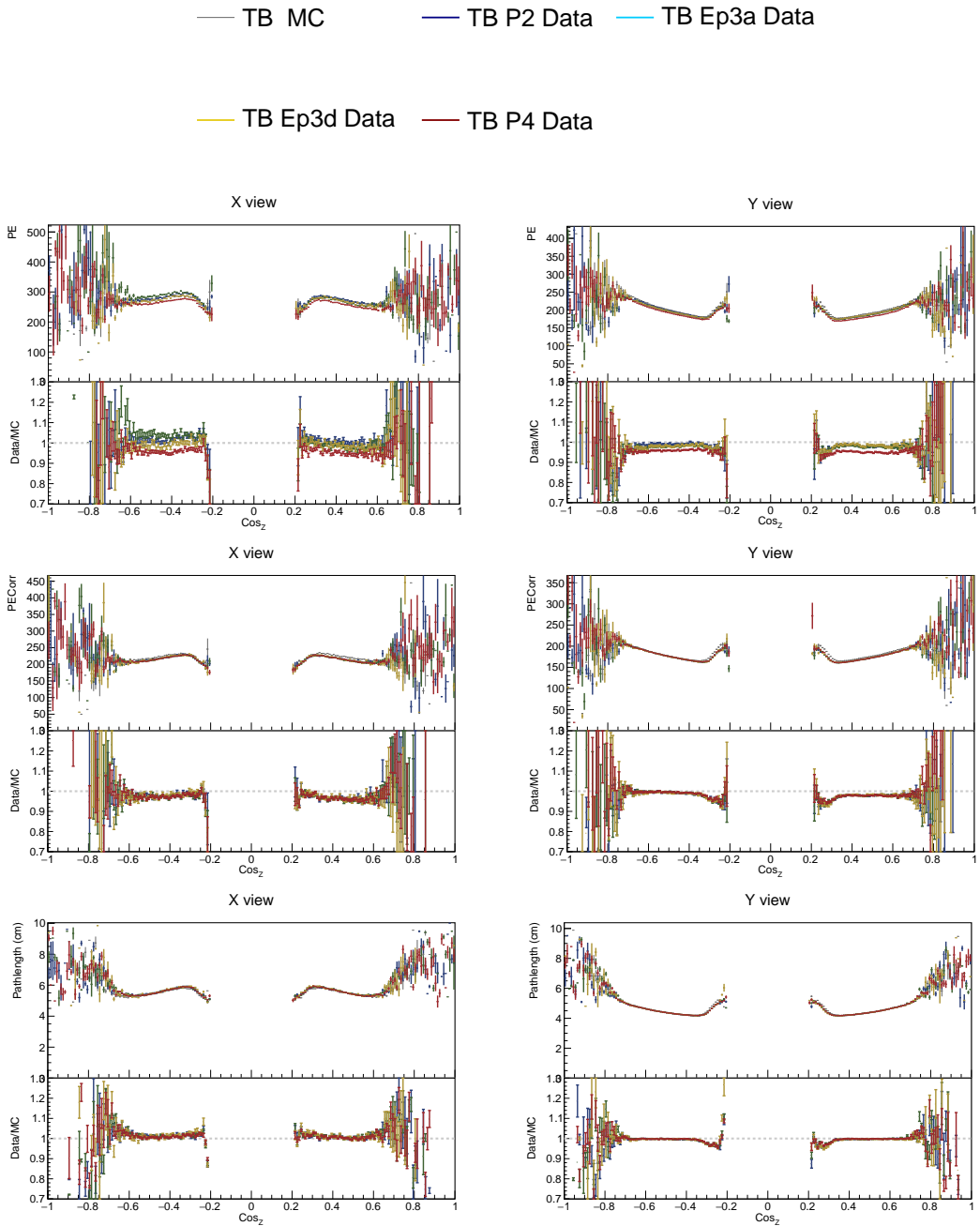


Figure 2.65: Distributions of stopping muons within a 1-2 m track window from the end of their tracks across the cosine of the track angle from the Z (beam) axis.

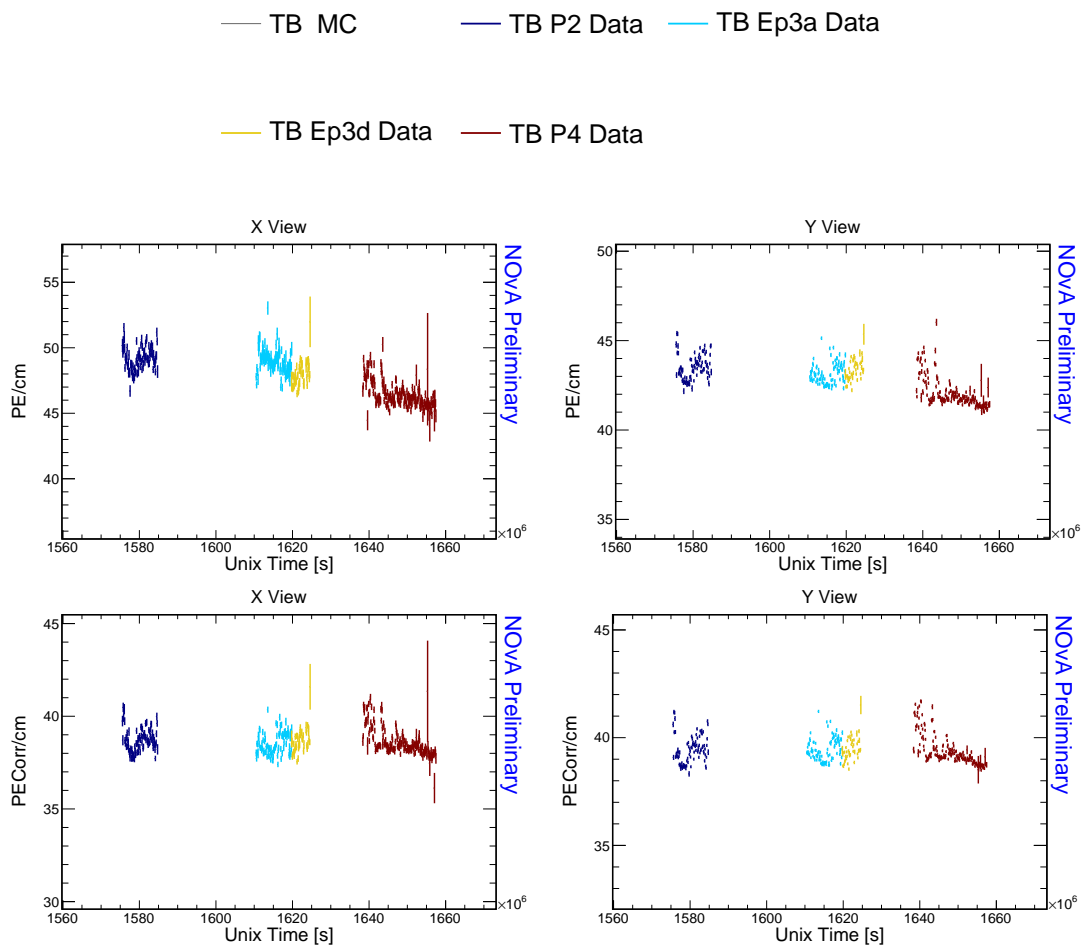


Figure 2.66: Distributions of stopping muons within a 1-2 m track window from the end of their tracks across the event UNIX time.

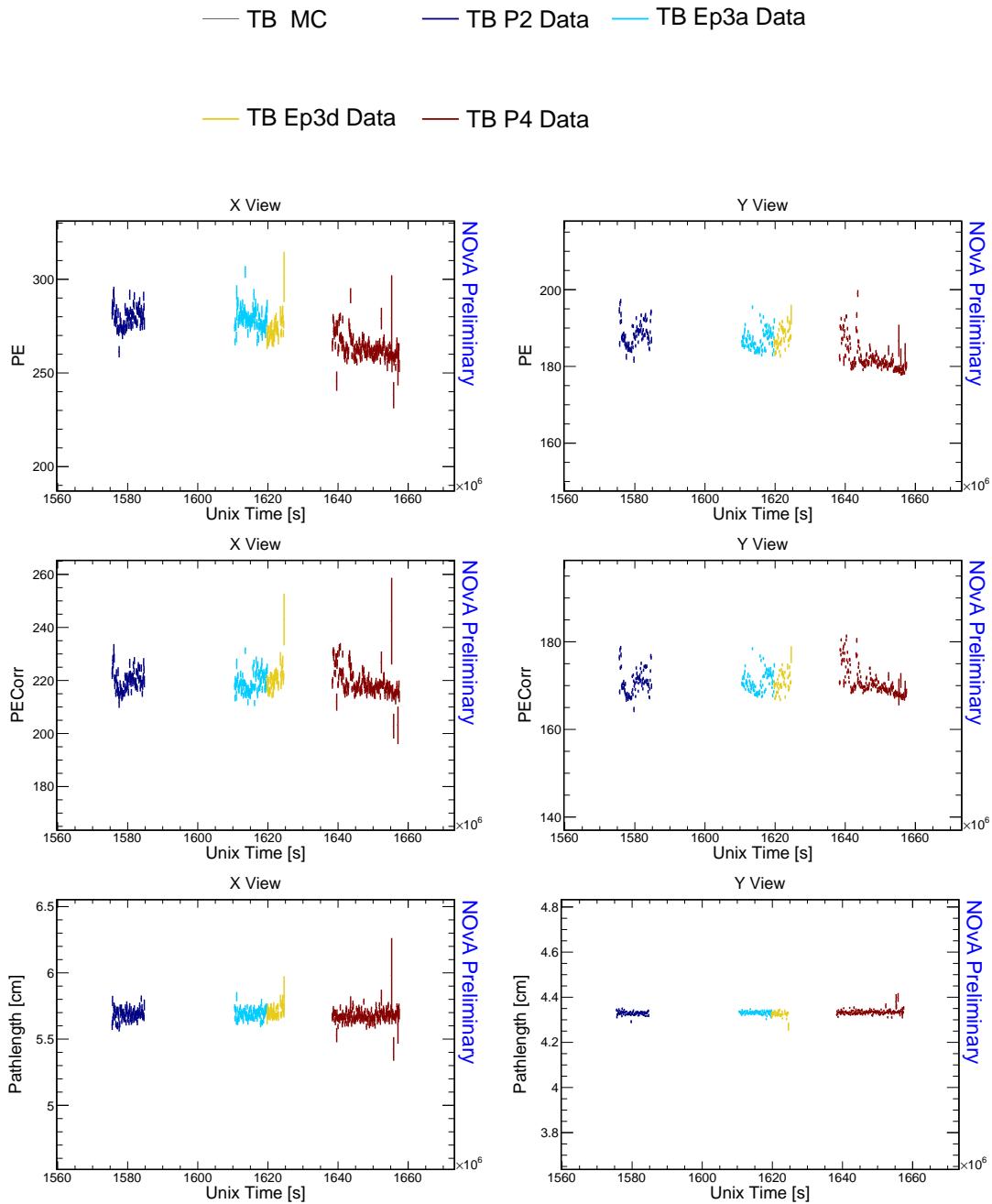


Figure 2.67: Distributions of stopping muons within a 1-2 m track window from the end of their tracks across the event UNIX time.

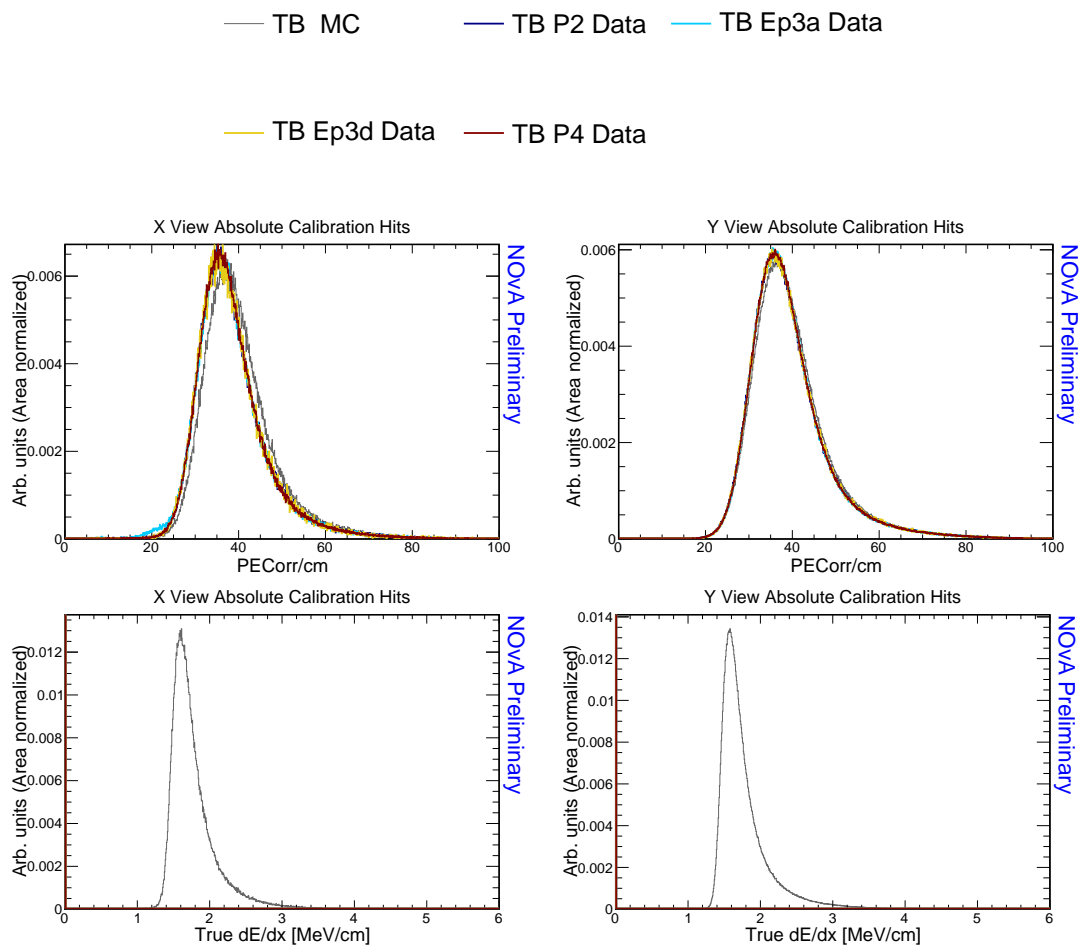


Figure 2.68: Distributions of stopping muons within a 1-2 m track window from the end of their tracks.

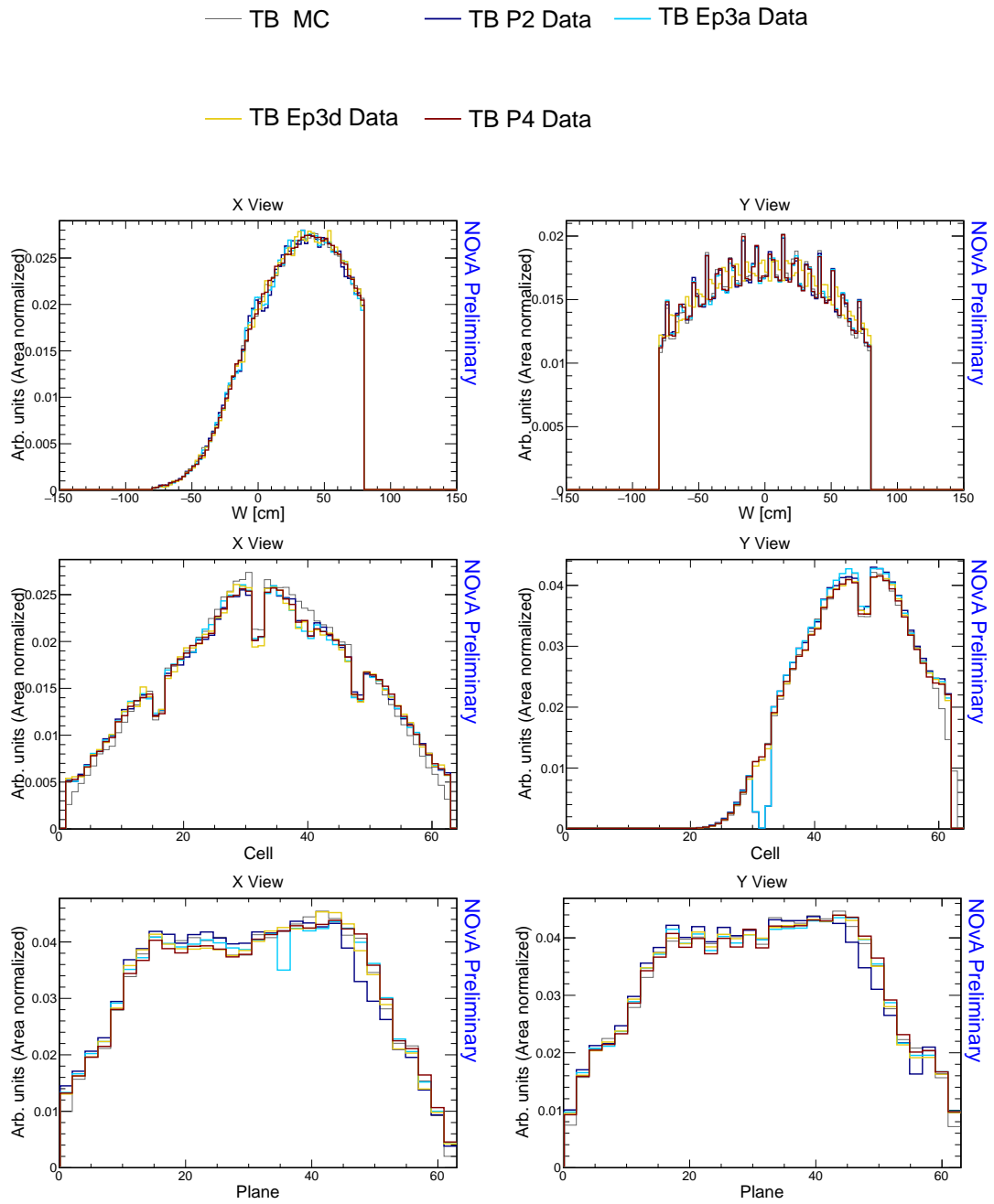


Figure 2.69: Distributions of stopping muons within a 1-2 m track window from the end of their tracks.



# Acronyms

**ADC** Analog-to-Digital Converter. 7, 14, 17, 18, 56

**APD** Avalanche Photodiode. 4, 6, 7, 11, 17, 18, 50, 51, 57

**ASIC** Application-Specific Integrated Circuit. 6, 7

**BDT** Boosted Decision Tree. 13

**BPF** Break Point Fitter. 13, 31, 32, 34–39, 41–46

**CC** Charged current. 2, 3, 10, 11

**CMC** Comprehensive Model Configuration. 10

**CNN** Convolutional Neural Network. 13

**COH $\pi$**  Coherent pion production. 10

**CP** Charge conjugation - Parity (symmetry). 1

**CRY** Cosmic-Ray Shower Generator. 10, 15, 30

**CVN** Convolutional Visual Network. 13

**DAQ** Data Acquisition. 6, 11, 16, 54

**DCM** Data Concentration Module. 7

**DIS** Deep Inelastic Scattering. 10

**FB** Fibre Brightness. 17, 18

**FD** Far Detector. 4–7, 10, 11, 17–19, 22, 24–29, 40, 44, 48

**FEB** Front End Board. 6, 7, 29, 31, 54, 57, 58, 60, 63, 64, 68

**FERMILAB** Fermi National Accelerator Laboratory. 1, 4, 28, 29

**FHC** Forward Horn Current (neutrino mode). 2, 3

**FPGA** Field Programmable Gate Array. 7

- FSI** Final State Interaction. 10
- FTBF** Fermilab Test Beam Facility. 25
- LOWESS** Locally Weighted Scatter plot Smoothing. 19, 20, 52
- MC** Monte Carlo. 8–10, 15, 30
- MEC** Meson Exchange Current. 10
- MEU** Muon Energy Unit. 21
- MI** Main Injector. 1, 2, 8
- MIP** minimum ionising particles. 14, 18
- ML** Machine Learning. 13
- MWPC** Multiwire Proportional Chamber. 26
- NC** Neutral Current. 11, 13
- ND** Near Detector. 2–5, 7, 11, 12, 22, 24–30, 39, 40, 44
- NDOS** Near Detector on the Surface. 4, 27–30, 66
- NOvA** NuMI Off-axis  $\nu_e$  Appearance (experiment). 1–14, 16, 17, 19–22, 24–28, 30, 31, 39, 55
- NuMI** Neutrinos from the Main Injector. 1–4, 8, 9, 11, 25
- PE** Photo Electron. 7, 17, 18
- PECorr** Corrected Photo Electrons. 18–20
- PID** Particle Identification. 13
- POT** Protons On Target. 1
- PPFX** Package to Predict the Flux. 8, 9, 23
- PVC** Polyvinyl chloride. 4–6, 22
- QE** Quasi Elastic (interaction). 10

**REMIN** Reconstructed Muon Identifier. [13](#)

**RES** Resonant baryon production. [10](#)

**RHC** Reverse Horn Current (antineutrino mode). [2](#), [3](#)

**T2K** Tokai to Kamioka (experiment). [9](#)

**TB** Test Beam. [4](#), [20](#)

**ToF** Time of Flight. [26](#)

**WLS** Wavelength Shifting (fibre). [4](#), [6](#), [11](#), [14](#), [16](#), [18](#), [20](#), [50](#), [51](#), [55](#)

# Bibliography

- [1] Nova experiments official website. URL <https://novaexperiment.fnal.gov>. Cited February 2024.
- [2] Fermi national accelerator laboratory official website. URL <https://fnal.gov>. Cited February 2024.
- [3] Gary Feldman for the NOvA Collaboration. Physics of the nova experiment. White paper, 2012. URL <https://nova-docdb.fnal.gov/cgi-bin>ShowDocument?docid=7733>. Public NOvA document: NOVA-doc-7733-v1, cited on 05.2020.
- [4] R.B. Patterson. The NOvA Experiment: Status and Outlook. *Nucl. Phys. B Proc. Suppl.*, 235-236:151–157, 2013. doi:[10.1016/j.nuclphysbps.2013.04.005](https://doi.org/10.1016/j.nuclphysbps.2013.04.005).
- [5] P. Adamson et al. First measurement of muon-neutrino disappearance in NOvA. *Phys. Rev. D*, 93(5):051104, 2016. doi:[10.1103/PhysRevD.93.051104](https://doi.org/10.1103/PhysRevD.93.051104).
- [6] M.A. Acero et al. First Measurement of Neutrino Oscillation Parameters using Neutrinos and Antineutrinos by NOvA. *Phys. Rev. Lett.*, 123(15):151803, 2019. doi:[10.1103/PhysRevLett.123.151803](https://doi.org/10.1103/PhysRevLett.123.151803).
- [7] M. A. Acero et al. Improved measurement of neutrino oscillation parameters by the NOvA experiment. *Phys. Rev. D*, 106(3):032004, 2022. doi:[10.1103/PhysRevD.106.032004](https://doi.org/10.1103/PhysRevD.106.032004).
- [8] M. A. Acero et al. Measurement of neutrino-induced neutral-current coherent  $\pi^0$  production in the NOvA near detector. *Phys. Rev. D*, 102(1):012004, 2020. doi:[10.1103/PhysRevD.102.012004](https://doi.org/10.1103/PhysRevD.102.012004).
- [9] M. A. Acero et al. Measurement of the double-differential muon-neutrino charged-current inclusive cross section in the NOvA near detector. *Phys. Rev. D*, 107(5):052011, 2023. doi:[10.1103/PhysRevD.107.052011](https://doi.org/10.1103/PhysRevD.107.052011).
- [10] M. A. Acero et al. Measurement of the  $\nu_e$ –Nucleus Charged-Current Double-Differential Cross Section at  $\langle E_\nu \rangle = 2.4$  GeV using NOvA. *Phys. Rev. Lett.*, 130(5):051802, 2023. doi:[10.1103/PhysRevLett.130.051802](https://doi.org/10.1103/PhysRevLett.130.051802).

- [11] M. A. Acero et al. Measurement of  $\nu_\mu$  charged-current inclusive  $\pi^0$  production in the NOvA near detector. *Phys. Rev. D*, 107(11):112008, 2023. doi:[10.1103/PhysRevD.107.112008](https://doi.org/10.1103/PhysRevD.107.112008).
- [12] P. Adamson et al. Search for active-sterile neutrino mixing using neutral-current interactions in NOvA. *Phys. Rev. D*, 96(7):072006, 2017. doi:[10.1103/PhysRevD.96.072006](https://doi.org/10.1103/PhysRevD.96.072006).
- [13] M. A. Acero et al. Search for Active-Sterile Antineutrino Mixing Using Neutral-Current Interactions with the NOvA Experiment. *Phys. Rev. Lett.*, 127(20):201801, 2021. doi:[10.1103/PhysRevLett.127.201801](https://doi.org/10.1103/PhysRevLett.127.201801).
- [14] M. A. Acero et al. Supernova neutrino detection in NOvA. *JCAP*, 10:014, 2020. doi:[10.1088/1475-7516/2020/10/014](https://doi.org/10.1088/1475-7516/2020/10/014).
- [15] M. A. Acero et al. Extended search for supernovalike neutrinos in NOvA coincident with LIGO/Virgo detections. *Phys. Rev. D*, 104(6):063024, 2021. doi:[10.1103/PhysRevD.104.063024](https://doi.org/10.1103/PhysRevD.104.063024).
- [16] M. A. Acero et al. Search for slow magnetic monopoles with the NOvA detector on the surface. *Phys. Rev. D*, 103(1):012007, 2021. doi:[10.1103/PhysRevD.103.012007](https://doi.org/10.1103/PhysRevD.103.012007).
- [17] Peter N. Shanahan and Patricia LaVern Vahle. Physics with NOvA: a half-time review. *Eur. Phys. J. ST*, 230(24):4259–4273, 2021. doi:[10.1140/epjs/s11734-021-00285-9](https://doi.org/10.1140/epjs/s11734-021-00285-9).
- [18] P. Adamson et al. The NuMI Neutrino Beam. *Nucl. Instrum. Meth. A*, 806:279–306, 2016. doi:[10.1016/j.nima.2015.08.063](https://doi.org/10.1016/j.nima.2015.08.063).
- [19] Katsuya Yonehara. Megawatt upgrade of numi target system. 1 2022. URL <https://www.osti.gov/biblio/1844332>.
- [20] Leonidas Aliaga Soplin. *Neutrino Flux Prediction for the NuMI Beamline*. PhD thesis, William-Mary Coll., 2016.
- [21] D. S. Ayres et al. The nova technical design report. *NOvA Collaboration*, 2007. doi:[10.2172/935497](https://doi.org/10.2172/935497).

- [22] Yury Kudenko. Neutrino detectors for oscillation experiments. *JINST*, 12(06):C06003, 2017. doi:[10.1088/1748-0221/12/06/C06003](https://doi.org/10.1088/1748-0221/12/06/C06003).
- [23] S. Mufson et al. Liquid scintillator production for the NOvA experiment. *Nucl. Instrum. Meth. A*, 799:1–9, 2015. doi:[10.1016/j.nima.2015.07.026](https://doi.org/10.1016/j.nima.2015.07.026).
- [24] Xinchun Tian. NOvA Data Acquisition Software System. In *Meeting of the APS Division of Particles and Fields*, 9 2011.
- [25] A. Aurisano, C. Backhouse, R. Hatcher, N. Mayer, J. Musser, R. Patterson, R. Schroeter, and A. Sousa. The NOvA simulation chain. *J. Phys. Conf. Ser.*, 664(7):072002, 2015. doi:[10.1088/1742-6596/664/7/072002](https://doi.org/10.1088/1742-6596/664/7/072002).
- [26] S. Agostinelli et al. GEANT4—a simulation toolkit. *Nucl. Instrum. Meth. A*, 506:250–303, 2003. doi:[10.1016/S0168-9002\(03\)01368-8](https://doi.org/10.1016/S0168-9002(03)01368-8).
- [27] Zarko Pavlovic. *Observation of Disappearance of Muon Neutrinos in the NuMI Beam*. PhD thesis, Texas U., 2008.
- [28] L. Aliaga et al. Neutrino Flux Predictions for the NuMI Beam. *Phys. Rev. D*, 94(9):092005, 2016. doi:[10.1103/PhysRevD.94.092005](https://doi.org/10.1103/PhysRevD.94.092005). [Addendum: *Phys. Rev. D* 95, 039903 (2017)].
- [29] C. Alt et al. Inclusive production of charged pions in p+C collisions at 158-GeV/c beam momentum. *Eur. Phys. J. C*, 49:897–917, 2007. doi:[10.1140/epjc/s10052-006-0165-7](https://doi.org/10.1140/epjc/s10052-006-0165-7).
- [30] D. S. Barton et al. Experimental study of the  $a$  dependence of inclusive hadron fragmentation. *Phys. Rev. D*, 27:2580–2599, Jun 1983. doi:[10.1103/PhysRevD.27.2580](https://doi.org/10.1103/PhysRevD.27.2580).
- [31] T.T. Böhlen, F. Cerutti, M.P.W. Chin, A. Fassò, A. Ferrari, P.G. Ortega, A. Mairani, P.R. Sala, G. Smirnov, and V. Vlachoudis. The fluka code: Developments and challenges for high energy and medical applications. 120:211–214. ISSN 0090-3752. doi:[10.1016/j.nds.2014.07.049](https://doi.org/10.1016/j.nds.2014.07.049).
- [32] Alfredo Ferrari, Paola R. Sala, Alberto Fasso, and Johannes Ranft. FLUKA: A multi-particle transport code (Program version 2005). 10 2005. doi:[10.2172/877507](https://doi.org/10.2172/877507).

- [33] Gemma Maria Tinti. *Sterile neutrino oscillations in MINOS and hadron production in pC collisions*. PhD thesis, 2010.
- [34] Andrey V. Lebedev. *Ratio of Pion Kaon Production in Proton Carbon Interactions*. PhD thesis, 2007.
- [35] B Baatar, G Barr, J Bartke, L Betev, O Chvala, J Dolejsi, V Eckardt, HG Fischer, Z Fodor, A Karev, et al. Inclusive production of protons, anti-protons, neutrons, deuterons and tritons in p+ c collisions at 158 gev/c beam momentum. *The European Physical Journal C*, 73:1–66, 2013. doi:[10.1140/epjc/s10052-013-2364-3](https://doi.org/10.1140/epjc/s10052-013-2364-3).
- [36] N. Abgrall et al. Measurements of  $\pi^\pm$ ,  $K^\pm$ ,  $K_S^0$ ,  $\Lambda$  and proton production in proton–carbon interactions at 31 GeV/c with the NA61/SHINE spectrometer at the CERN SPS. *Eur. Phys. J. C*, 76(2):84, 2016. doi:[10.1140/epjc/s10052-016-3898-y](https://doi.org/10.1140/epjc/s10052-016-3898-y).
- [37] H. Adhikary et al. Measurements of  $\pi^+$ ,  $\pi^-$ ,  $p$ ,  $\bar{p}$ ,  $K^+$  and  $K^-$  production in 120 GeV/c p + C interactions. *Phys. Rev. D*, 108:072013, 2023. doi:[10.1103/PhysRevD.108.072013](https://doi.org/10.1103/PhysRevD.108.072013).
- [38] A. Aduszkiewicz et al. Measurements of production and inelastic cross sections for p+C , p+Be , and p+Al at 60 GeV/c and p+C and p+Be at 120 GeV/c. *Phys. Rev. D*, 100(11):112001, 2019. doi:[10.1103/PhysRevD.100.112001](https://doi.org/10.1103/PhysRevD.100.112001).
- [39] A. Aduszkiewicz et al. Measurements of hadron production in  $\pi^+ + C$  and  $\pi^+ + Be$  interactions at 60 GeV/c. *Phys. Rev. D*, 100(11):112004, 2019. doi:[10.1103/PhysRevD.100.112004](https://doi.org/10.1103/PhysRevD.100.112004).
- [40] H. Adhikary et al. Measurements of KS0,  $\Lambda$ , and  $\Lambda^-$  production in 120 GeV/c p+C interactions. *Phys. Rev. D*, 107(7):072004, 2023. doi:[10.1103/PhysRevD.107.072004](https://doi.org/10.1103/PhysRevD.107.072004).
- [41] Matej Pavlin. Hadron production measurements for neutrino experiments, 2020. URL [https://indico.fnal.gov/event/43209/contributions/187869/attachments/130502/159028/HadronProduction\\_neutrino2020.pdf](https://indico.fnal.gov/event/43209/contributions/187869/attachments/130502/159028/HadronProduction_neutrino2020.pdf). Presented on Neutrino 2020 conference.

- [42] N. Abgrall et al. Measurements of  $\pi^\pm$ ,  $K^\pm$  and proton double differential yields from the surface of the T2K replica target for incoming 31 GeV/c protons with the NA61/SHINE spectrometer at the CERN SPS. *Eur. Phys. J. C*, 79(2):100, 2019. doi:[10.1140/epjc/s10052-019-6583-0](https://doi.org/10.1140/epjc/s10052-019-6583-0).
- [43] T. Akaishi et al. EMPHATIC: A Proposed Experiment to Measure Hadron Scattering and Production Cross Sections for Improved Neutrino Flux Predictions. 12 2019.
- [44] C. Andreopoulos et al. The GENIE Neutrino Monte Carlo Generator. *Nucl. Instrum. Meth. A*, 614:87–104, 2010. doi:[10.1016/j.nima.2009.12.009](https://doi.org/10.1016/j.nima.2009.12.009).
- [45] J. Nieves, J. E. Amaro, and M. Valverde. Inclusive quasielastic charged-current neutrino-nucleus reactions. *Phys. Rev. C*, 70:055503, Nov 2004. doi:[10.1103/PhysRevC.70.055503](https://doi.org/10.1103/PhysRevC.70.055503).
- [46] Aaron S. Meyer, Minerba Betancourt, Richard Gran, and Richard J. Hill. Deuterium target data for precision neutrino-nucleus cross sections. *Phys. Rev. D*, 93:113015, Jun 2016. doi:[10.1103/PhysRevD.93.113015](https://doi.org/10.1103/PhysRevD.93.113015).
- [47] J. Nieves, I. Ruiz Simo, and M. J. Vicente Vacas. Inclusive charged-current neutrino-nucleus reactions. *Phys. Rev. C*, 83:045501, Apr 2011. doi:[10.1103/PhysRevC.83.045501](https://doi.org/10.1103/PhysRevC.83.045501).
- [48] R. Gran, J. Nieves, F. Sanchez, and M. J. Vicente Vacas. Neutrino-nucleus quasi-elastic and 2p2h interactions up to 10 gev. *Phys. Rev. D*, 88:113007, Dec 2013. doi:[10.1103/PhysRevD.88.113007](https://doi.org/10.1103/PhysRevD.88.113007).
- [49] Ch. Berger and L. M. Sehgal. Lepton mass effects in single pion production by neutrinos. *Phys. Rev. D*, 76:113004, Dec 2007. doi:[10.1103/PhysRevD.76.113004](https://doi.org/10.1103/PhysRevD.76.113004).
- [50] Ch. Berger and L. M. Sehgal. Partially conserved axial vector current and coherent pion production by low energy neutrinos. *Phys. Rev. D*, 79:053003, Mar 2009. doi:[10.1103/PhysRevD.79.053003](https://doi.org/10.1103/PhysRevD.79.053003).
- [51] A Bodek and U. K. Yang. Higher twist, xi(omega) scaling, and effective LO PDFs for lepton scattering in the few GeV region. *J. Phys. G*, 29:1899–1906, 2003. doi:[10.1088/0954-3899/29/8/369](https://doi.org/10.1088/0954-3899/29/8/369).

- [52] T. Yang, C. Andreopoulos, H. Gallagher, K. Hoffmann, and P. Kehayias. A Hadronization Model for Few-GeV Neutrino Interactions. *Eur. Phys. J. C*, 63: 1–10, 2009. doi:[10.1140/epjc/s10052-009-1094-z](https://doi.org/10.1140/epjc/s10052-009-1094-z).
- [53] L.L. Salcedo, E. Oset, M.J. Vicente-Vacas, and C. Garcia-Recio. Computer simulation of inclusive pion nuclear reactions. 484(3):557–592. ISSN 0375-9474. doi:[10.1016/0375-9474\(88\)90310-7](https://doi.org/10.1016/0375-9474(88)90310-7).
- [54] Chris Hagmann, David Lange, and Douglas Wright. Cosmic-ray shower generator (cry) for monte carlo transport codes. volume 2, pages 1143 – 1146. ISBN 978-1-4244-0922-8. doi:[10.1109/NSSMIC.2007.4437209](https://doi.org/10.1109/NSSMIC.2007.4437209).
- [55] C. N. Chou. The nature of the saturation effect of fluorescent scintillators. *Phys. Rev.*, 87:904–905, Sep 1952. doi:[10.1103/PhysRev.87.904](https://doi.org/10.1103/PhysRev.87.904). URL <https://link.aps.org/doi/10.1103/PhysRev.87.904>.
- [56] M. Baird, J. Bian, M. Messier, E. Niner, D. Rocco, and K. Sachdev. Event Reconstruction Techniques in NOvA. *J. Phys. Conf. Ser.*, 664(7):072035, 2015. doi:[10.1088/1742-6596/664/7/072035](https://doi.org/10.1088/1742-6596/664/7/072035).
- [57] Martin Ester, Hans-Peter Kriegel, Jörg Sander, and Xiaowei Xu. A density-based algorithm for discovering clusters in large spatial databases with noise. In *Proceedings of the Second International Conference on Knowledge Discovery and Data Mining*, KDD’96, page 226–231. AAAI Press, 1996. doi:[10.5555/3001460.3001507](https://doi.org/10.5555/3001460.3001507).
- [58] Leandro A. F. Fernandes and Manuel Menezes de Oliveira Neto. Real-time line detection through an improved hough transform voting scheme. *Pattern Recognit.*, 41:299–314, 2008. doi:[10.1016/j.patcog.2007.04.003](https://doi.org/10.1016/j.patcog.2007.04.003). URL <https://api.semanticscholar.org/CorpusID:5996185>.
- [59] Mattias Ohlsson, Carsten Peterson, and Alan L. Yuille. Track finding with deformable templates — the elastic arms approach. 71(1):77–98. ISSN 0010-4655. doi:[10.1016/0010-4655\(92\)90074-9](https://doi.org/10.1016/0010-4655(92)90074-9). URL <https://www.sciencedirect.com/science/article/pii/0010465592900749>.
- [60] R. Krishnapuram and J.M. Keller. A possibilistic approach to clustering. *IEEE Transactions on Fuzzy Systems*, 1(2):98–110, 1993. doi:[10.1109/91.227387](https://doi.org/10.1109/91.227387).

- [61] Miin-Shen Yang and Kuo-Lung Wu. Unsupervised possibilistic clustering. 39(1):5–21. ISSN 0031-3203. doi:<https://doi.org/10.1016/j.patcog.2005.07.005>. URL <https://www.sciencedirect.com/science/article/pii/S0031320305002943>.
- [62] Nicholas Jacob Raddatz. *Measurement of Muon Neutrino Disappearance with Non-Fiducial Interactions in the NO $\nu$ A Experiment*. PhD thesis, Minnesota U., 2016.
- [63] Michael David Baird. *An Analysis of Muon Neutrino Disappearance from the NuMI Beam Using an Optimal Track Fitter*. PhD thesis, Indiana U., 2015.
- [64] G. Lutz. Optimum track fitting in the presence of multiple scattering. 273(1):349–361. ISSN 0168-9002. doi:[https://doi.org/10.1016/0168-9002\(88\)90836-4](https://doi.org/10.1016/0168-9002(88)90836-4). URL <https://www.sciencedirect.com/science/article/pii/0168900288908364>.
- [65] Brian Rebel. Window tracking algorithm for cosmic ray muons. NOVA Document 15977-v1. URL <https://nova-docdb.fnal.gov/cgi-bin/sso>ShowDocument?docid=15977>. NO $\nu$ A internal document.
- [66] Christian Szegedy, Wei Liu, Yangqing Jia, Pierre Sermanet, Scott Reed, Dragomir Anguelov, Dumitru Erhan, Vincent Vanhoucke, and Andrew Rabinovich. Going Deeper with Convolutions. art. arXiv:1409.4842. doi:[10.48550/arXiv.1409.4842](https://arxiv.org/abs/1409.4842).
- [67] A. Aurisano, A. Radovic, D. Rocco, A. Himmel, M.D. Messier, E. Niner, G. Pawloski, F. Psihas, A. Sousa, and P. Vahle. A Convolutional Neural Network Neutrino Event Classifier. *JINST*, 11(09):P09001, 2016. doi:[10.1088/1748-0221/11/09/P09001](https://doi.org/10.1088/1748-0221/11/09/P09001).
- [68] Fernanda Psihas. Measurement of long baseline neutrino oscillations and improvements from deep learning. 1 2018. doi:[10.2172/1437288](https://doi.org/10.2172/1437288). URL <https://www.osti.gov/biblio/1437288>.
- [69] Prabhjot Singh. *Extraction of Neutrino Oscillation Parameters using a Simultaneous Fit of  $\nu_\mu$  Disappearance and  $\nu_e$  Appearance data with the NO $\nu$ A Experiment*. PhD thesis, University of Delhi, Dept. of Physics and Astrophysics, India, Delhi U., 9 2019.
- [70] Luke Vinton. Calorimetric Energy Scale Calibration of the NO $\nu$ A Detectors. NOVA Document 13579, document FA\_Calorimetric\_energy\_scale.pdf. URL

<https://nova-docdb.fnal.gov/cgi-bin/sso>ShowDocument?docid=13579>. NOvA Technical Note.

- [71] Ryan J. Nichol. Fibre brightness from cosmic muon data. NOVA Document 34909. URL <https://nova-docdb.fnal.gov/cgi-bin/sso>ShowDocument?docid=34909>. NOvA technical note.
- [72] Prabhjot Singh. Attenuation Calibration of the NOvA Detectors. In *The 38th International Conference on High Energy Physics (ICHEP 2016)*, 2024. URL <https://nova-docdb.fnal.gov/cgi-bin/sso>ShowDocument?docid=15840>. (cited on 03.2024).
- [73] Michael Wallbank. The NOvA Test Beam Program. ICHEP2020:188, . doi:[10.22323/1.390.0188](https://doi.org/10.22323/1.390.0188).
- [74] Alex Sousa. Test Beam Plenary Update - FNAL September 2018. NOVA Document 33012, . URL <https://nova-docdb.fnal.gov/cgi-bin/sso>ShowDocument?docid=33012>. NOvA internal document.
- [75] Alex Sousa, Ryan Nichol, Karol Lang, and Jeff Nelson. NOvA Test Beam Task Force Report. NOVA Document 15750. URL <https://nova-docdb.fnal.gov/cgi-bin/sso>ShowDocument?docid=15750>. NOvA technical note.
- [76] Alex Sousa. NOvA Test Beam Status and Plans - Support Documentation. NOVA Document 22172-v2, . URL <https://nova-docdb.fnal.gov/cgi-bin/sso>ShowDocument?docid=22172>. NOvA technical note.
- [77] Fermilab test beam facility official website. URL <https://ftbf.fnal.gov/>. Cited March 2024.
- [78] Alex Sousa. NOvA Test Beam Plenary @ IU Collaboration Meeting. NOVA Document 29543, . URL <https://nova-docdb.fnal.gov/cgi-bin/sso>ShowDocument?docid=29543>. NOvA internal document.
- [79] Michael Wallbank. Final Test Beam Updates (Geometry and Other!). NOVA Document 58388, . URL <https://nova-docdb.fnal.gov/cgi-bin/sso>ShowDocument?docid=58388>. NOvA internal document.

- [80] Michael Wallbank. Understanding, Improving, Validating the Test Beam Geometry. NOVA Document 57955, February 2023. URL <https://nova-docdb.fnal.gov/cgi-bin/sso>ShowDocument?docid=57955>. NOvA internal document.
- [81] Robert Kralik. Test beam calibration update. NOVA Document 57516-v2. URL <https://nova-docdb.fnal.gov/cgi-bin/sso>ShowDocument?docid=57516>. NOvA internal document.
- [82] Alex Sousa. Test Beam Plenary Update - Jun. 6, 2019. NOVA Document 38349, . URL <https://nova-docdb.fnal.gov/cgi-bin/sso>ShowDocument?docid=38349>. NOvA internal document.
- [83] Miniboone experiments official website. URL <https://www-boone.fnal.gov/>. Cited March 2024.
- [84] Alex Sousa. Filling System and Scintillator Status. NOVA Document 34067, . URL <https://nova-docdb.fnal.gov/cgi-bin/sso>ShowDocument?docid=34067>. NOvA internal document.
- [85] Junting Huang, Will Flanagan, and Beatriz Tapia Oregui. Test Beam: Light Yield of the Liquid Scintillator Drained from the NDOS Detector. NOVA Document 38740. URL <https://nova-docdb.fnal.gov/cgi-bin/sso>ShowDocument?docid=38740>. NOvA internal document.
- [86] Dung Phan. Test Beam: Tintometer Measurement of Texas A&M oil. NOVA Document 39088. URL <https://nova-docdb.fnal.gov/cgi-bin/sso>ShowDocument?docid=39088>. NOvA internal document.
- [87] Alex Sousa. Test Beam Scintillator Fill Plan. NOVA Document 34196, . URL <https://nova-docdb.fnal.gov/cgi-bin/sso>ShowDocument?docid=34196>. NOvA internal document.
- [88] Alex Sousa. 2nd Block Filling Status - Nov. 18, 2019. NOVA Document 41961, . URL <https://nova-docdb.fnal.gov/cgi-bin/sso>ShowDocument?docid=41961>. NOvA internal document.
- [89] Teresa Megan Lackey. *Proton Scattering in NOvA Test Beam*. PhD thesis.

- [90] David Northacker, Alex Sousa, and Yagmur Torun. Test Beam - Overfilling Horizontal Planes. NOVA Document 49439. URL <https://nova-docdb.fnal.gov/cgi-bin/sso>ShowDocument?docid=49439>. NOvA internal document.
- [91] Mark Messier and Teresa Lackey. Data driven cosmic generation. NOVA Document 51327-v3. URL <https://nova-docdb.fnal.gov/cgi-bin/sso>ShowDocument?docid=51327&version=3>. NOvA internal document.
- [92] R. L. Workman and Others. Review of Particle Physics. 2022:083C01. doi:[10.1093/ptep/ptac097](https://doi.org/10.1093/ptep/ptac097).
- [93] Anna Maureen Hall. TB P2 Calib. Summary. NOVA Document 49674. URL <https://nova-docdb.fnal.gov/cgi-bin/sso>ShowDocument?docid=49674>. NOvA internal document.
- [94] Matthew Strait. Update on light level tuning. NOVA Document 43249. URL <https://nova-docdb.fnal.gov/cgi-bin/sso>ShowDocument?docid=43249>. NOvA internal document.
- [95] Artur Sztuc. DCM/FEB Shut-Off Studies. NOVA Document 53658. URL <https://nova-docdb.fnal.gov/cgi-bin/sso>ShowDocument?docid=53658>. NOvA internal document.